

10-
NASA Technical Memorandum 78631

Design of Microstrip Disk Antenna Arrays

M. C. Bailey and F. G. Parks

FEBRUARY 1978

U. S. AIR FORCE

HQ SAMTEC, AFL 2827
TECHNICAL LIBRARY (PMET)
VANDENBERG AFB, CA 93437.

NASA

Design of Microstrip Disk Antenna Arrays

M. C. Bailey

Langley Research Center
Hampton, Virginia

and

F. G. Parks

University of Kansas
Lawrence, Kansas



National Aeronautics
and Space Administration

**Scientific and Technical
Information Office**

1978

CONTENTS

SUMMARY	1
INTRODUCTION	1
SYMBOLS	1
THEORY AND DESIGN OF MICROSTRIP DISK ANTENNAS	4
Microstrip Element	4
Input impedance	4
Resonant frequency	4
Bandwidth	6
Radiation patterns	6
Array Considerations	7
Radiation pattern	7
Directivity	7
Gain and efficiency	7
Beamwidth	7
Element spacing	8
Element excitation	8
Mutual Coupling	9
Element patterns	10
Mutual coupling coefficients	10
Two-element coupling	11
Coupling coefficient calculation	12
Design Procedure	12
DEMONSTRATION ARRAYS	13
Array Description	13
Feed Network	14
Stripline network	14
Stripline packaging	15
Beam Scanning	15
Radio Frequency Performance Characteristics	16
Directivity	16
Volumetric patterns	16
Principal plane patterns	17
Sidelobes	17
Gain and efficiency	17
Impedance	17
Bandwidth	17
CONCLUDING REMARKS	17
REFERENCES	19
TABLE	21
FIGURES	22

SUMMARY

The radio frequency characteristics and design parameters for microstrip disk antenna elements and planar arrays are presented. Two C-band model arrays (an 8-element linear and an 8 by 8 planar) were designed, fabricated, and tested to demonstrate the technique of using microstrip elements for array applications. These arrays were designed with a cosine amplitude distribution. The effects of a thermal protective cover upon the electrical performance of microstrip antennas were not considered in this paper.

INTRODUCTION

Microstrip array design techniques are well suited for applications where a physically thin, conformal, rugged, and inexpensive antenna is required. (See refs. 1 to 6.) Although microstrip elements are relatively narrow band devices, these antennas will exhibit sufficient bandwidth characteristics for many aerospace applications.

The microstrip antenna is basically a printed circuit element which is supported parallel to a ground plane by a dielectric material, as shown in figure 1. The structure may be fabricated from standard printed circuit double-clad laminates. The metal on one side of the laminate is the ground plane, and the copper on the other side is etched away to leave the microstrip element. The size and shape (square, rectangular, circular, etc.) of the microstrip element will produce different electrical characteristics. The actual geometry of the microstrip element may, therefore, depend upon the specific application. The basic objective of this paper is to present detailed design information for the circular element.

SYMBOLS

a	radius of microstrip disk or circular aperture
a_e	effective disk radius at resonance
c	speed of light in vacuum
$D(\theta, \phi)$	antenna directivity
$D(\theta_m, \phi_m)$	antenna directivity in direction of beam peak
d	thickness of dielectric substrate
d_x	spacing between adjacent rows of array

d_y	spacing between adjacent columns of array
E	electric field intensity
$E(\theta, \phi)$	radiation pattern of array
E_θ	θ -component of element pattern
E_ϕ	ϕ -component of element pattern
$f(\theta, \phi)$	array factor
f_o	microstrip disk resonant frequency (first-order approximation)
f_r	microstrip disk resonant frequency
$G(\theta_m, \phi_m)$	antenna gain in direction of beam peak
$g(\theta, \phi)$	radiation pattern of isolated element
$g_{mn}(\theta, \phi)$	radiation pattern of element (m,n) in array
H	magnetic field intensity
$[I]$	identity matrix
$J_1()$	Bessel function of first kind of order one
$J_1'()$	derivative of $J_1()$ with respect to argument
j	$= \sqrt{-1}$
k_o	free space propagation constant, $2\pi/\lambda$
M	number of rows of elements in array
m	refers to mth row of array
N	number of columns of elements in array
n	refers to nth column of array
p	refers to pth row of array
q	refers to qth column of array
r, θ, ϕ	spherical coordinates
$[S]$	complex scattering matrix
$S_{mn,pq}$	complex coupling coefficient between elements (m,n) and (p,q)

$[V^+]$	matrix of complex incident voltages
$[V^-]$	matrix of complex reflected voltages
V_{mn}	total complex excitation voltage of element (m,n)
V_{mn}^+	complex incident voltage of element (m,n)
V_{pq}^+	complex incident voltage of element (p,q)
V_{mn}^-	complex reflected voltage of element (m,n)
V_1	output voltage at port 1 of hybrid
V_2	output voltage at port 2 of hybrid
v	velocity of propagation
x,y,z	Cartesian coordinates
X'_{nm}	mth zero of derivative of Bessel function of first kind and order n
X'_{n1}	first zero of derivative of Bessel function of first kind and order n
$[Y]$	complex admittance matrix
$[Y_0]$	diagonal matrix of waveguide characteristic admittances
$[Z]$	complex impedance matrix
$Z_{mn}(\theta,\phi)$	active impedance of array element (m,n)
α_{mn}	excitation phase of element (m,n)
$\Gamma_{mn}(\theta,\phi)$	active reflection coefficient of array element (m,n)
ϵ_r	dielectric constant
η	efficiency
θ_a	phase shift in arm 4 of hybrid
θ_b	phase shift in arm 3 of hybrid
θ_{HP}	half-power beamwidth
θ_m, ϕ_m	angular direction of maximum radiation
θ_s, ϕ_s	angular direction of beam scan
θ_{V1}	output phase at port 1 of hybrid

θ_{V2}	output phase at port 2 of hybrid
λ	free space wavelength
λ_{ϵ}	wavelength in dielectric substrate, $\lambda/\sqrt{\epsilon_r}$
ψ_x	incremental excitation phase between adjacent rows of array
ψ_y	incremental excitation phase between adjacent columns of array

Abbreviations:

dBi	decibels relative to an isotropic radiator
RF	radio frequency
SMA	military type specification for a connector
TE ₁₁	transverse electric mode
TM ₀	lowest order transverse magnetic surface wave mode
TM ₁₁	transverse magnetic mode
VSWR	voltage standing wave ratio

THEORY AND DESIGN OF MICROSTRIP DISK ANTENNAS

Microstrip Element

The structure of the circular disk element is shown in figure 1. The diameter of the disk is approximately one-half wavelength in the dielectric. The disk is excited by a probe from the back and the center of the disk is shorted to the ground plane as described in reference 7. The microstrip disk element being considered in this paper is similar to an earlier antenna (ref. 8) except that the present disk is excited at only one point.

Input impedance.— The microstrip disk antenna can be matched from the back directly to a 50-ohm transmission line. The input impedance is a function of the distance from the feed point to the disk center. The impedance at resonance increases from zero at the center to approximately 120 ohms at the disk edge. The 50-ohm feed point is one-third of the radius from the center of the disk. Figure 2 shows how the return loss (or reflection coefficient) varies as the frequency changes. This disk diameter is 1.86 cm on a 0.16-cm substrate with a 2.5 dielectric constant. The return loss when fed from the back at resonance is usually less than -25 dB (VSWR < 1.1).

Resonant frequency.— The microstrip disk antenna can be analyzed by considering the radiating disk and the ground plane below it as a dielectric loaded resonator with magnetic sidewalls. The resonant frequency (frequency for minimum VSWR) can then be obtained, to a first approximation, from reference 9 as:

$$f_0 = \frac{X'_{nm}c}{2\pi a\sqrt{\epsilon_r}} \quad (1)$$

where a is the disk radius, ϵ_r is the substrate dielectric constant, X'_{nm} is the m th zero of the derivative of the Bessel function of order n , and c is the speed of light in a vacuum ($c = 3 \times 10^8$ m/sec). For $m = 1$,

$$X'_{n1} = \begin{cases} 1.841 & (n = 1) \\ 3.054 & (n = 2) \\ 4.201 & (n = 3) \end{cases} \quad (2)$$

The resonant frequency for the lowest order TM mode (transverse magnetic to the disk axis) for $m = n = 1$ is

$$f_0 = \frac{1.841c}{2\pi a\sqrt{\epsilon_r}} \quad (3)$$

The calculated frequencies for the prominent resonator modes are shown in figure 3. The graph compares the calculated resonator frequencies with the measured microstrip disk return loss as a function of frequency from 2 to 10 GHz. The data were measured for a microstrip disk antenna with a 4.7-cm diameter on a 0.16-cm teflon fiber-glass substrate. The measured resonant frequencies (minimum return loss) correspond to the $m = 1$ resonator modes and indicate that the microstrip disk antenna can be viewed as a resonator for the purpose of selecting the disk size for a specified design frequency.

The resonant frequency for the TM_{11} mode can be calculated more accurately by including the influence of the edge fringing fields upon the capacitance of the microstrip resonator model. The fringing fields cause the radius of the microstrip disk to appear larger at resonance; therefore, the resonant frequency for the TM_{11} mode becomes

$$f_r = \frac{1.841c}{2\pi a_e\sqrt{\epsilon_r}} \quad (4)$$

where a_e is the effective radius of the disk due to the fringing fields and a_e is dependent upon the thickness of the dielectric substrate.

Several methods have been devised for calculating the capacitance of microstrip resonators due to fringing fields. (See refs. 10 to 13.) By using the results reported in reference 13, a simple algebraic expression for the effective disk radius was determined to be

$$a_e = a \sqrt{1 + [2d/(\pi a \epsilon_r)] \{ \log_e [\pi a/(2d)] + 1.7726 \}} \quad (5)$$

By substituting equation (5) into equation (4) and defining the wavelength in the dielectric substrate as

$$\lambda_\epsilon = c/(f_r\sqrt{\epsilon_r}) \quad (6)$$

a relationship between the resonant disk radius and the substrate thickness can be obtained as

$$(a/\lambda_e)^2 + (2/\pi\epsilon_r)(a/\lambda_e)(d/\lambda_e) \left[\log_e (\pi a/\lambda_e) - \log_e (2d/\lambda_e) + 1.7726 \right] - (1.841/2\pi)^2 = 0 \quad (7)$$

Transcendental equation (7) is plotted in figure 4 as a function of the substrate thickness in wavelength d/λ_e for various substrate dielectric constants ϵ_r . Also shown in figure 4 are some experimental data points for $\epsilon_r = 2.5$. The calculated curve for $\epsilon_r = 2.5$ is within the scatter of the experimental data for the TM_{11} mode.

Bandwidth.- The bandwidth of microstrip antenna radiators is determined primarily by the dielectric substrate thickness. The bandwidth is a linear function of thickness for substrate thickness less than 1/16 wavelength. The measured percent bandwidth as a function of substrate thickness is shown in figure 5. The data are for antennas with a substrate dielectric constant of 2.5.

Radiation patterns.- The radiation pattern of a microstrip disk antenna operating in the TM_{11} mode is similar to the pattern of an open end circular waveguide with TE_{11} mode excitation. Figures 6 and 7 compare the measured and calculated E-plane and H-plane patterns of the microstrip and waveguide antennas. The microstrip antenna resonates at 5 GHz with a 0.34 wavelength diameter on a 0.16-cm teflon fiber-glass substrate. The antenna is mounted on a 10 wavelength square ground plane. The waveguide patterns were calculated for a diameter equal to the effective resonant diameter of the disk, that is, 0.366 wavelength. The calculated circular waveguide patterns include the oscillatory variations with angle due to the finite ground plane dimensions. This calculation is accomplished by expressing the radiated field as a superposition of the field on an infinite ground plane (ref. 14) and the singularly diffracted fields from the ground plane edges (ref. 15).

The circular waveguide aperture model with an infinite ground plane (ref. 14) is very often a satisfactory model for array calculations. For the aperture in the x,y plane (the microstrip disk is also in the x,y plane) and polarized in the y-direction, the normalized element pattern in the r, θ , ϕ spherical coordinate system is

$$g(\theta, \phi) = \sqrt{E_\theta^2 + E_\phi^2} \quad (8)$$

where

$$E_\theta = \frac{2 \sin \phi J_1(k_0 a_e \sin \theta)}{k_0 a_e \sin \theta} \quad (9)$$

$$E_\phi = \frac{2 \cos \theta \cos \phi J_1'(k_0 a_e \sin \theta)}{1 - \left(\frac{k_0 a_e \sin \theta}{1.841} \right)^2} \quad (10)$$

The calculated radiation pattern for a circular waveguide aperture with an infinite ground plane is shown in figure 8. This model can be used to represent the element pattern in the design of microstrip disk antenna arrays.

Array Considerations

Many antenna applications cannot be satisfied by a simple antenna element. These applications require a combination of several identical antennas to form a single antenna array.

This section examines the factors which have a major influence on the array performance. These factors are the spatial distribution of the individual radiators and their excitation voltage. The general array characteristics are obtained from a few simple equations.

Radiation pattern.— For a planar array of radiating elements in the x,y plane (see fig. 9), the radiation pattern is

$$E(\theta, \phi) = |g(\theta, \phi) f(\theta, \phi)| \quad (11)$$

where $g(\theta, \phi)$ is the element radiation pattern and $f(\theta, \phi)$ is the array factor given by (from ref. 16, chap. 5)

$$f(\theta, \phi) = \sum_{m=1}^M \sum_{n=1}^N V_{mn} \exp \left\{ jk_0 [(m-1)d_x \sin \theta \cos \phi + (n-1)d_y \sin \theta \sin \phi] \right\} \quad (12)$$

and where V_{mn} is the complex excitation of element (m,n).

Directivity.— The directivity $D(\theta, \phi)$ is a measure of the spatial distribution of radiated energy. The directivity is defined as the ratio of the power density in the θ, ϕ direction to the average power density radiated, which can be found by integrating the radiation pattern over 4π steradians, that is,

$$D(\theta, \phi) = \frac{|g(\theta, \phi) f(\theta, \phi)|^2}{(1/4\pi) \int_0^{2\pi} \int_0^\pi |g(\theta, \phi) f(\theta, \phi)|^2 \sin \theta \, d\theta \, d\phi} \quad (13)$$

Gain and efficiency.— The directivity as given in equation (13) assumes that all the energy supplied to the antenna terminals is radiated; however, some energy is dissipated or lost within the antenna and feed network. A good measure of the performance is the actual gain of the antenna in the direction of maximum radiation; that is,

$$G(\theta_m, \phi_m) = \eta D(\theta_m, \phi_m) \quad (14)$$

where η is the efficiency of the antenna and feed network.

Beamwidth.— The beamwidth of the radiation pattern is determined by the number of elements, the element spacing, the excitation voltage amplitude dis-

tribution, and the element pattern; however, the half-power beamwidth for a long linear array with a cosine distribution can be approximated by that of a finite-length cosine line source, that is,

$$\theta_{HP} \approx \frac{68.8}{(M - 1)d_x} \text{ deg} \quad (15)$$

The half-power beamwidth for a cosine line source is plotted in figure 10 as a function of the element spacing for 8, 16, and 32 elements. The line source model is not accurate for small arrays. The beamwidth of small micro-strip arrays with cosine tapers can be estimated more accurately with the circular waveguide array model. The radiation pattern for the waveguide model $|g(\theta, \phi) f(\theta, \phi)|^2$ was calculated for a 0.366-wavelength-diameter waveguide on an infinite ground plane for 8, 16, and 32 elements (fig. 10). The data begin at 0.34 wavelength spacing although the elements cannot be spaced closer than the disk diameter.

Element spacing.— The spacing between elements determines the location of grating lobes and the maximum beam scan angle. If grating lobes are to be avoided, the element spacing is restricted to less than one free space wavelength. The element spacing in the direction of beam scanning d_x is also limited by the largest scan angle θ_s of the main beam from the array normal

$$d_x < \frac{\lambda}{1 + \sin |\theta_s|} \quad (16)$$

Element excitation.— The complex excitation voltage controls the radiation pattern beamwidth, sidelobe level, and beam pointing direction. Each radiating element of the antenna (m,n) is excited by a voltage V_{mn} from the feed network.

The main beam of the antenna points in a direction that is normal to the phase front. The phase front can be adjusted to scan the beam by controlling the phase of excitation α_{mn} to each radiating element. The voltage V_{mn} applied to each element is

$$V_{mn} = |V_{mn}| e^{-j\alpha_{mn}} \quad (17)$$

where the phase of excitation to element (m,n) is

$$\alpha_{mn} = (m - 1)\psi_x + (n - 1)\psi_y \quad (18)$$

where the excitation phase increments between consecutive columns and rows of the array are, respectively,

$$\psi_x = k_0 d_x \sin \theta_s \cos \phi_s \quad (19)$$

$$\psi_y = k_0 d_y \sin \theta_s \sin \phi_s \quad (20)$$

where θ_s and ϕ_s refer to the beam steering directions.

Mutual Coupling

The mutual coupling between radiating elements is the cause of an apparent change in the element impedance and element pattern. For example, in a scanning phased array, the impedance of each radiating element varies as the main beam is scanned. This mismatch affects the level of the radiated power, the shape of the radiation pattern, and spurious lobes. In addition, an array that is well matched at broadside may have an angle of scan in which most of the power is reflected into the feed network.

In order to describe the effects of mutual coupling, the antenna array is represented as an (M times N) port linear system which can be described by a scattering matrix. The scattering matrix represents the complex coupling coefficients between the incident and reflected voltages of each port

$$\begin{bmatrix} V_{11}^- \\ V_{12}^- \\ \vdots \\ V_{21}^- \\ V_{22}^- \\ \vdots \\ V_{MN}^- \end{bmatrix} = \begin{bmatrix} S_{11,11} & S_{11,12} & \dots & S_{11,21} & S_{11,22} & \dots & S_{11,MN} \\ S_{12,11} & S_{12,12} & \dots & S_{12,21} & S_{12,22} & \dots & S_{12,MN} \\ \vdots & \vdots & & \vdots & \vdots & & \vdots \\ S_{21,11} & S_{21,12} & \dots & S_{21,21} & S_{21,22} & \dots & S_{21,MN} \\ S_{22,11} & S_{22,12} & \dots & S_{22,21} & S_{22,22} & \dots & S_{22,MN} \\ \vdots & \vdots & & \vdots & \vdots & & \vdots \\ S_{MN,11} & S_{MN,12} & \dots & S_{MN,21} & S_{MN,22} & \dots & S_{MN,MN} \end{bmatrix} \begin{bmatrix} V_{11}^+ \\ V_{12}^+ \\ \vdots \\ V_{21}^+ \\ V_{22}^+ \\ \vdots \\ V_{MN}^+ \end{bmatrix} \quad (21)$$

or, in compact notation

$$[V^-] = [S][V^+] \quad (22)$$

The reflection coefficient Γ_{mn} of element (m,n) is obtained by dividing the reflected voltage V_{mn}^- by the incident voltage V_{mn}^+ , that is,

$$\Gamma_{mn} = \frac{V_{mn}^-}{V_{mn}^+} = \sum_{p=1}^M \sum_{q=1}^N S_{mn,pq} \frac{V_{pq}^+}{V_{mn}^+} \quad (23)$$

If the main beam is scanned in the direction (θ, ϕ) , the active reflection coefficient becomes

$$\begin{aligned} \Gamma_{mn}(\theta, \phi) &= \sum_{p=1}^M \sum_{q=1}^N S_{mn,pq} \left| \frac{V_{pq}^+}{V_{mn}^+} \right| \\ &\times \exp \left\{ jk_0 \left[(m-p)d_x \sin \theta \cos \phi + (n-q)d_y \sin \theta \sin \phi \right] \right\} \end{aligned} \quad (24)$$

The impedance of each element of the array can then be determined from the active reflection coefficient, that is,

$$Z_{mn}(\theta, \phi) = \frac{1 + \Gamma_{mn}(\theta, \phi)}{1 - \Gamma_{mn}(\theta, \phi)} \quad (25)$$

which results in a variation in impedance due to mutual coupling as the beam is scanned away from broadside.

The excitation voltage of the radiating element (m,n) is

$$V_{mn} = V_{mn}^+ - V_{mn}^- \quad (26)$$

or

$$V_{mn} = V_{mn}^+ [1 - \Gamma_{mn}(\theta, \phi)] \quad (27)$$

which shows that the excitation voltage of each element in the array also varies with scan due to coupling.

The effect of mutual coupling on the array radiation manifests itself as a change in the radiation pattern of each element. The array radiation pattern can be expressed as

$$E(\theta, \phi) = \sum_{m=1}^M \sum_{n=1}^N g_{mn}(\theta, \phi) |V_{mn}^+| e^{-j\alpha_{mn}} \times \exp \left\{ jk_0 [(m-1)d_x \sin \theta \cos \phi + (n-1)d_y \sin \theta \sin \phi] \right\} \quad (28)$$

where the element pattern $g_{mn}(\theta, \phi)$ is the actual radiation pattern taken in the array in the presence of all other elements. The element pattern $g_{mn}(\theta, \phi)$ also takes into account all coupling effects and mismatches

$$g_{mn}(\theta, \phi) = g(\theta, \phi) [1 - \Gamma_{mn}(\theta, \phi)] \quad (29)$$

where $g(\theta, \phi)$ is the radiation pattern of an isolated element.

Element patterns.— Figure 11 shows the measured element patterns of a linear 8-element array with E-plane coupling. The patterns are measured by exciting one element and terminating the other seven microstrip elements with 50-ohm loads. The patterns show that there are no serious mismatch effects in the 8-element microstrip array due to mutual coupling. In general, the coupling effects are more pronounced in larger arrays. (See ref. 17.) The dominant ripple in the patterns of figure 11 is caused by diffraction from the finite ground plane edges.

Mutual coupling coefficients.— The scattering matrix method of determining the variation in the reflection coefficient requires that each mutual coupling coefficient be determined. The mutual coupling coefficients $S_{mn,pq}$ may be measured by exciting one element and terminating each of the other elements in matched loads. (See ref. 18.) The ratio of the induced voltage at element

(m,n) to the excitation voltage at element (p,q) gives the amplitude and phase of the coupling coefficient $S_{mn,pq}$. Once these coefficients are determined, they may be substituted into equations (24) and (28) to determine the mismatch and radiation patterns for any amplitude and phase excitation of the array.

Figure 12 shows measured complex coupling coefficients for an 8-element microstrip array. The end element was excited with the other elements terminated and a swept frequency network analyzer was used to measure the RF coupling to each element. A complete description of the effects of mutual coupling for the 8-element array requires the measurement of 64 coupling coefficients (coupling between each pair combination of the array).

Two-element coupling.— If the mutual impedance for each pair combination of the array is known, the scattering matrix for the entire array can be determined:

$$[S] = [[I] + [Z]][[I] - [Z]]^{-1} \quad (30)$$

where $[I]$ is the identity matrix, $[Z]$ is the complex impedance matrix, and $[\]^{-1}$ indicates matrix inversion.

Each component of the MN by MN impedance matrix is determined by first measuring the mutual coupling of two elements out of the array, although in the same relative position and orientation as the corresponding pair of elements in the array. The mutual impedance for the pair is then found from the 2×2 matrix relation:

$$[Z]_{2 \times 2} = [[I]_{2 \times 2} + [S]_{2 \times 2}][[I]_{2 \times 2} - [S]_{2 \times 2}]^{-1} \quad (31)$$

The 2-element mutual coupling coefficients were measured for various spacings and orientations on a large ground plane. The elements were constructed on two separate teflon fiber-glass laminates and then mounted together on a large flat ground plane. The separation between the elements was varied by mounting teflon fiber-glass spacers of various widths between the coupled antennas as illustrated in figure 13.

The coupling was measured over a swept frequency range of 4.5 to 6.5 GHz with a microwave network analyzer. A typical graph of these data is shown in figure 14. The elements resonated at 5.5 GHz with less than -25-dB return loss. The maximum coupling occurs at resonance and decreases rapidly as the antennas become mismatched off resonance.

The mutual coupling as a function of the spacing between disk centers is shown in figures 15 and 16. These data are for antennas at resonance with maximum coupling. The H-plane coupling amplitude decreases rapidly as the spacing increases. However, the E-plane coupling amplitude decreases more slowly and appears to couple by means of a surface wave propagating in the lowest order TM_0 mode. The presence of other elements in an array will influence the surface wave velocity, extract power from the surface wave, and change the coupling between two elements of the array due to mutual array element interaction and scattering. This phenomenon is shown in figures 15 and 16 by comparing the measurements for two elements with those of the 8-element array.

Coupling coefficient calculation.— The array designer may require mutual coupling data for many orientations and spacings; therefore, a theoretical method of estimating coupling is described. The currents on the microstrip disk antennas are postulated to be similar to the electric field distribution for the TE_{11} circular waveguide mode. Therefore, the dual problem of coupling between dielectric-filled and covered circular waveguide-fed apertures was used to predict the coupling between the microstrip disks.

A computer program has been developed to calculate the self and mutual admittance of dielectric-filled circular waveguide-fed apertures covered by dielectric layers. (See ref. 17.) By using these calculated self and mutual admittances to form the complex admittance matrix $[Y]$, the coupling coefficients for the microstrip disk array can be estimated as

$$[S] = [[Y_0] - [Y]][[Y_0] + [Y]]^{-1} \quad (32)$$

where $[Y_0]$ is a diagonal matrix whose components are the waveguide characteristic admittance.

Figure 17 shows a comparison of the calculated waveguide coupling with the measured microstrip disk coupling data. The dielectric constant of the material inside the waveguide and of the dielectric cover is the same as that of the microstrip substrate material ($\epsilon_r = 2.5$). The microstrip disk substrate is the same thickness as the aperture dielectric cover and the waveguide diameter is the same as the diameter of the microstrip disk. Since the disk antenna is well matched at resonance and the coupling is maximum at this frequency, the computer program was modified to tune each waveguide so that the calculated coupling is also maximized. This modification is accomplished by setting the self admittance of each waveguide aperture equal to the waveguide characteristic admittance.

The E-plane calculations predict the high level of coupling for large spacings. However, the H-plane calculations are approximately 4 dB lower than the measured levels of coupling. The waveguide calculations estimate the coupling within 1 dB as the orientation angle varies from 0° to 55° as shown in figure 18. The graph is normalized to the level of E-plane coupling $\phi = 0$. The data in figure 18 were measured at resonance with a spacing of 2.3 wavelengths.

Design Procedure

A recommended procedure for the electrical design of microstrip disk antenna arrays is

(1) With the operating bandwidth and center frequency specified, the substrate thickness is selected from figure 5. For economical reasons, a commercially available stock thickness slightly greater than that dictated by figure 5 should be selected. Actually, some overdesign at this stage is advisable in order to insure that the bandwidth requirement will be met.

(2) Either equation (7) or the curves in figure 4 are used to obtain the disk size for resonance at the center operating frequency. At this stage it is

advisable to construct and test a single element to verify that the resonant frequency and bandwidth requirements are met; if not, a slight frequency scaling of the disk size should center the resonant frequency.

(3) The circular waveguide radius for radiation pattern and mutual coupling calculations is obtained from equation (5).

(4) The number of elements, amplitude excitation distribution, and element spacing to satisfy the beamwidth and sidelobe requirements are determined from pattern calculations of the waveguide array model. For cosine amplitude Butler matrix excitation, the data in figure 10 can be used to determine the required number of elements and element spacing. The maximum element spacing to avoid grating lobes is restricted by equation (16).

(5) If the main beam is to point in a direction other than normal to the array, the phase excitation distribution is determined by equation (18).

(6) By using the initial array parameters, the effects of mutual coupling upon the input impedance and radiation pattern of the microstrip disk array are calculated from the waveguide array model. If significant effects are noted, the amplitude and phase excitation coefficients should be adjusted to compensate for mutual coupling.

DEMONSTRATION ARRAYS

This section describes the performance of two C-band (5.5 GHz) arrays that were designed to demonstrate the theory and design methods described in the previous section. Microstrip disk radiating elements and stripline Butler matrix feed networks using a cosine amplitude excitation were used for the demonstration arrays. A linear array (fig. 19) was designed to produce a 20° by 85° half-power beamwidth linearly polarized fan beam broadside radiation pattern, and a planar array (fig. 20) was designed to produce a 20° by 20° half-power beamwidth linearly polarized pencil beam broadside radiation pattern. Design information is also provided so that a scanning beam feed network could be included later in place of the broadside beam network.

Array Description

The 20° half-power beamwidth is obtained from an 8-element array with a cosine-on-a-pedestal amplitude distribution and an element spacing of 0.42λ . The amplitude excitation coefficients (normalized to the array input) are

Cosine distribution		Cosine distribution	
Element number	Amplitude, dB	Element number	Amplitude, dB
1	-20.17	5	-6.15
2	-11.09	6	-7.58
3	-7.58	7	-11.09
4	-6.15	8	-20.17

A cross section of the array configuration is shown in figure 21. The radiating elements are copper disks on a copper-clad dielectric sheet. Each element is fed from the back by a stripline feed network bonded to the array. All radiators are connected through the feed network to a single common connector on the back side.

Dual copper-clad teflon fiber-glass laminates 0.16 cm thick are used for the microstrip antennas and the feed networks. The laminate is constructed from layers of glass cloth which have been impregnated with teflon. The laminate has a dielectric constant of 2.48 ± 0.04 and a dissipation factor of 0.002.

Feed Network

There are many feed network circuits which can produce a cosine amplitude excitation. For example, the sidelobe reducing cosine amplitude excitation may be obtained by using resistive or reactive attenuators. These feed network attenuators are placed in the transmission line to each array radiating element; however, for a cosine distribution using attenuators, one-half of the power would be lost in the feed system.

A sidelobe reducing network with a cosine amplitude excitation can also be implemented without attenuators. A circuit of this type is the "lossless" Butler factorial matrix. (See ref. 19.) This network produces a cosine distribution utilizing 3-dB hybrid branchline couplers and fixed phase shifters, as shown schematically in figure 22. The Butler matrix produces two uniform excitations: the first one with a phase change of positive π and the second one with a phase change of negative π . The linear superposition of these two excitations results in a cosine amplitude distribution and the resulting phase distribution produces a broadside beam.

The 64-element array is fed with the 8-element matrix described. Each matrix feeds a row of 8 microstrip disks and another network feeds each of the 8 rows (fig. 23). This combination of networks results in a pencil beam radiation pattern, whereas the single 8-element matrix produces a fan beam.

Stripline network.— The feed network can be implemented from many different types of transmission lines: stripline, coaxial, waveguide, and microstrip. The design for this project utilizes stripline transmission networks. Stripline has the advantage of being compact in size compared with coaxial and waveguide transmission lines. Stripline circuits were preferred for this application instead of microstrip to avoid radiation from unshielded lines.

Many applications use microstrip feed lines etched on the same laminate as the microstrip radiating elements. However, radiation from these microstrip feed lines may have an appreciable effect on the total radiation pattern of the array. For example, unpublished calculations made by P. K. Agrawal of George Washington University show that a microstrip 3-dB branchline coupler can radiate 14 percent of the input power.

Four branchline 3-dB hybrid directional couplers are required in the cosine Butler matrix feed network. Several individual hybrid couplers were constructed

to determine the effects of dimensional tolerances and packaging techniques (fig. 24). Figure 25 shows the amplitude and phase of the transmission through the hybrid coupler.

Figure 26 shows the center copper conductor of the stripline cosine Butler matrix feed network. The measured output amplitude and phase distributions of the network are given in figures 27 and 28. Figure 29 shows the calculated output of the phase shifters and hybrid network combination as a function of phase shift for this physical circuit configuration.

Seven stripline three-port power dividers are used in this circuit. These power dividers are simple to fabricate; however, they cannot be matched in all three ports simultaneously. Minor circuit discontinuities and the mismatched power dividers result in sidelobes which are higher than -23 dB.

Four-port power dividers (ref. 20) will improve the electrical performance at the expense of greater assembly complexity and cost. The four-port network requires that external resistors or resistive film be added to the stripline package.

Stripline packaging.- The stripline package consists of two copper-clad laminates (fig. 30). The entire assembly is secured with a film fusion bonding process; therefore, rivets are not necessary to hold the assembly together except as needed for mode suppression and shielding. Mode suppression is required for broadwall launching connections with less than $1/8$ wavelength spacing between the rivets. The stripline is self shielding; thus, many of the rivets installed in the early networks were later eliminated (fig. 31).

Beam Scanning

A possible circuit to implement a scanning system is the Butler factorial digital phase switching matrix shown schematically in figure 32. The network produces seven scanned beams with -23-dB sidelobes. The seven progressive phase distributions and cosine amplitude distributions are the result of the superposition of eight uniform amplitude distributions and linear phase distributions. Superposition and scanning is accomplished by switching in adjacent uniformly excited beams.

The far-field patterns for this network were calculated by using the waveguide aperture model for the radiating element pattern. An H-plane scanning array produces the patterns in figure 33, and the E-plane scanning array produces the patterns in figure 34.

There will be a number of variables to be considered in the design of the scanning array. For example, one consideration is the large scan angle grating lobes which begin to appear for a 0.5 wavelength spacing as in figure 34. For the same scan angle, a 0.42 wavelength element spacing will decrease the effect of the grating lobe; however, the half-power beamwidth of the main lobe will increase. A good design would consider the tradeoff between limited scanning, element spacing, and beamwidth.

Radio Frequency Performance Characteristics

This section compares the measured RF performance of the microstrip disk and the low sidelobe linear and planar microstrip arrays. The three experimental C-band antennas considered were:

- (1) The circular disk microstrip antenna
- (2) The 8-element linear microstrip array with a Butler matrix feed network
- (3) The 64-element planar microstrip array with a Butler matrix feed network

The measured performance of each antenna is summarized in table I.

A complete description of the far-field radiation requires intensity measurements over the entire sphere of polar coordinate aspect angles, 4π steradians. Each linearly polarized test antenna was measured in an indoor anechoic test range using a circularly polarized horn to illuminate the test antenna in order to avoid the polarization mismatch problem when making measurements over a complete sphere. Figure 35 shows the 64-element array mounted on a pedestal in the antenna test facility. The antenna rotation is controlled from the chamber console (fig. 36), and the data are recorded on magnetic tape.

The antenna patterns are recorded in 2° increments in both θ and ϕ ; θ is increased in 2° increments from 0° to 180° as ϕ varies continuously from 0° to 360° . A complete recording consists of 91 scans with a total of 16380 data points.

Directivity.— The radiation pattern data are integrated over 4π steradians to determine the antenna's directivity. The maximum directivity at the beam peak increases with frequency as shown in figure 37 for each test antenna.

Volumetric patterns.— The recorded radiation pattern at a given frequency is displayed as a volumetric false color plot in which the directivity values that fall within specified ranges are assigned a color. The computer-generated false color plots are displayed on a television screen and then photographed to provide a single volumetric pattern.

The volumetric patterns are presented in two forms. The first presentation (figs. 38 to 40) displays the directivity values relative to an isotropic radiator as shades of gray within seven ranges: ≥ 0 dBi, ≥ -3 dBi, ≥ -6 dBi, ≥ -10 dBi, ≥ -15 dBi, ≥ -20 dBi, and < -20 dBi. The second presentation (figs. 41 to 43) displays the directivity values relative to the peak of the main beam instead of relative to isotropic directivity. The normalized directivity levels relative to the beam peak are (0 to -3 dB), (-3 to -6 dB), (-6 to -10 dB), (-10 to -15 dB), (-15 to -20 dB), (-20 to -25 dB), and (< -25 dB). The lightest shade of grey in figures 41, 42, and 43 represents the half-power beamwidth for each antenna.

Principal plane patterns.- Comprehensive pattern surveys are often necessary; however, for many applications it is possible to obtain sufficient information with pattern measurements in the principal (E and H) planes. In order to measure the co-polarized and cross-polarized components, a linearly polarized transmitting horn was used to illuminate the test antennas in the anechoic test range. The principal plane patterns for the three test antennas are given in figures 44 to 46.

Sidelobes.- The sidelobe structure for each array varies with frequency as observed in figures 47 and 48. The first sidelobe level plotted against frequency from these patterns is shown in figure 49 from 5.0 to 6.0 GHz. The sidelobe level varies from -20 to -23.5 dB in the frequency range of 5.3 to 5.8 GHz. The level varies principally because of errors in the amplitude and phase of the excitation from the stripline feed network.

Gain and efficiency.- The gain of each antenna relative to the gain of an isotropic radiator was measured with a swept frequency receiver using a standard gain horn as a reference. The gain and directivity are compared in figure 37 from 5.0 to 6.0 GHz. The efficiency of the antenna can be determined from the ratio of the gain and directivity at the peak of the main lobe. The maximum efficiencies at 5.5 GHz for the single microstrip element, 8-element array, and 64-element array are 79 percent, 78 percent, and 69 percent, respectively. These efficiencies include the losses in the feed networks for each antenna.

Impedance.- The measurement of impedance is made at the single input port of each antenna system with a swept frequency network analyzer (fig. 50). The network analyzer characterizes the antenna in terms of the complex small-signal scattering parameters as a function of frequency. The scattering parameters determine the magnitude and phase of the reflection coefficient which is displayed on a Smith chart in figures 51 to 53. The scattering parameters and the Smith chart are normalized to a 50-ohm characteristic impedance.

Bandwidth.- The measured 3:1 VSWR bandwidths at 5.5 GHz for the single element, 8-element linear array, and 64-element planar array are 7.5 percent, 8 percent, and 2 percent, respectively.

CONCLUDING REMARKS

Design data was presented for microstrip elements and arrays including the mutual interaction between elements and the stripline feed network design for a cosine amplitude excitation distribution. Utilizing this design data, two C-band low sidelobe arrays were fabricated and tested: an 8-element linear and a 64-element planar array. These arrays incorporated stripline Butler matrix feed networks to produce a low sidelobe broadside beam.

Good agreement was obtained between the measured and calculated radiation patterns including the half-power beamwidth and the sidelobes. The sidelobes were designed for a -23-dB level. The measured sidelobes for both arrays were less than -20 dB for an 11-percent bandwidth.

The performance of the low sidelobe broadside beam arrays indicates that a low sidelobe scanning array utilizing the Butler factorial digital phase switching matrix will be practical to implement.

The design data in this paper do not include the effects of adding a thermal protective cover to the array. However, preliminary data indicate that for dielectric covers less than $1/16$ wavelength, the general effects upon the performance of a single microstrip element are an additional decrease of the resonant frequency of less than 2 percent and an additional increase in bandwidth of up to 2 percent.

Langley Research Center
National Aeronautics and Space Administration
Hampton, VA 23665
December 12, 1977

REFERENCES

1. Munson, Robert: Microstrip Phase D Array Antennas. M72-06, Twenty-Second Annual Symposium USAF Antenna Research and Development Program (Monticello, Illinois), Oct. 1972.
2. Munson, Robert; and Murphy, Lawrence: Conformal Microstrip Array for a Parabolic Dish. Twenty-Third Annual Symposium USAF Antenna Research and Development Program (Monticello, Illinois), Oct. 1973. (Available from DDC as AD 914-238L.)
3. Munson, Robert E.: Conformal Microstrip Antennas and Microstrip Phased Arrays. IEEE Trans. Antennas & Propag., vol. AP-22, no. 1, Jan. 1974, pp. 74-78.
4. Sanford, Gary G.: Conformal Microstrip Phased Array for Aircraft Tests With ATS-6. Proceedings of the National Electronics Conference, Volume XXIX, David L. Cohn and Gregory S. Lauer, eds., National Engineering Consortium, Inc., Oct. 1974, pp. 252-257.
5. Weinschel, Henry D.: A Cylindrical Array of Circularly Polarized Microstrip Antenna. IEEE AP-S International Symposium (Urbana, Illinois), 1975, pp. 177-180.
6. Campbell, T. G.; Appleton, M. W.; and Lusby, T. K.: The Design and Fabrication of Microstrip Omnidirectional Array Antennas for Aerospace Applications. NASA TM X-73979, 1976.
7. Howell, John Q.: Microstrip Antennas. IEEE Transactions Antennas and Propagation, vol. AP-23, no. 1, Jan. 1975, pp. 90-93.
8. Brain, D. J.; and Mark, J. R.: The Disc Antenna. A Possible L-Band Aircraft Antenna. Proceedings IEEE International Conference (London, England), Mar. 1973, pp. 14-17.
9. Watkins, J.: Circular Resonant Structures in Microstrip. Electronic Letters, vol. 5, no. 21, Oct. 1969, pp. 524-525.
10. Itoh, T.; and Mittra, R.: A New Method for Calculating the Capacitance of a Circular Disk for Microwave Integrated Circuits. IEEE Trans. Microwave Theory & Tech., vol. MTT-21, no. 6, June 1973, pp. 431-432.
11. Wolff, Ingo; and Knoppik, Norbert: Rectangular and Circular Microstrip Disk Capacitors and Resonators. IEEE Trans. Microwave Theory & Tech., vol. MTT-22, no. 10, Oct. 1974, pp. 857-864.
12. Borkar, Suresh R.; and Yang, Richard F. H.: Capacitance of a Circular Disk for Applications in Microwave Integrated Circuits. IEEE Trans. Microwave Theory & Tech., vol. MTT-23, no. 7, July 1975, pp. 588-591.

13. Shen, L. C.; Long, S. A.; Allerdin, M. R.; and Walton, M. D.: Resonant Frequency of a Circular Disc, Printed-Circuit Antenna. IEEE Trans. Antennas & Propag., vol. AP-25, no. 4, July 1977, pp. 595-596.
14. Bailey, M. C.; Samaddar, S. N.; and Swift, Calvin T.: Electromagnetic Properties of a Circular Aperture in a Dielectric-Covered or Uncovered Ground Plane. NASA TN D-4752, 1968.
15. Balanis, C. A.: Pattern Distortion Due to Edge Diffractions. IEEE Trans. Antennas & Propag., vol. AP-18, no. 4, July 1970, pp. 561-563.
16. Collin, Robert E.; and Zucker, Francis J.: Antenna Theory. Part 1. McGraw-Hill Book Co., Inc., c.1969.
17. Bailey, M. C.: Analysis of Finite-Size Phased Arrays of Circular Waveguide Elements. NASA TR R-408, 1974.
18. Oliner, A. A.; and Malech, R. G.: Mutual Coupling in Infinite Scanning Arrays. Microwave Scanning Antennas, Vol. II, R. C. Hansen, ed., Academic Press, Inc., 1966, pp. 195-335.
19. Butler, Jesse L.: Digital, Matrix, and Intermediate-Frequency Scanning. Microwave Scanning Antennas, Vol. III, R. C. Hansen, ed., Academic Press, Inc., 1966, pp. 217-288.
20. Howe, Harlan: Stripline Circuit Design. Artech House (Dedham, Mass.), [1974].

TABLE I.- SUMMARY OF RADIO FREQUENCY PERFORMANCE

	Microstrip disk	8-element linear array	64-element planar array
3-dB beamwidth:			
E-plane, deg	110	20	19
H-plane, deg	85	83	20
First sidelobe level:			
E-plane, dB	---	-20.5	-22.5
H-plane, dB	---	-----	-20.0
Directivity, dB	7.6	13.5	20.2
Gain, dB	6.6	12.4	18.6
Efficiency, percent	79	78	69
Bandwidth (VSWR < 3:1), percent . . .	7.5	8	2

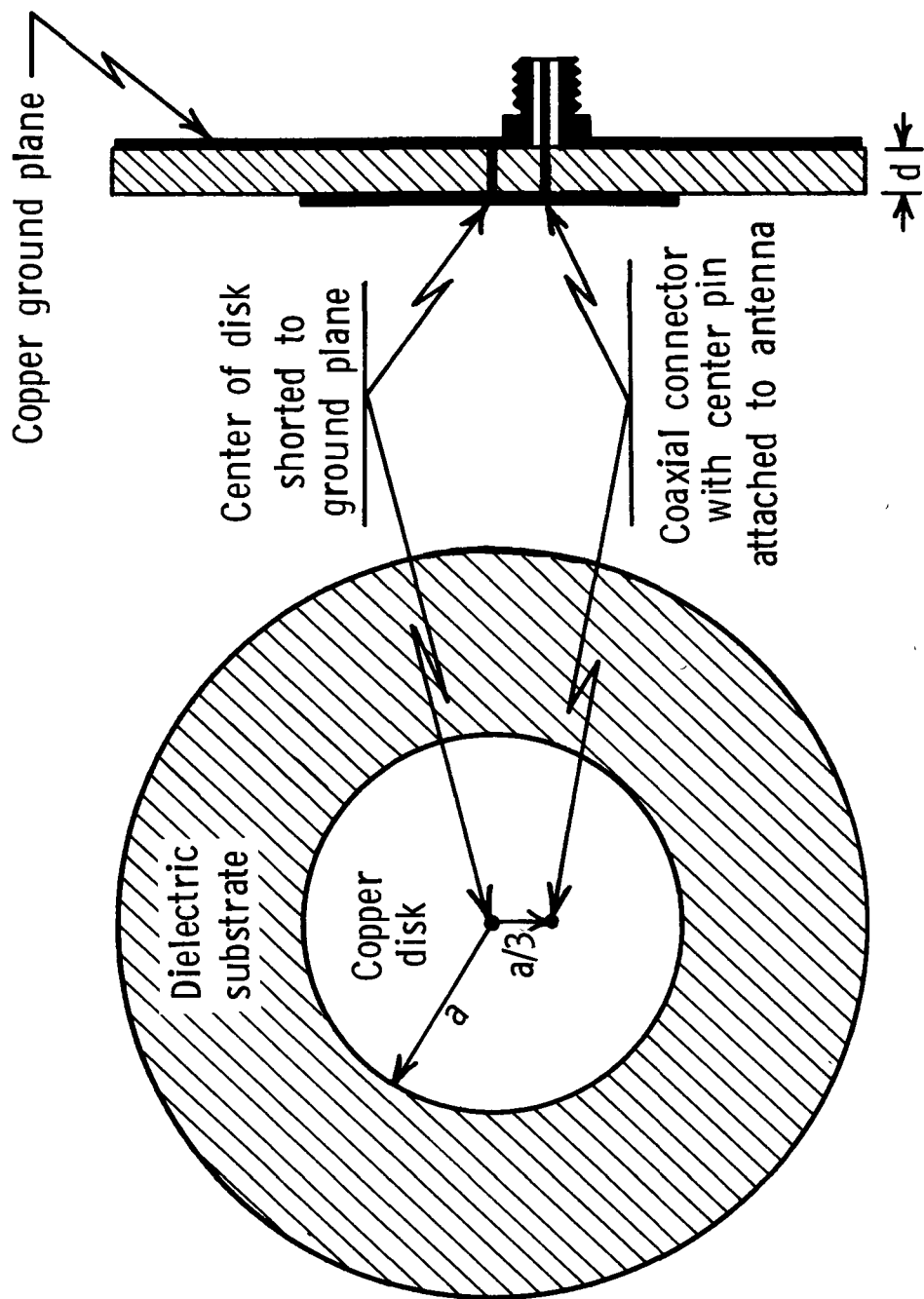


Figure 1.- Microstrip disk antenna fed from back.

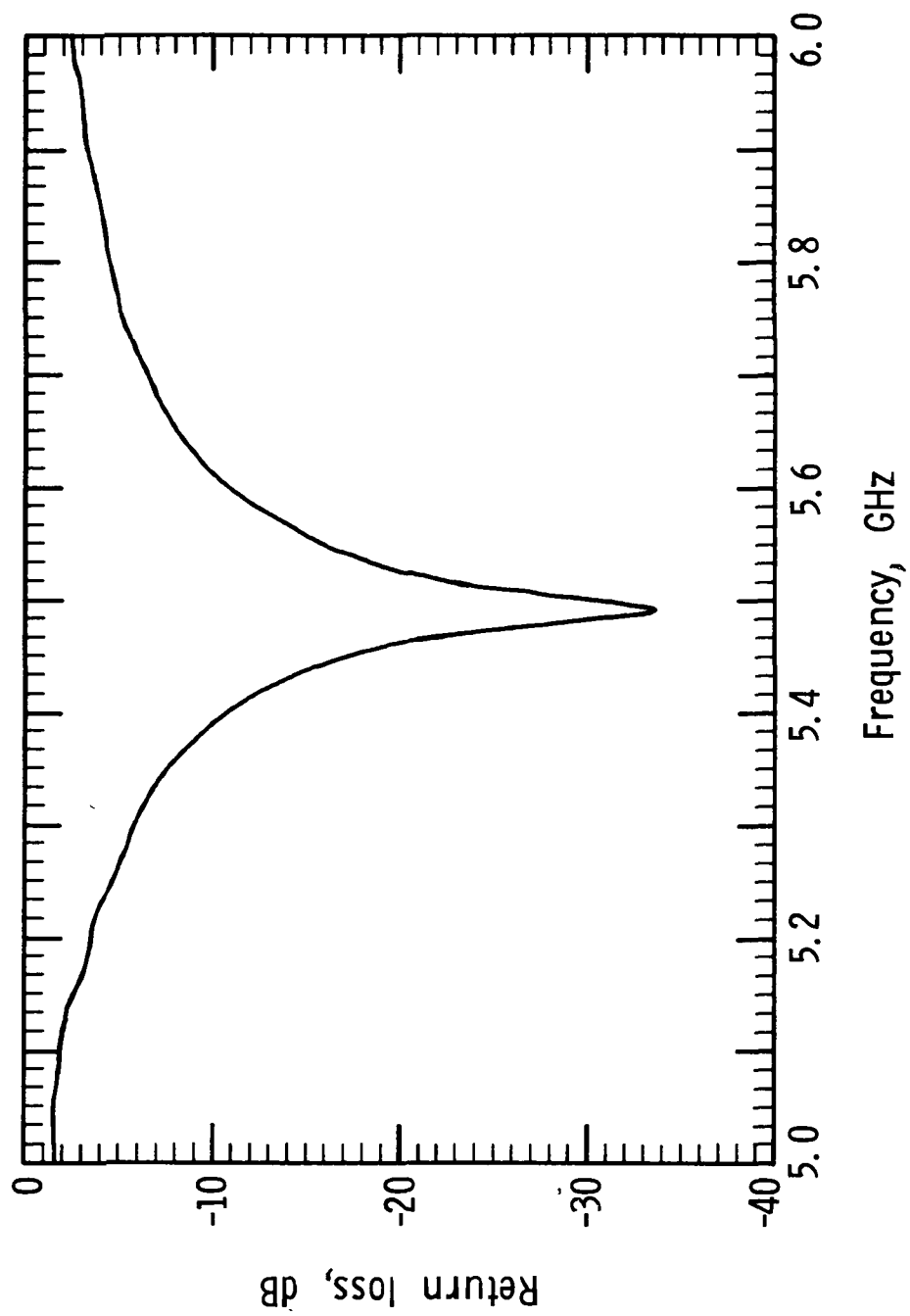


Figure 2.- Measured return loss of a microstrip disk antenna.

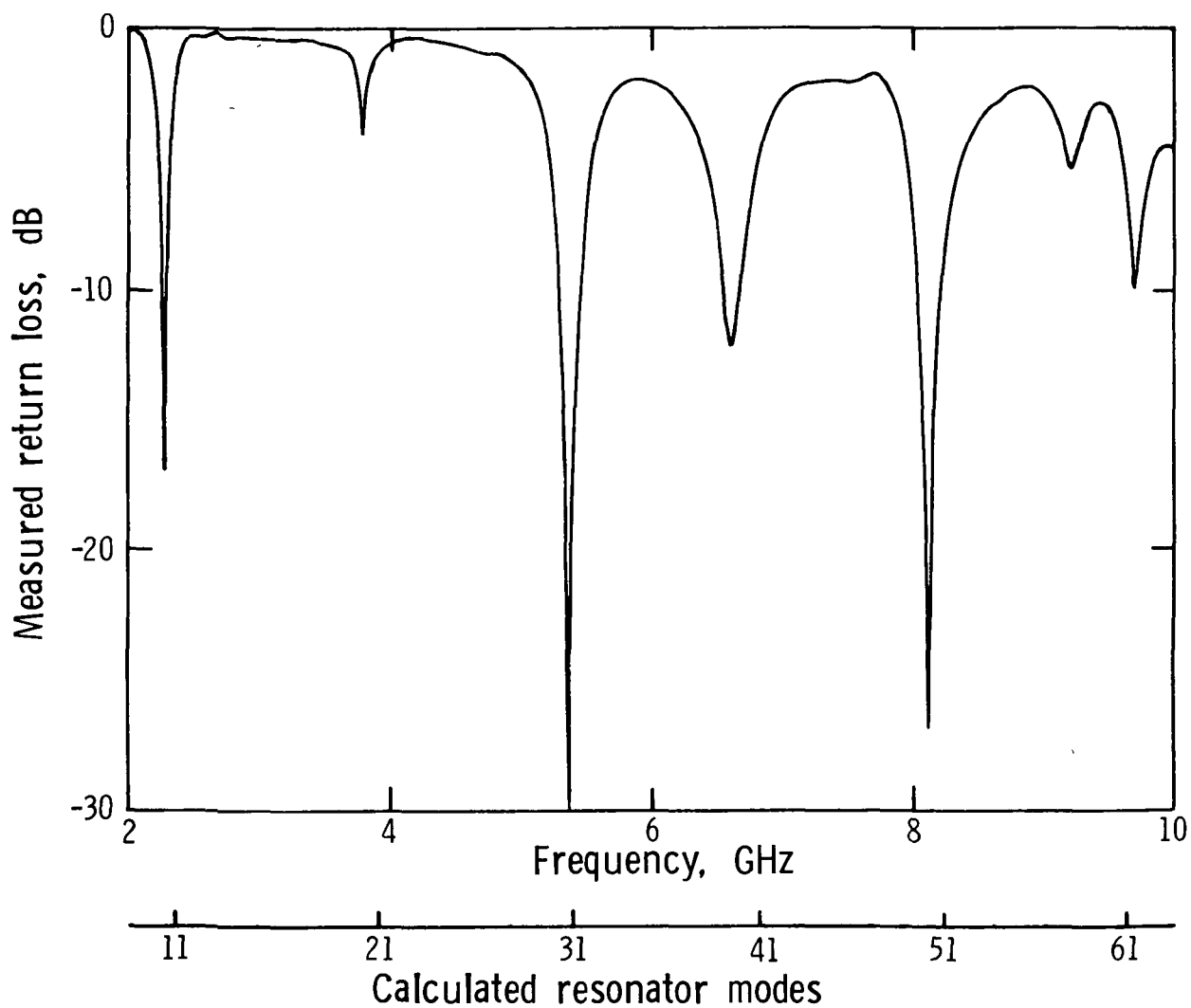


Figure 3.- Input return loss characteristics and calculated resonator modes for a 4.7-cm-diameter microstrip disk on a 0.16-cm-thick substrate.

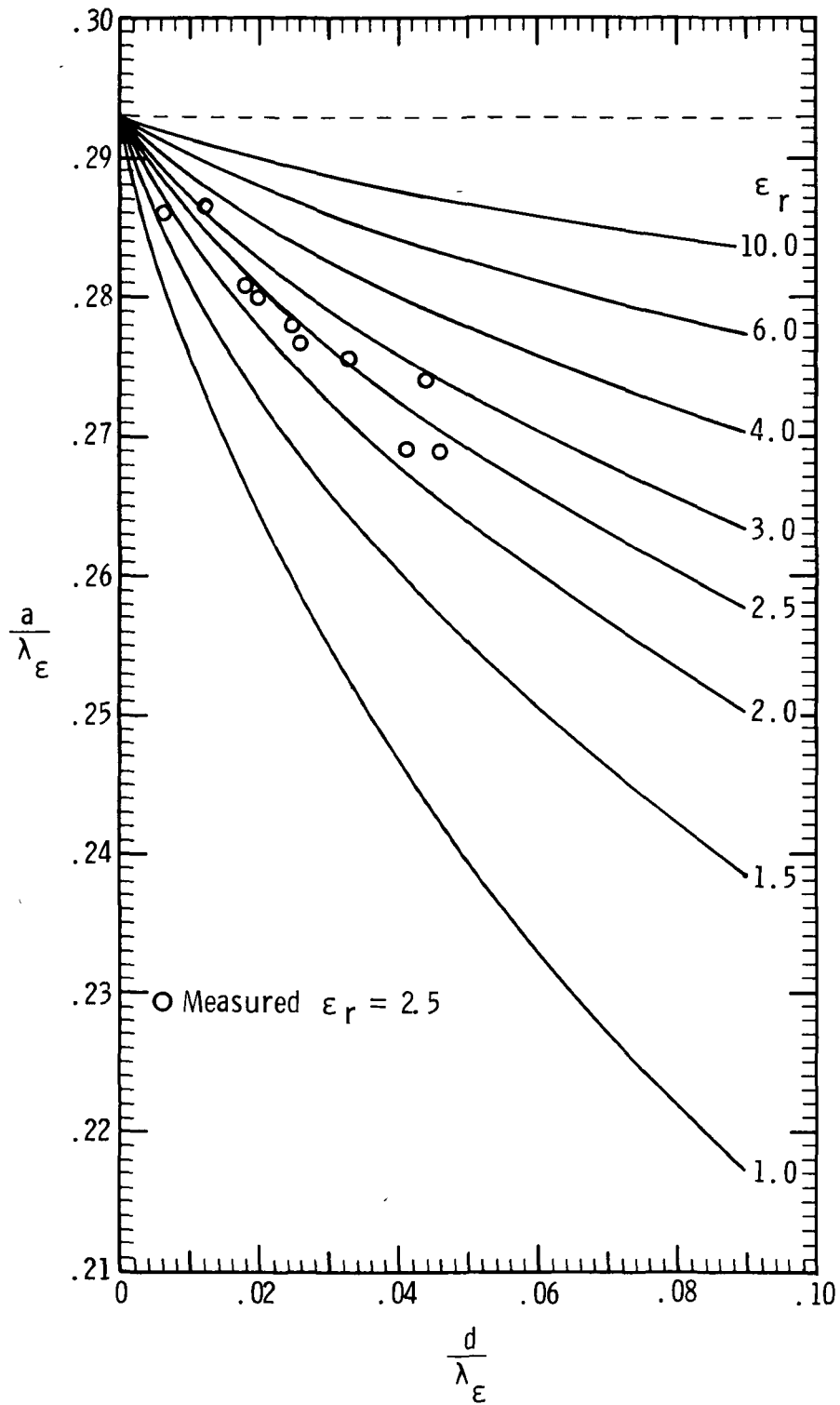


Figure 4.- Resonant disk size as a function of substrate thickness for TM_{11} mode microstrip disk antennas.

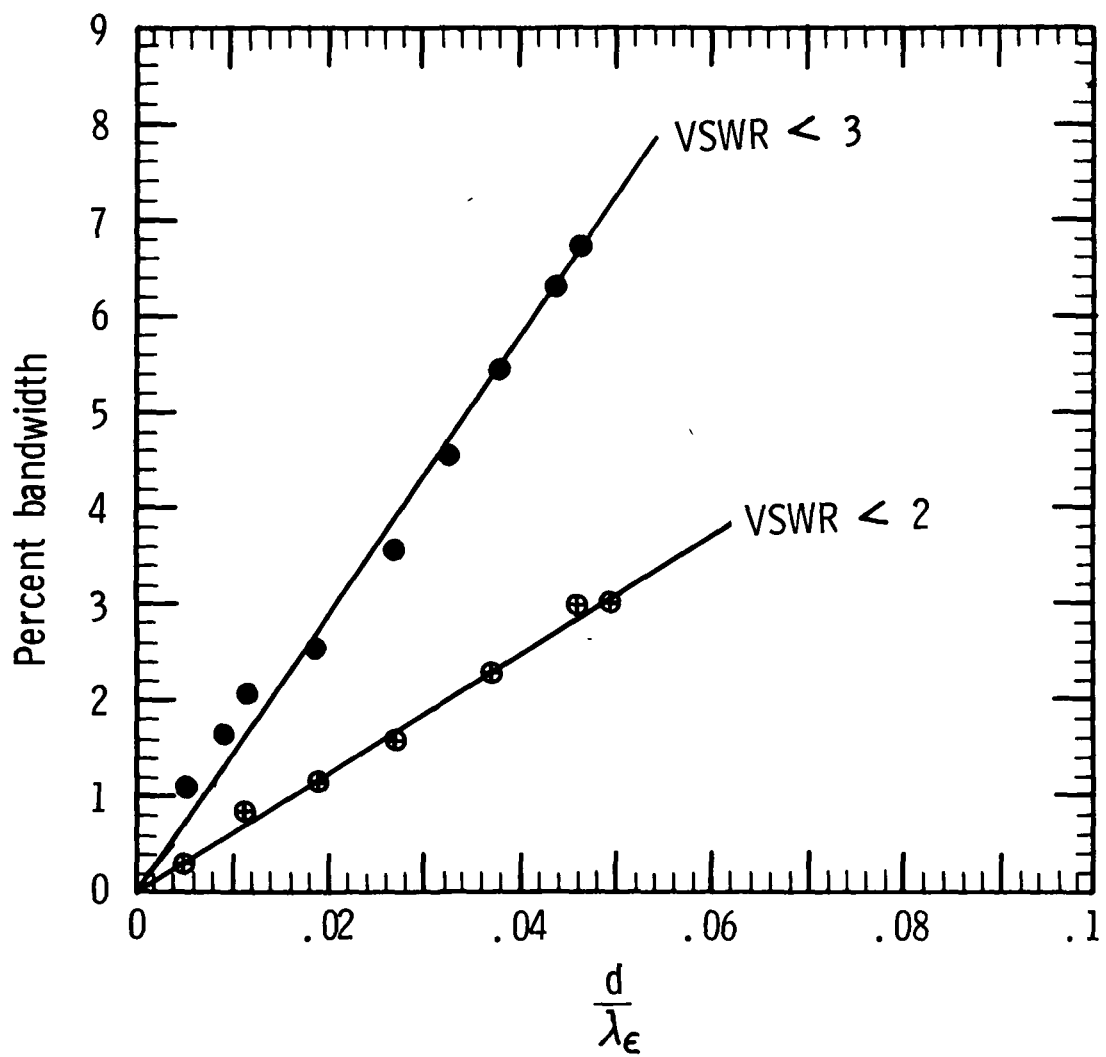


Figure 5.- Percent bandwidth of a microstrip disk antenna as a function of substrate thickness in wavelengths for $\epsilon_r = 2.5$.

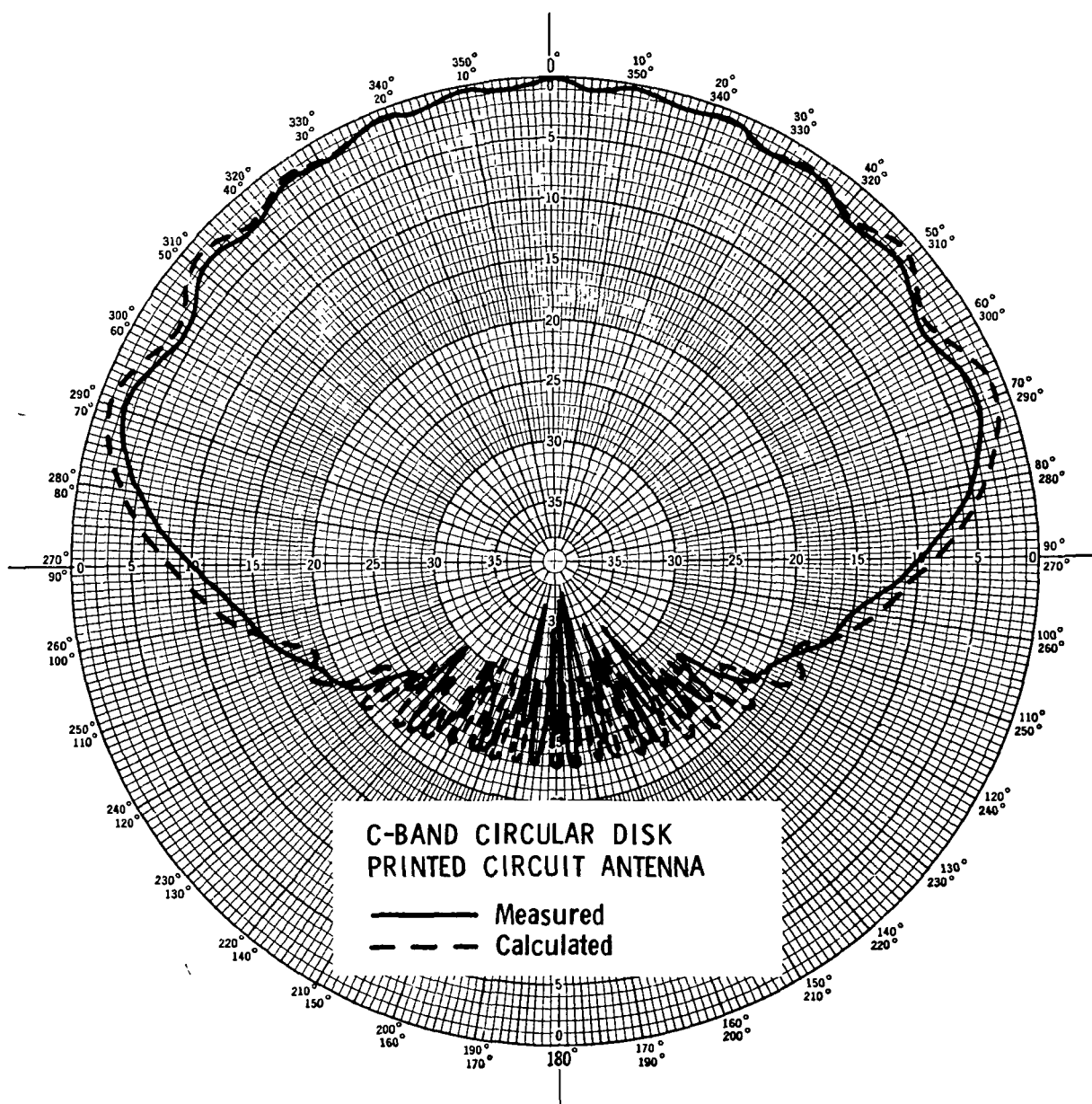


Figure 6.- E-plane pattern of a 5-GHz microstrip disk antenna on a 62-cm ground plane.

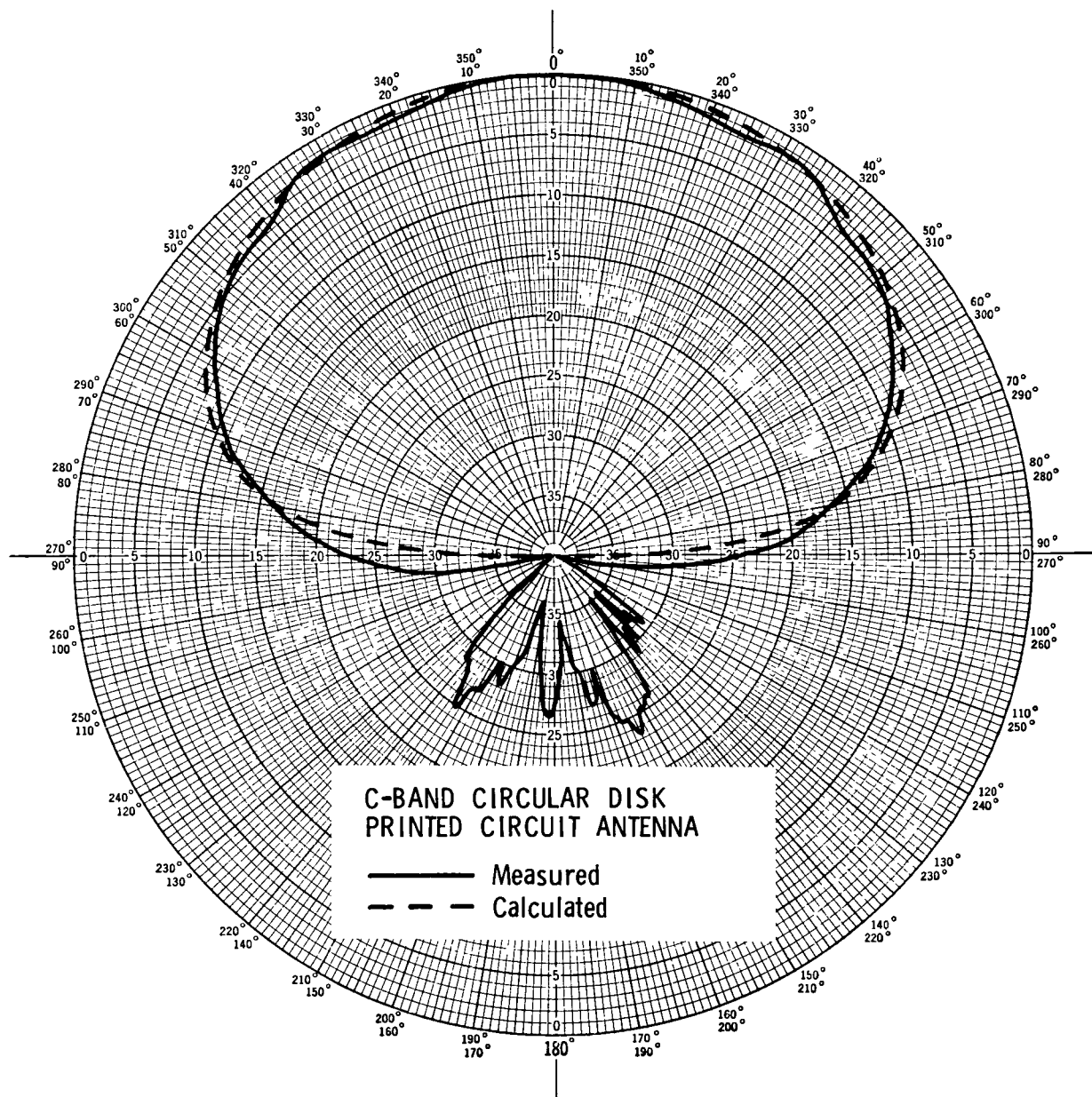


Figure 7.- H-plane pattern of a 5-GHz microstrip disk antenna on a 62-cm ground plane.

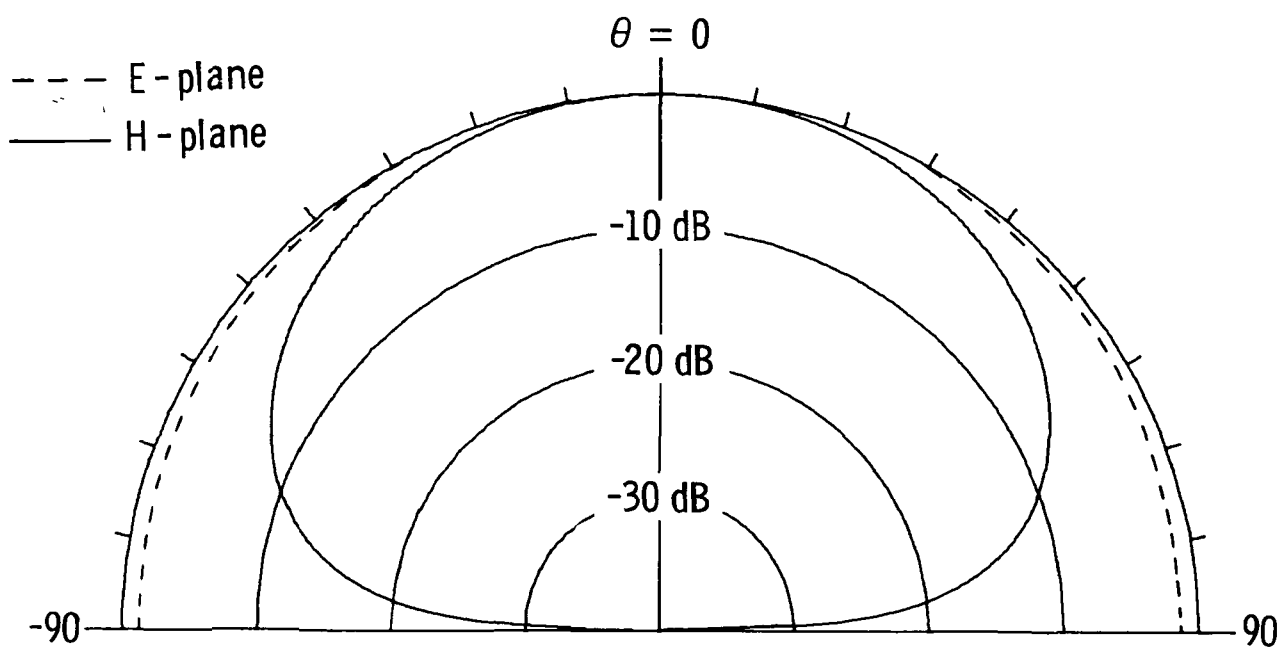


Figure 8.- Calculated radiation pattern of a circular aperture on an infinite ground plane.

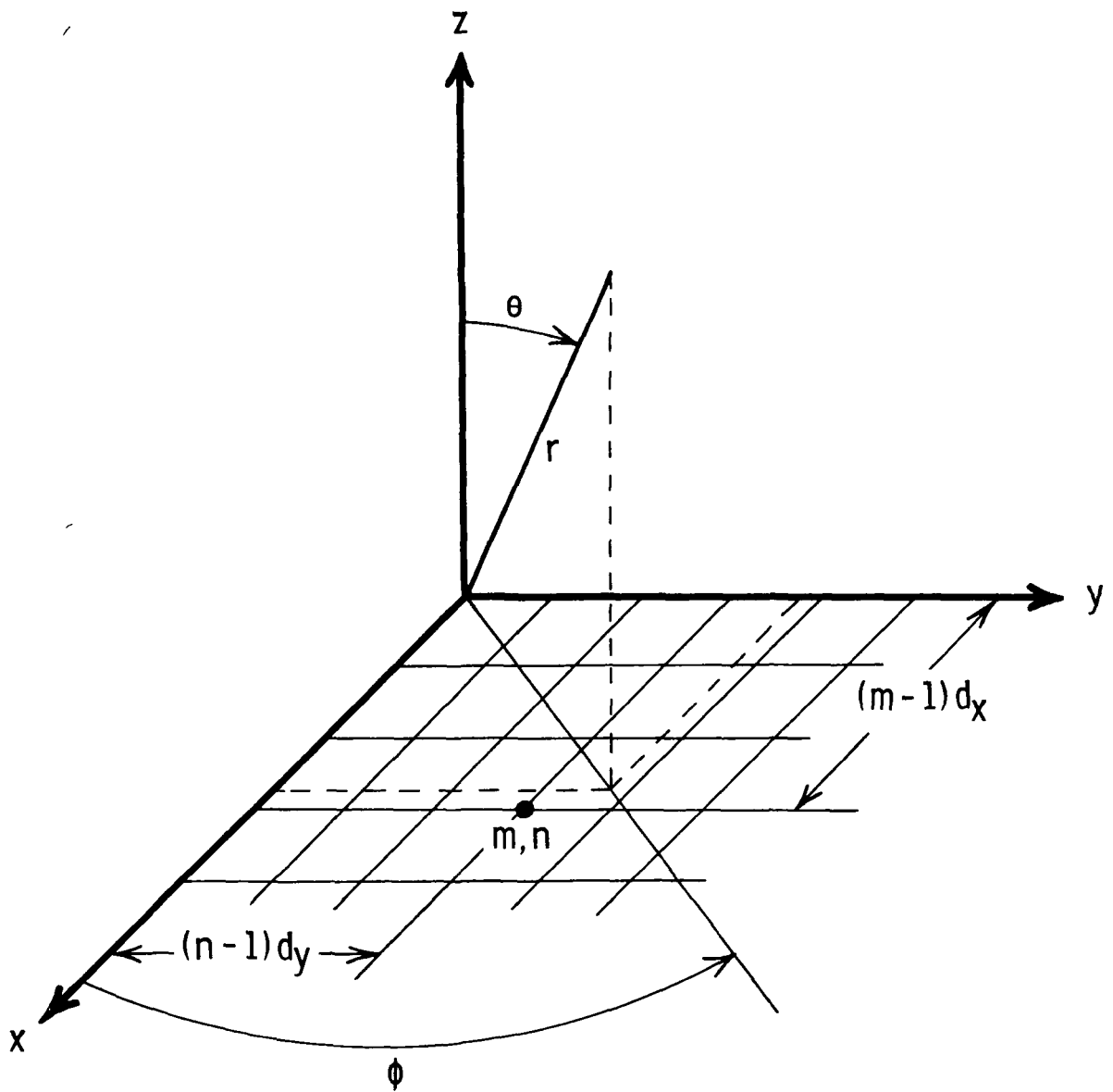


Figure 9.- Array coordinate system.

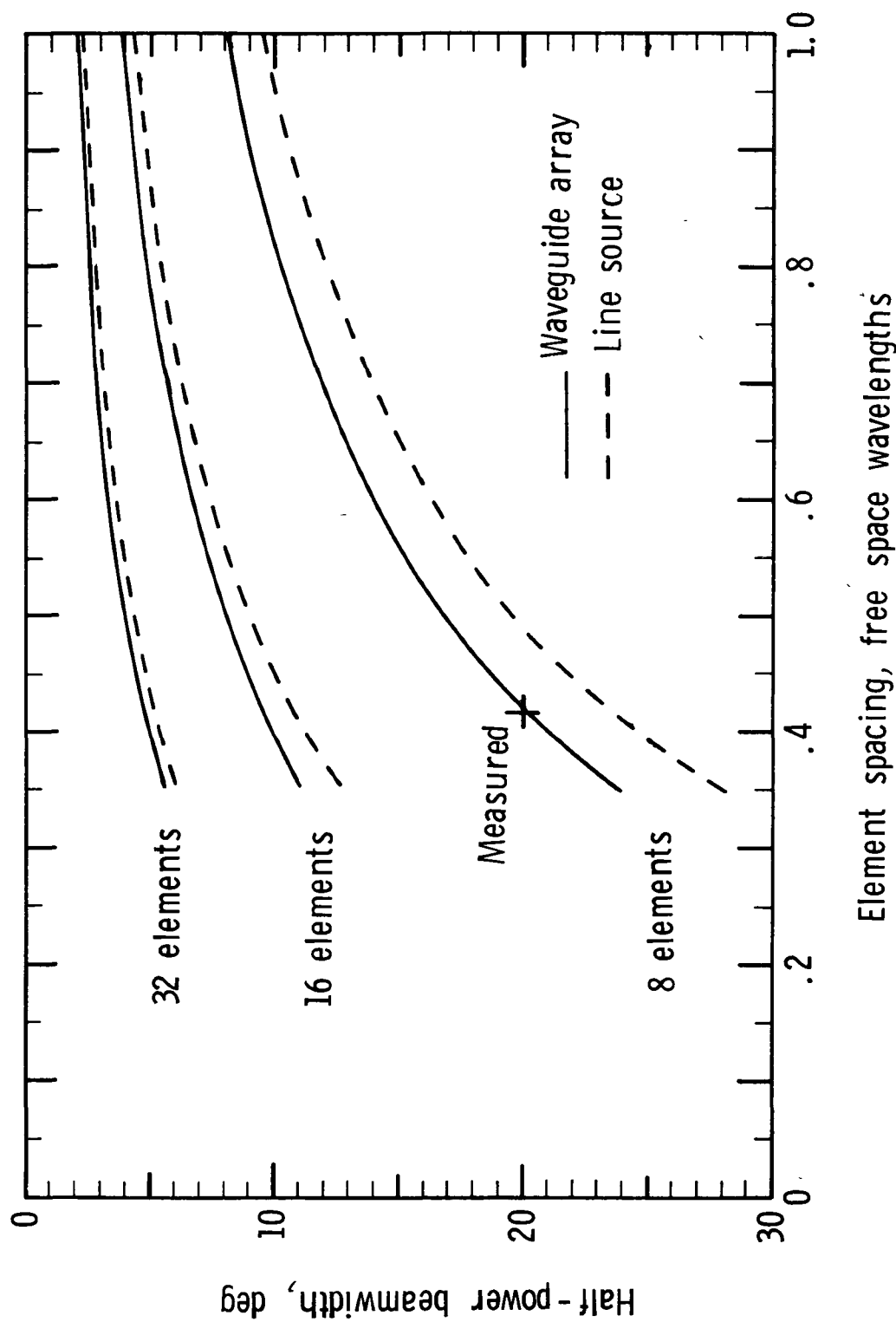
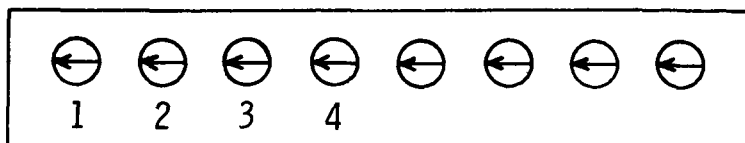


Figure 10.- Half-power beamwidth of microstrip arrays with cosine amplitude excitation.



0.42 wavelength element spacing

Frequency = 5.5 GHz

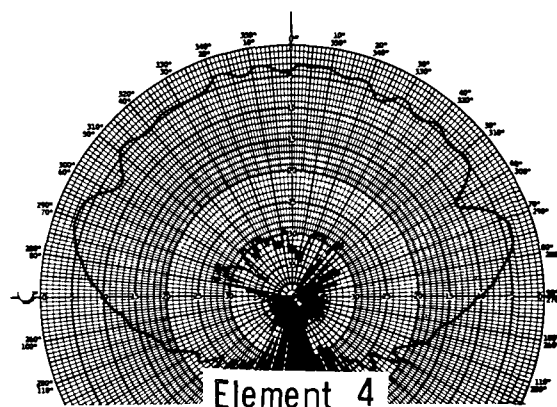
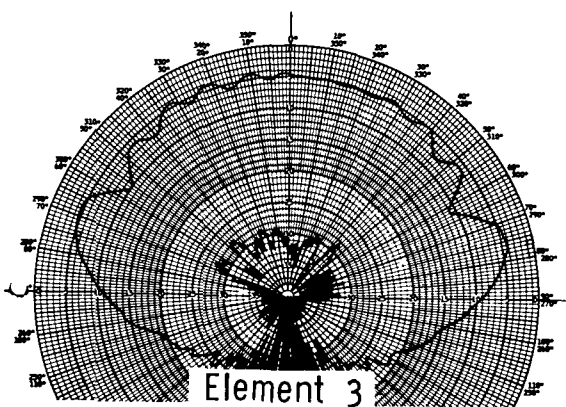
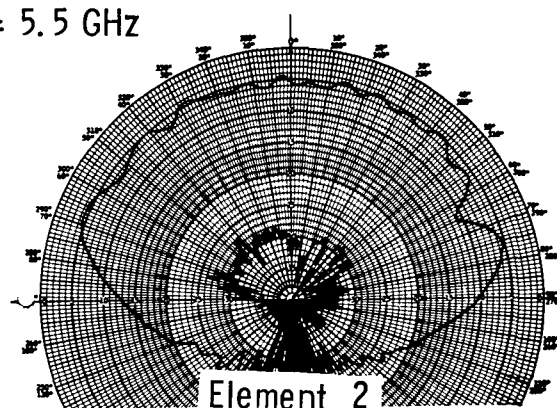
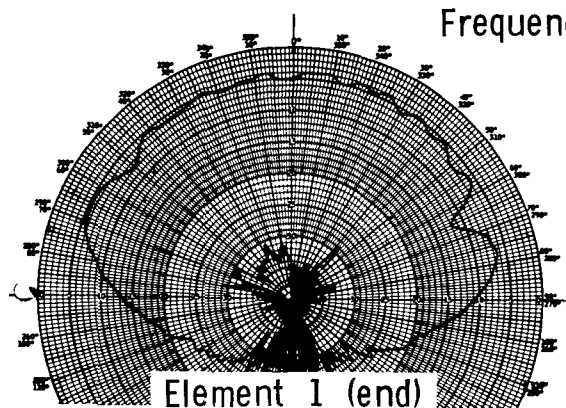


Figure 11.- E-plane element patterns for an 8-element linear array with 1 element excited and other 7 elements terminated.

E-plane coupling
 0.16-cm substrate, $\epsilon_r = 2.5$
 0.42 wavelength spacing
 Frequency = 5.5 GHz

[Amplitude, dB
 Phase, 360° periods]

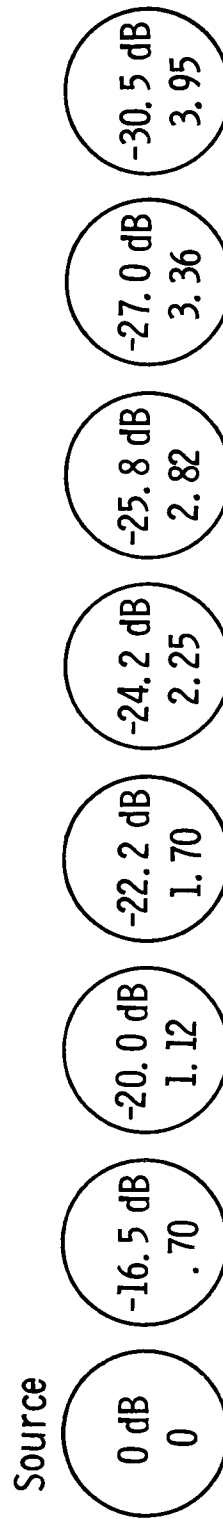


Figure 12.- Measured mutual coupling coefficients in an 8-element linear microstrip disk array.

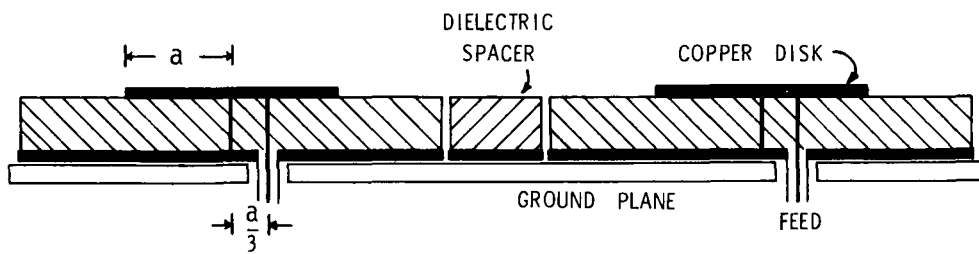


Figure 13.- Cross section of coupled disk antennas.

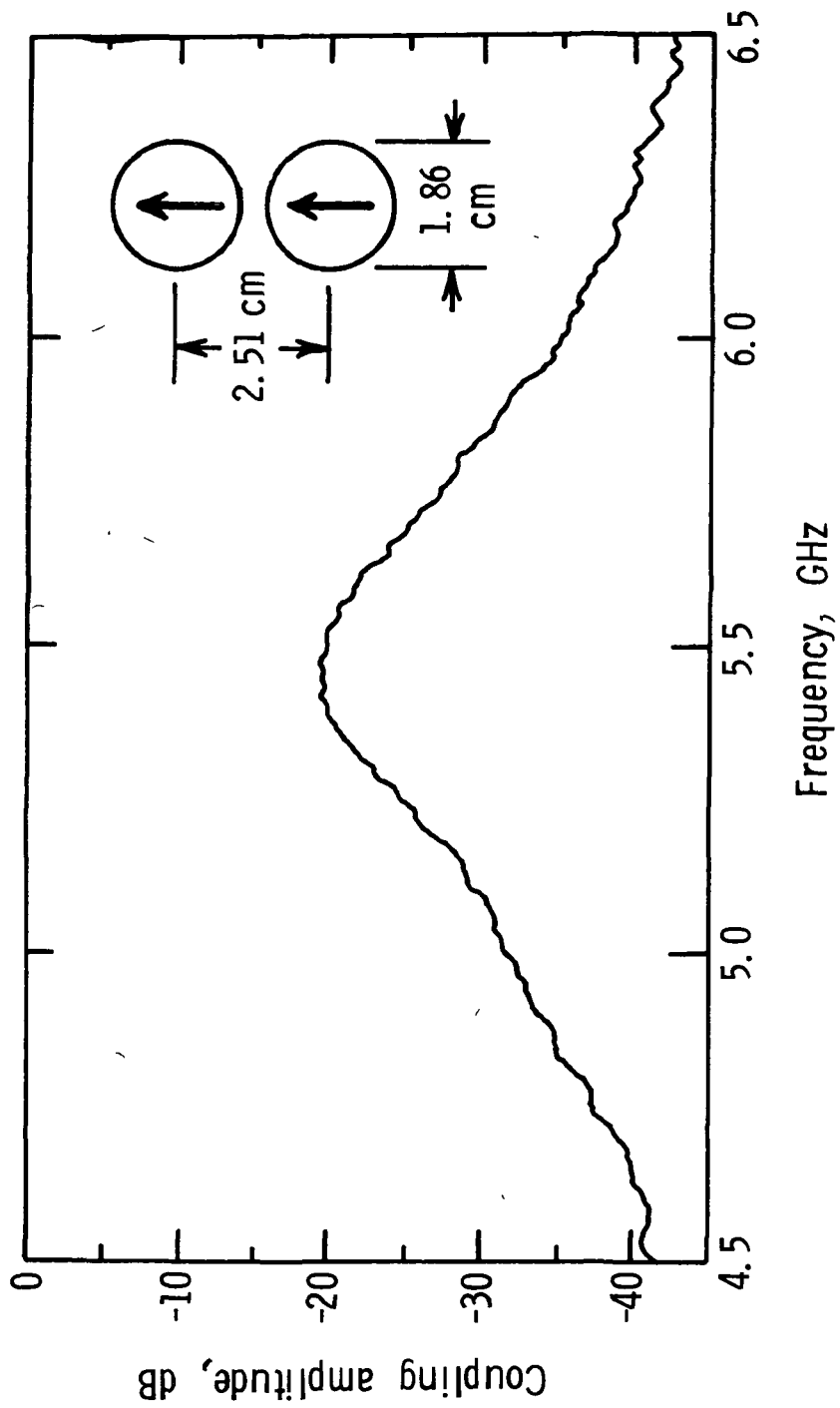


Figure 14.- Swept frequency coupling amplitude data between two microstrip disks.

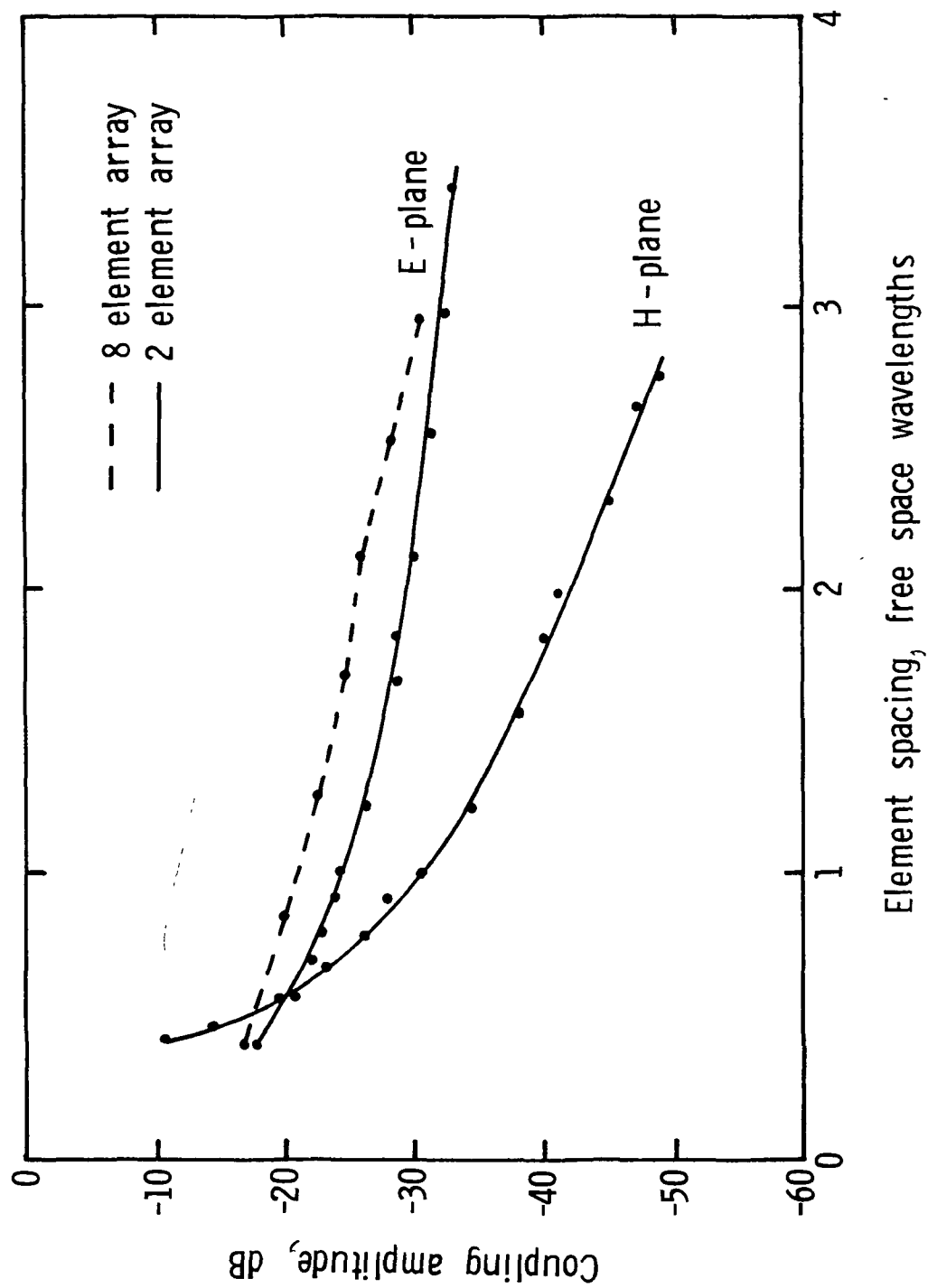
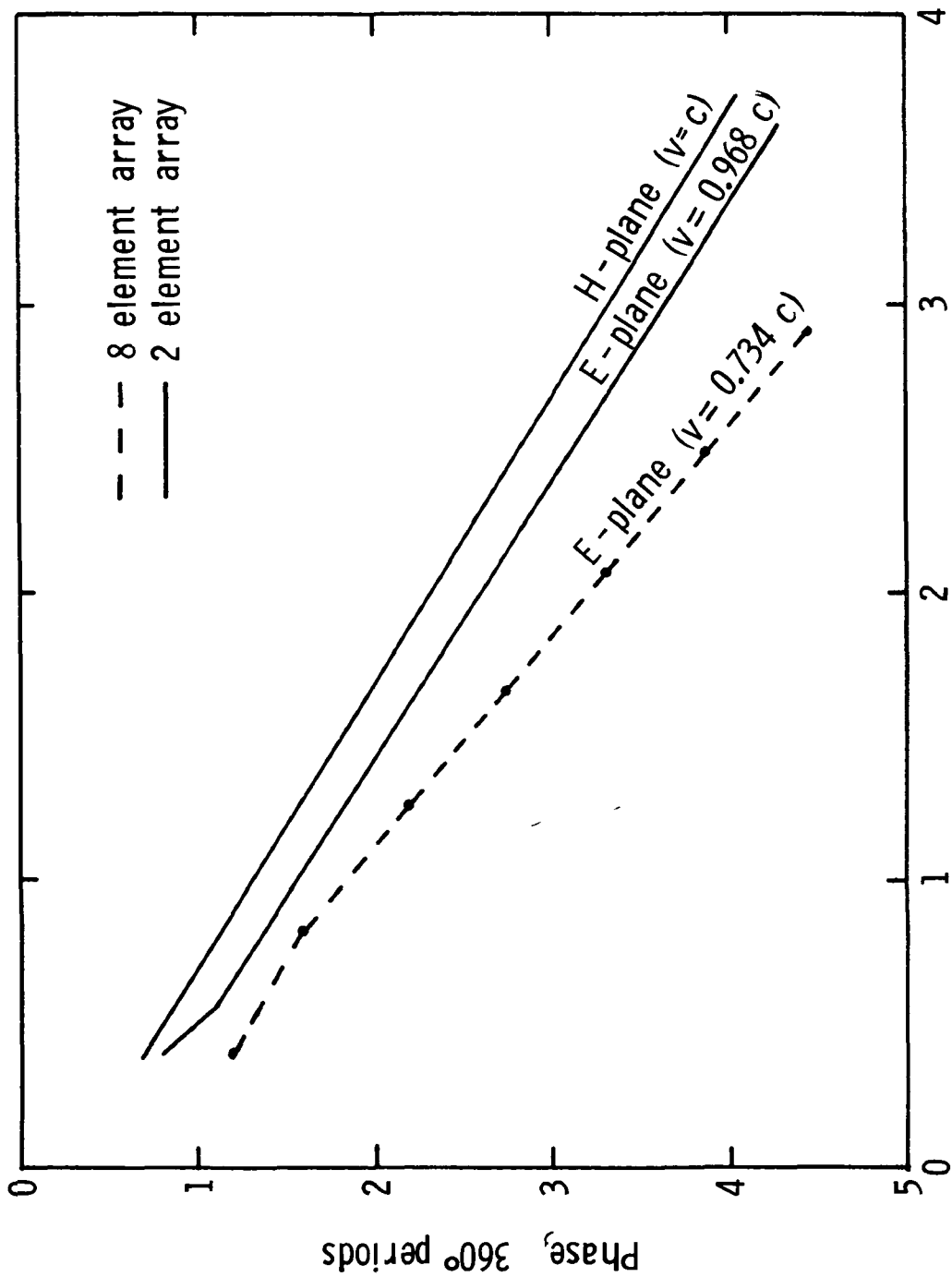


Figure 15.- Measured amplitude of mutual coupling coefficients for microstrip disks as a function of spacing.



Element spacing, free space wavelengths

Figure 16.- Measured phase of mutual coupling coefficients for microstrip disks as a function of spacing.

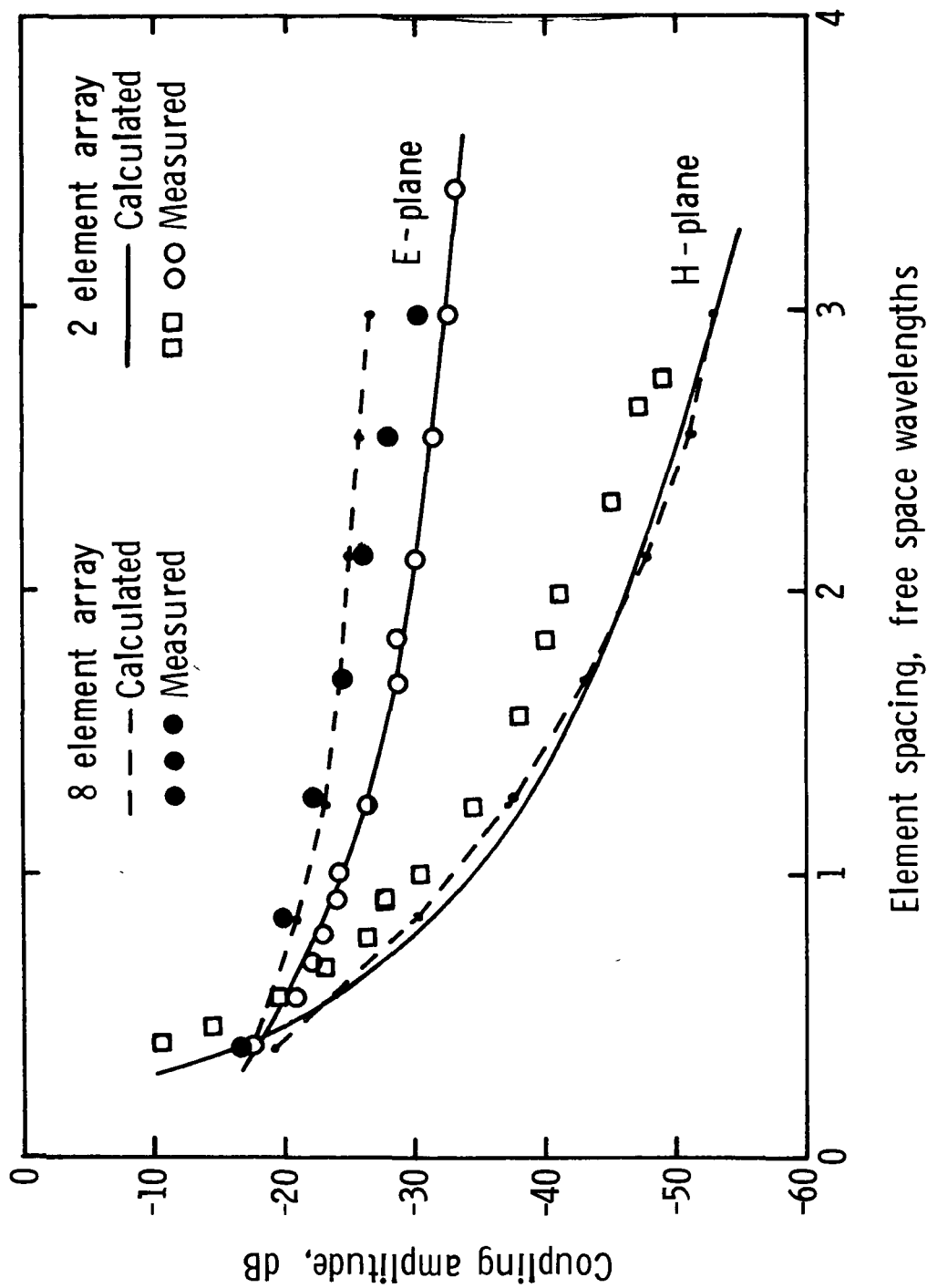


Figure 17.- Comparison of calculated and measured mutual coupling as a function of spacing.

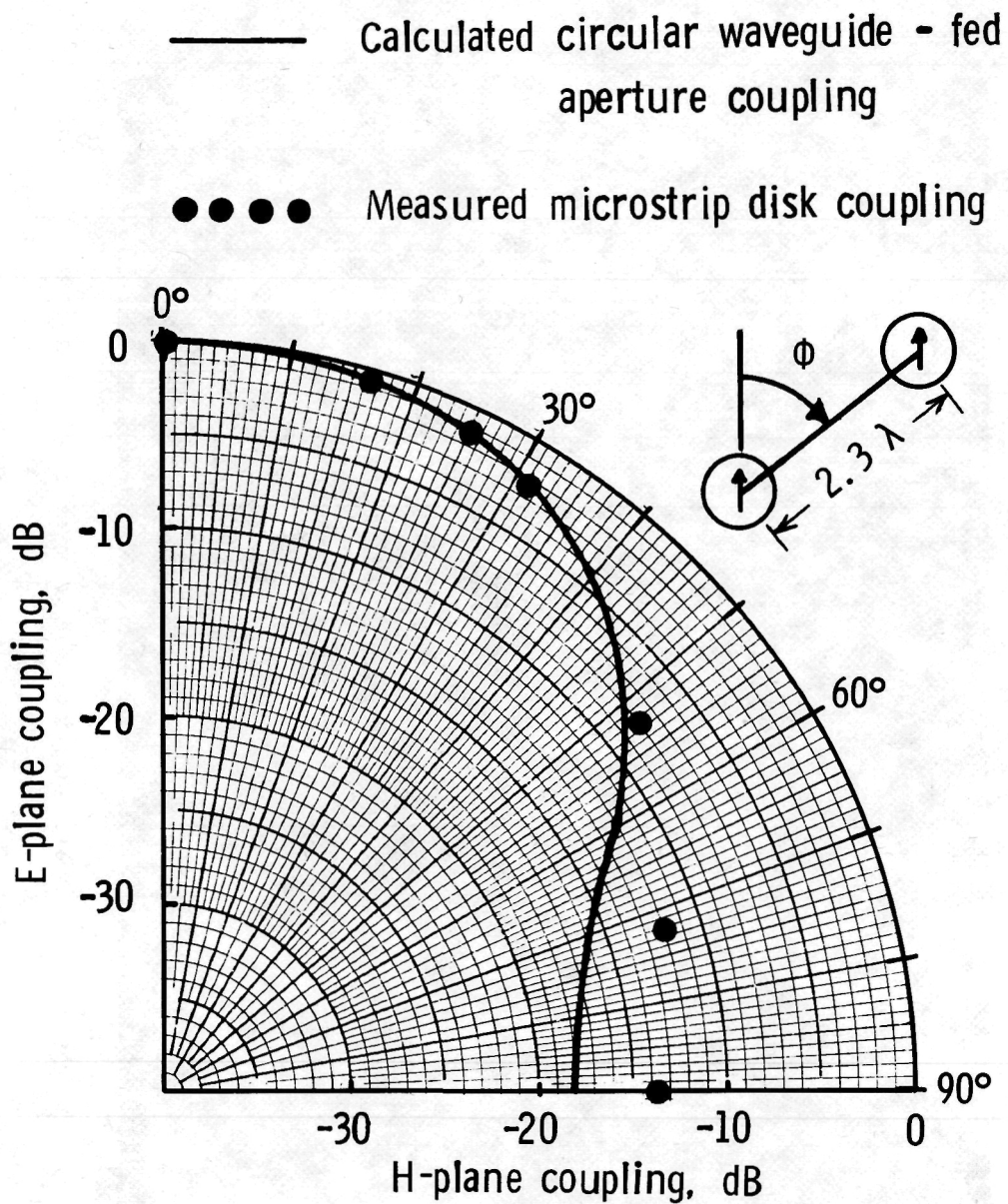


Figure 18.- Comparison of calculated and measured mutual coupling as a function of orientation.

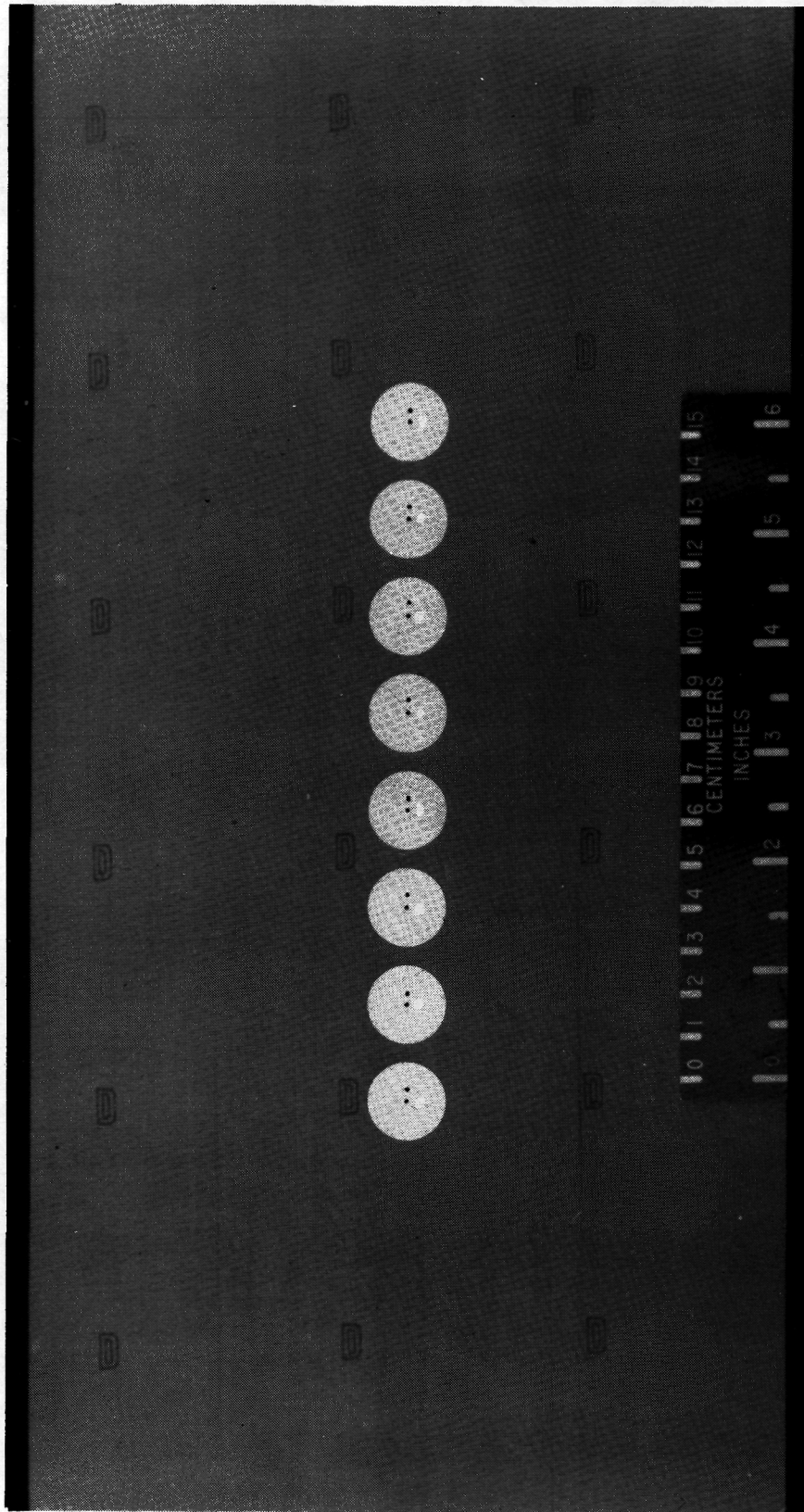


Figure 19.- The 8-element linear microstrip disk array.

L-77-2821

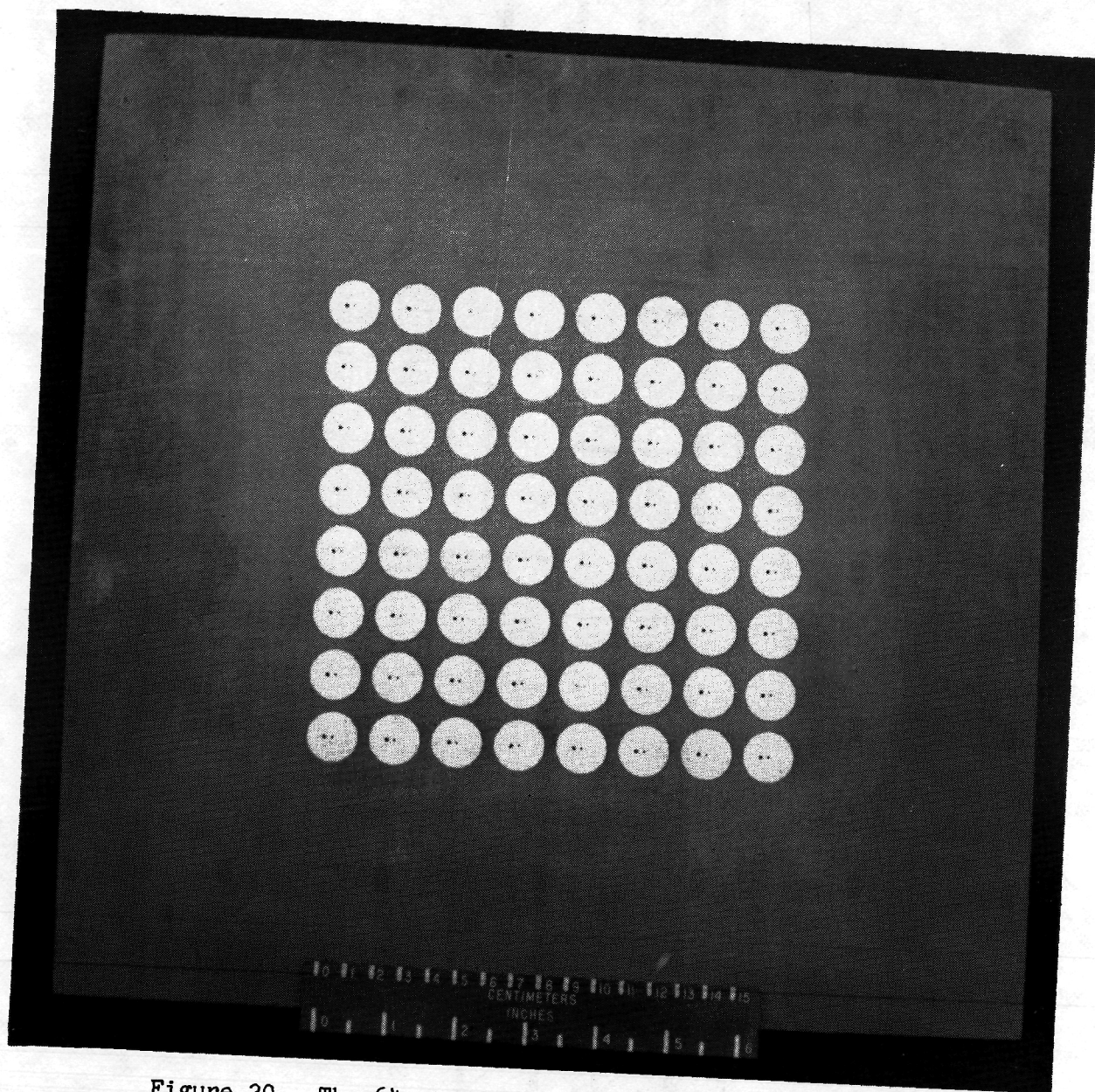


Figure 20.- The 64-element planar microstrip disk array. L-76-6610

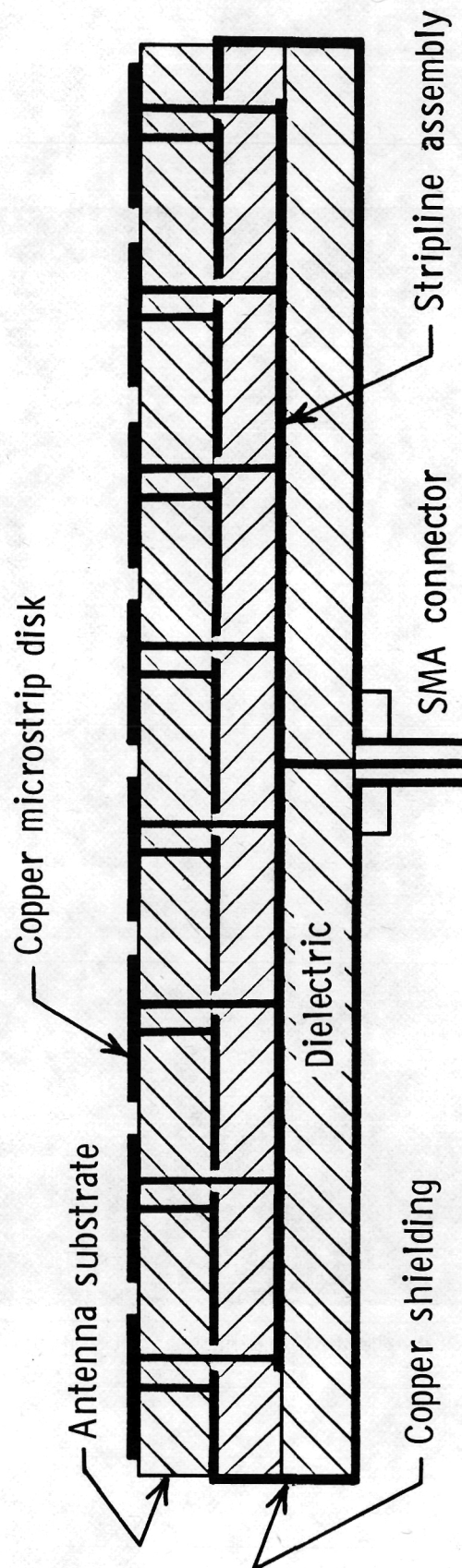


Figure 21.- Cross section of the microstrip disk antenna array and stripline feed network.

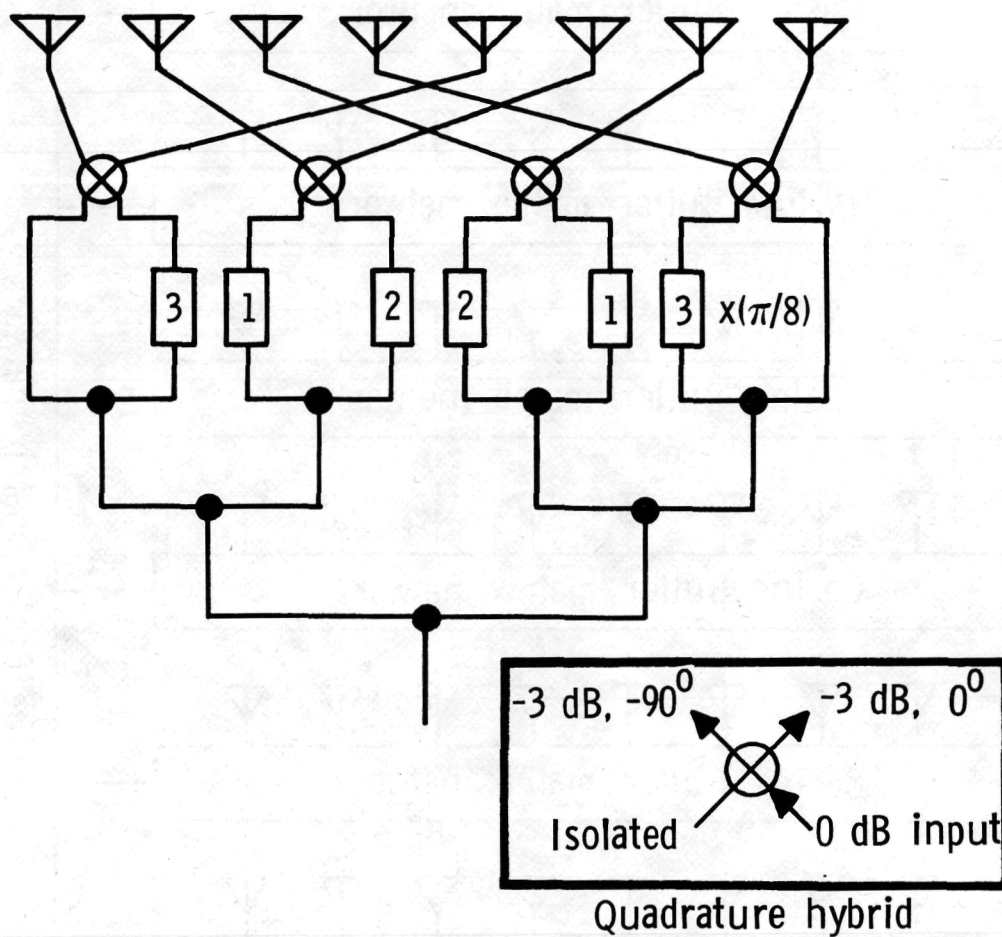


Figure 22.- Butler matrix feed network with a cosine amplitude taper.

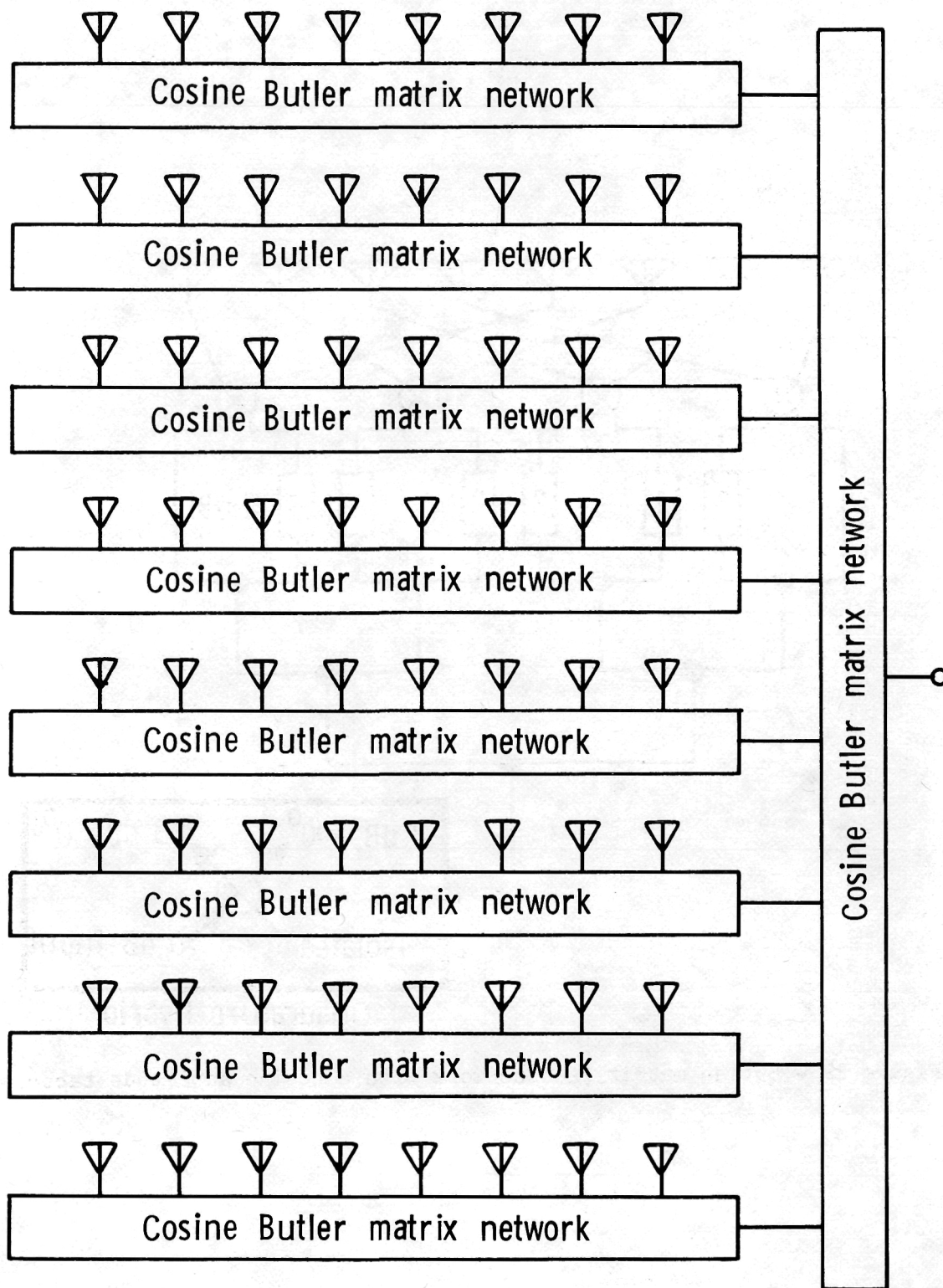
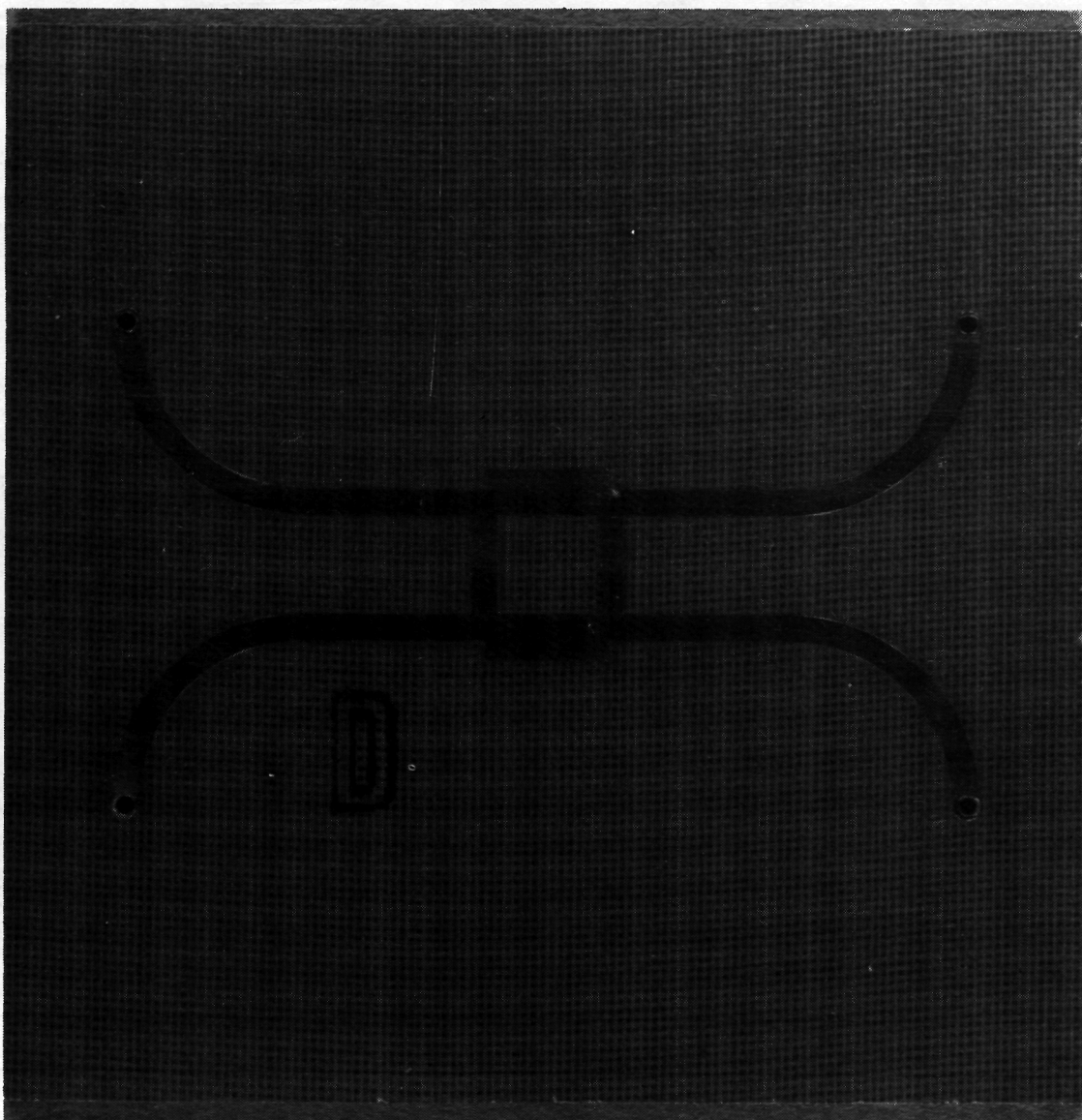


Figure 23.- The 64-element planar array Butler matrix feed network.



L-77-390

Figure 24.- Center copper conductor of a stripline 3-dB 90° branchline hybrid coupler.

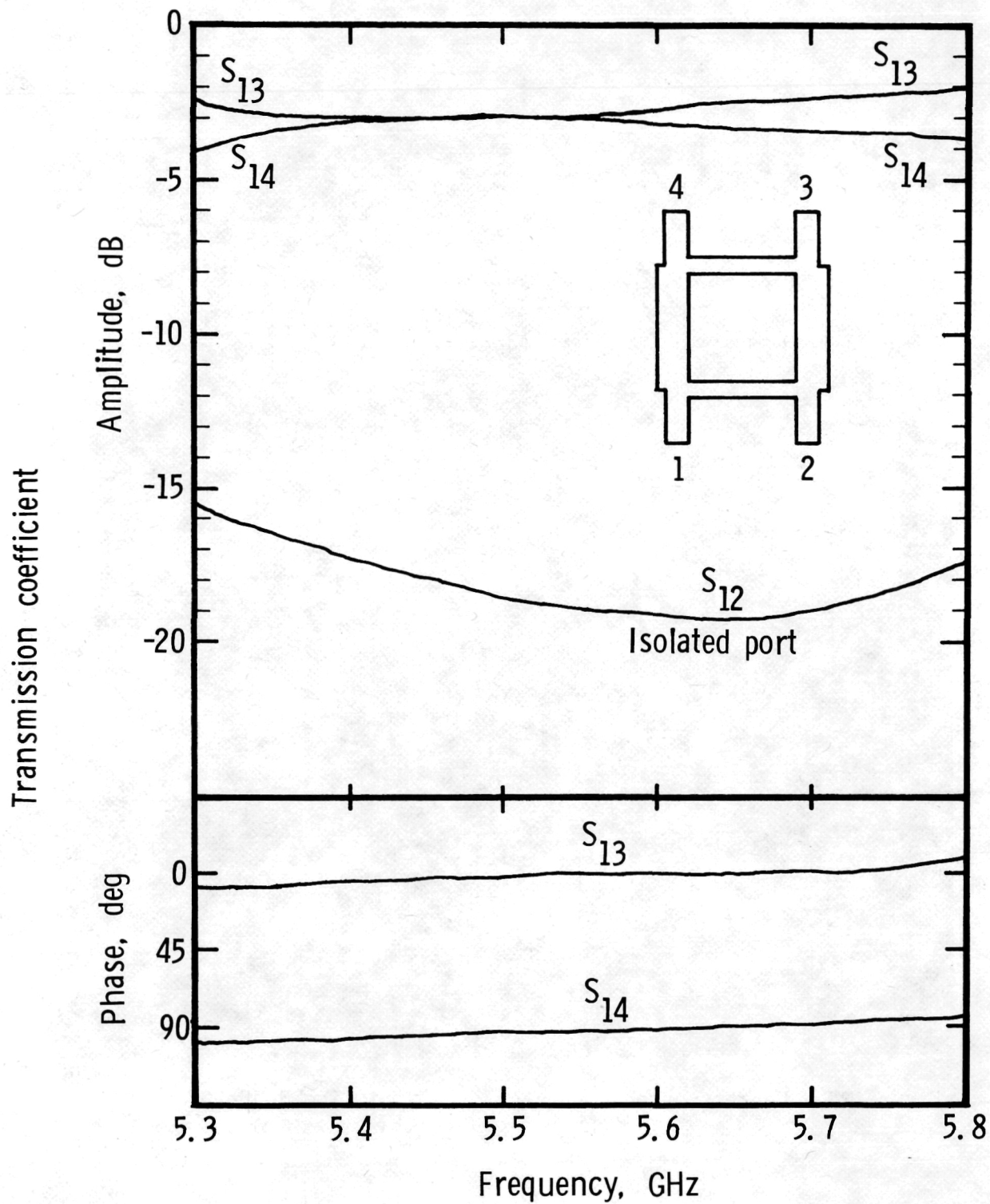


Figure 25.- Transmission parameters of branchline hybrid.

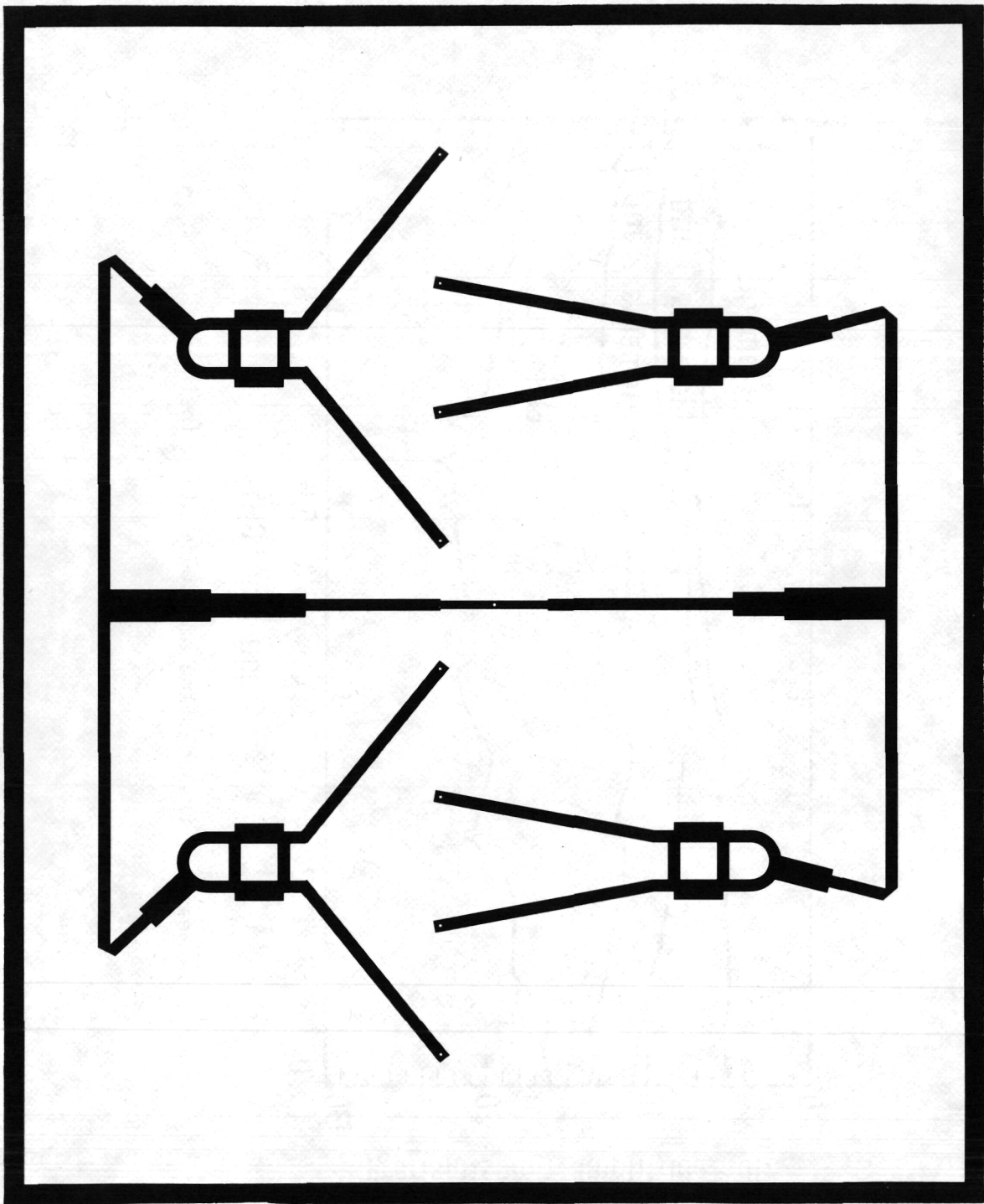


Figure 26.- Center copper conductor of stripline Butler matrix.

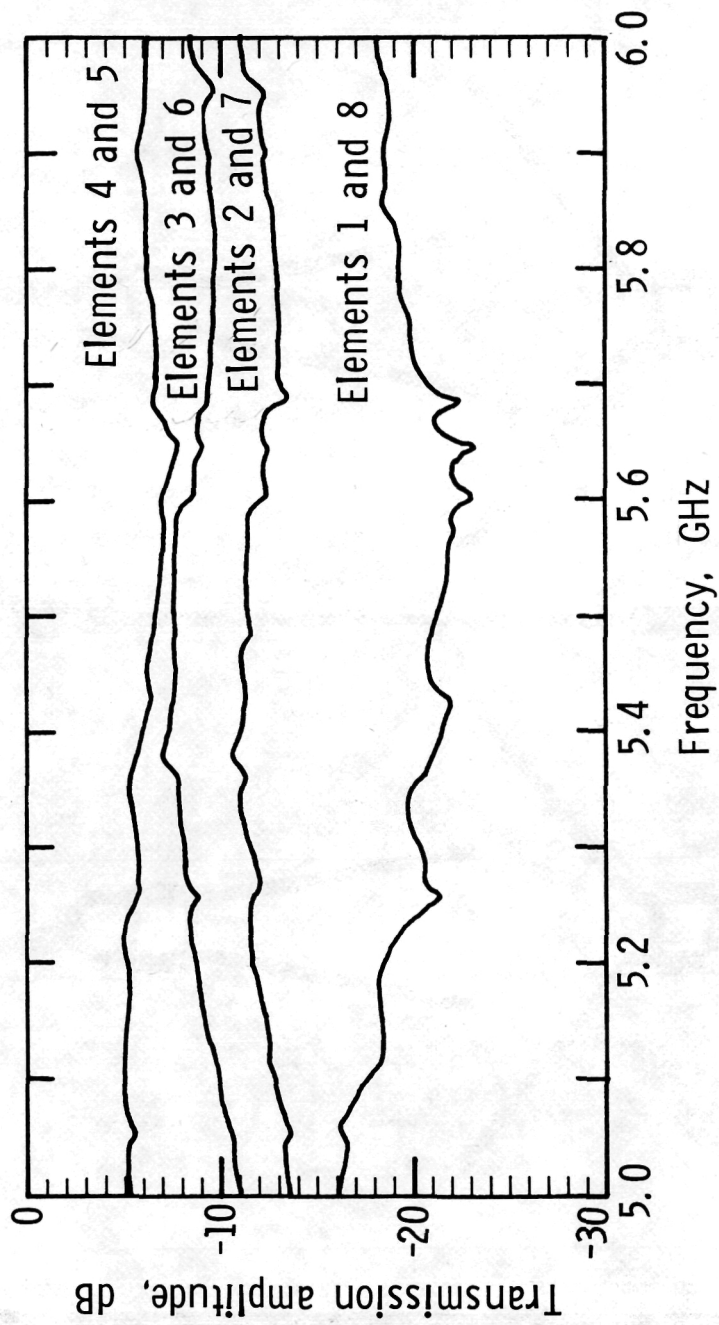


Figure 27.- Measured transmission amplitude of stripline Butler matrix.

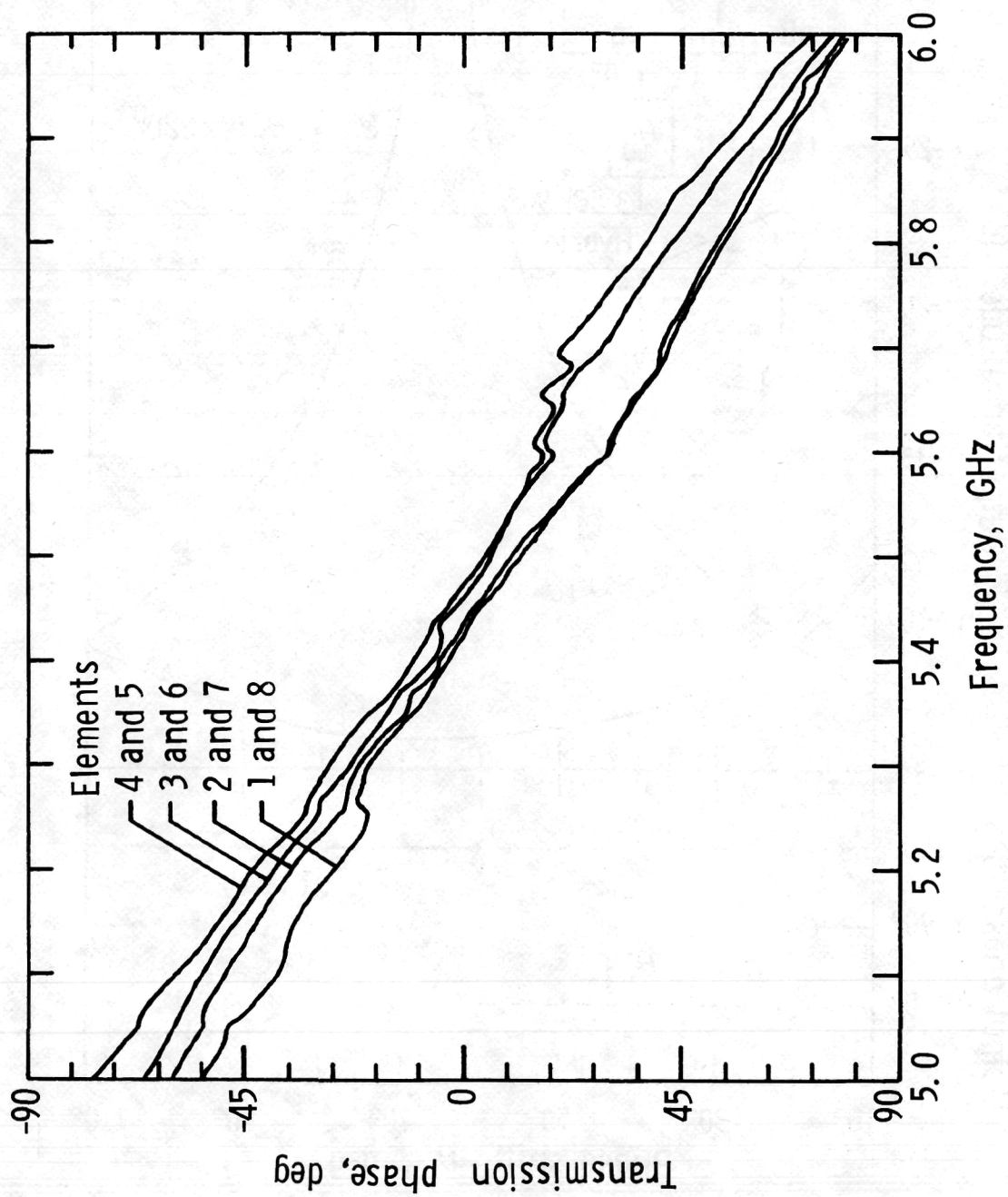


Figure 28.- Measured transmission phase of stripline Butler matrix.

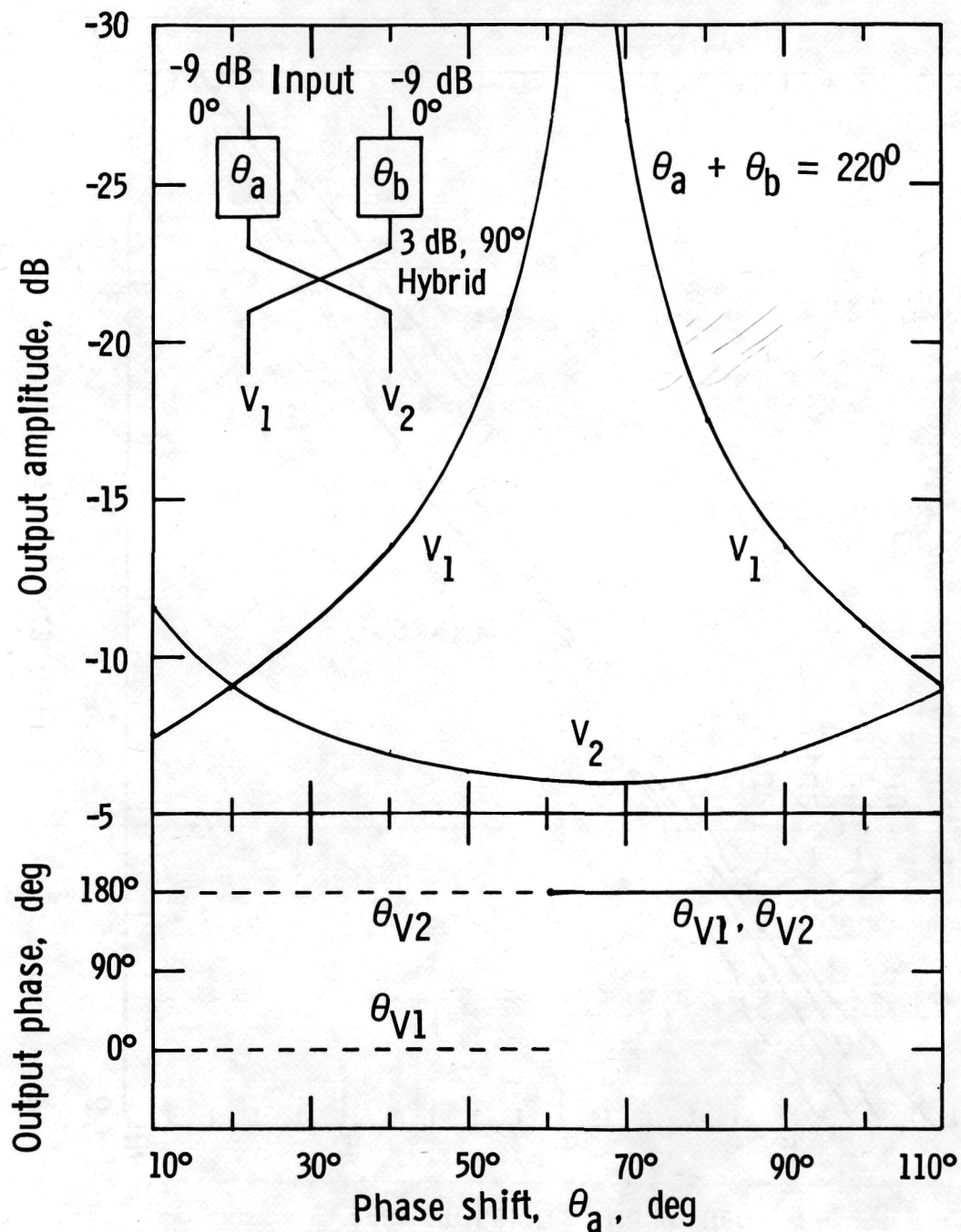
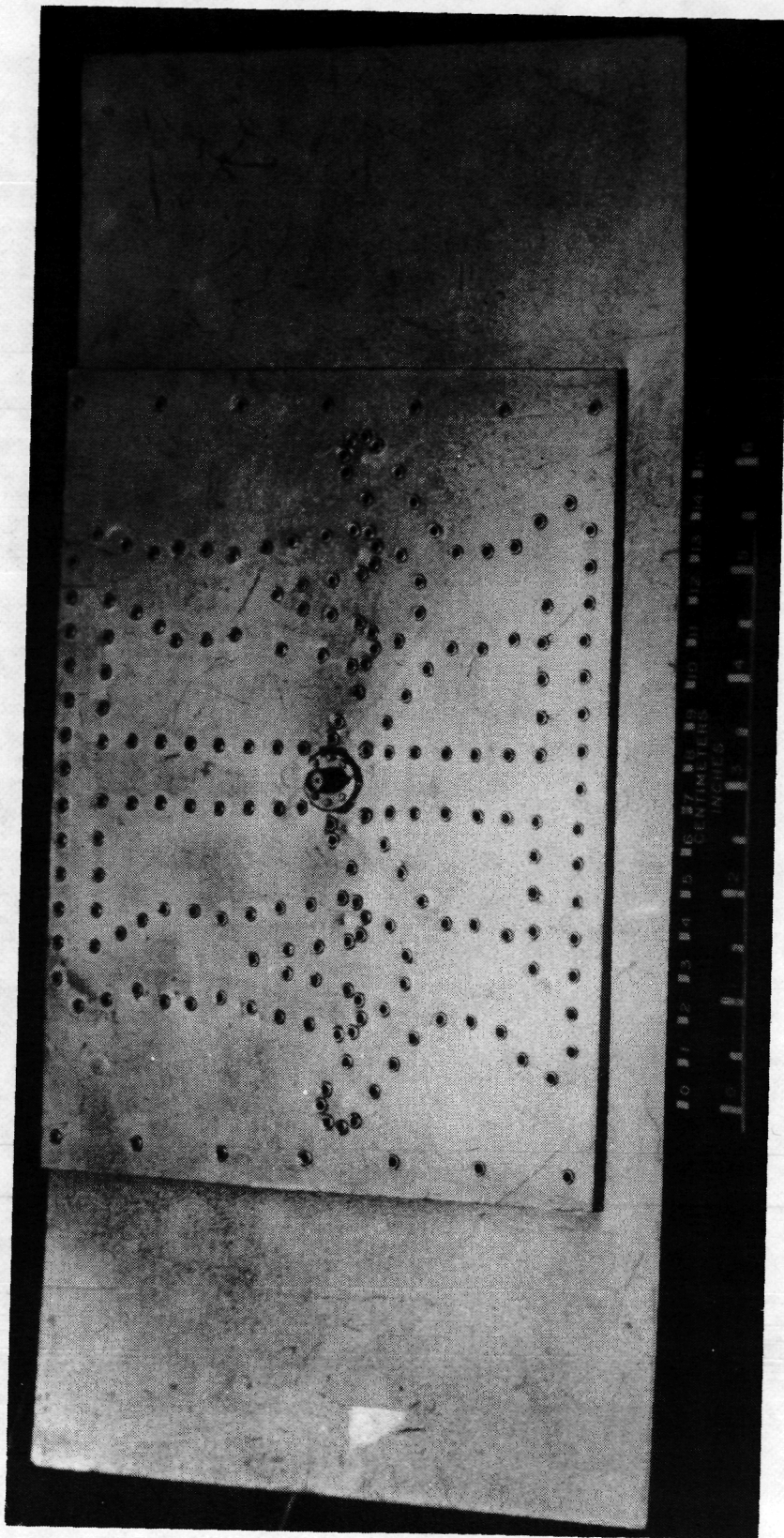
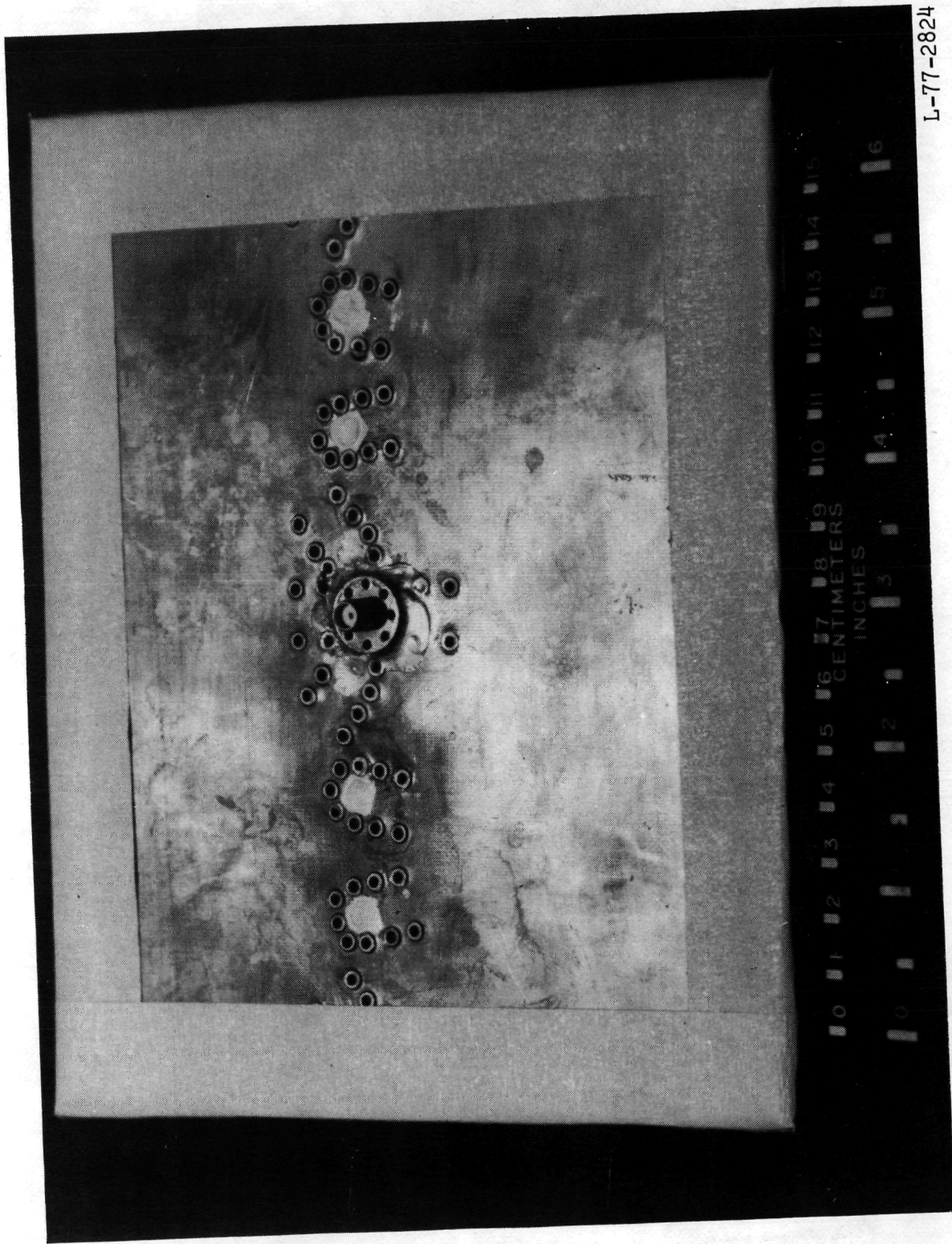


Figure 29.- Calculated outputs of hybrid and phase shifter combination.



L-77-2823

Figure 30.- Stripline network bonded to back of 8-element microstrip array.



L-77-2824

Figure 31.- Improved 8-element stripline feed network package.

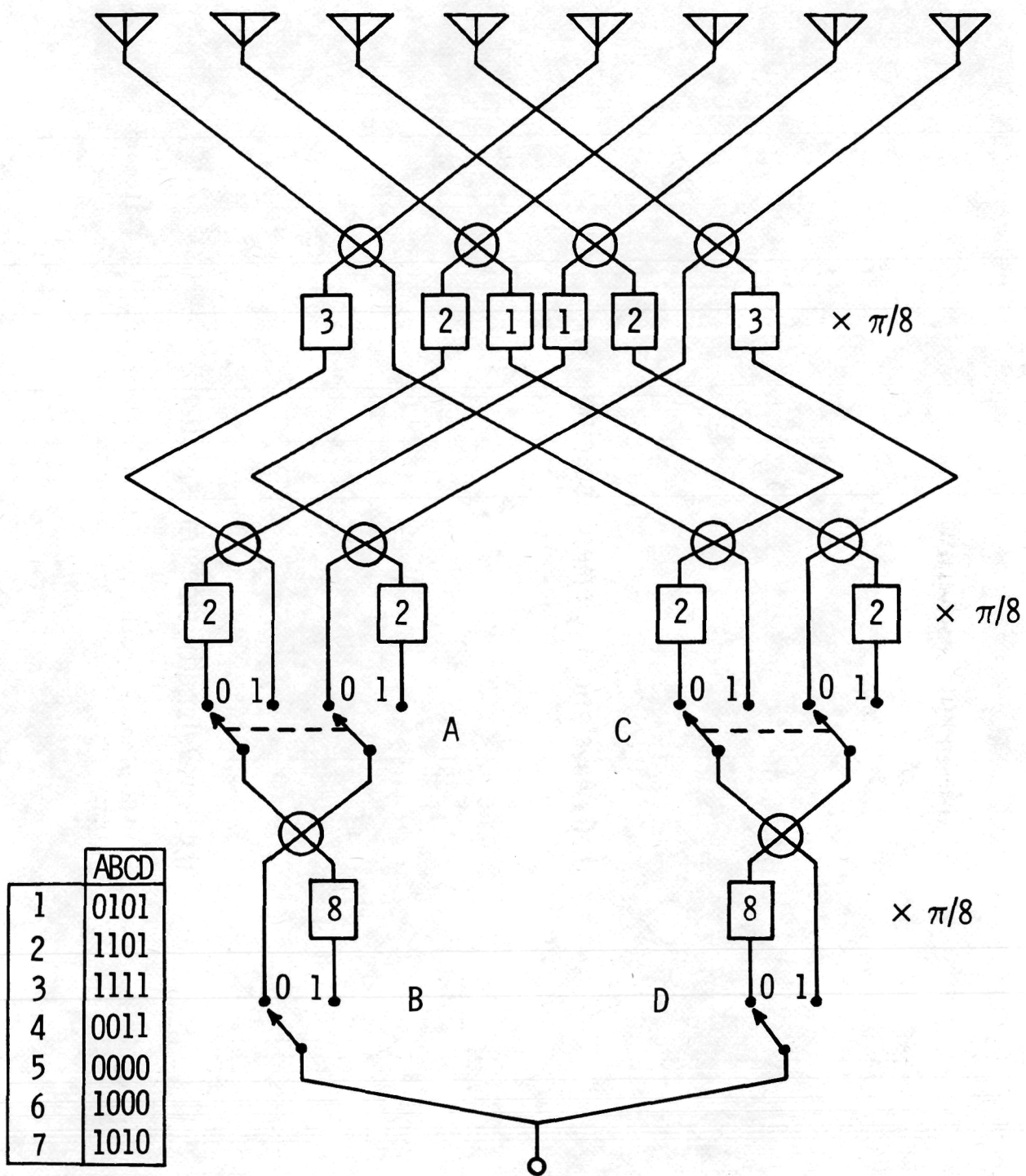
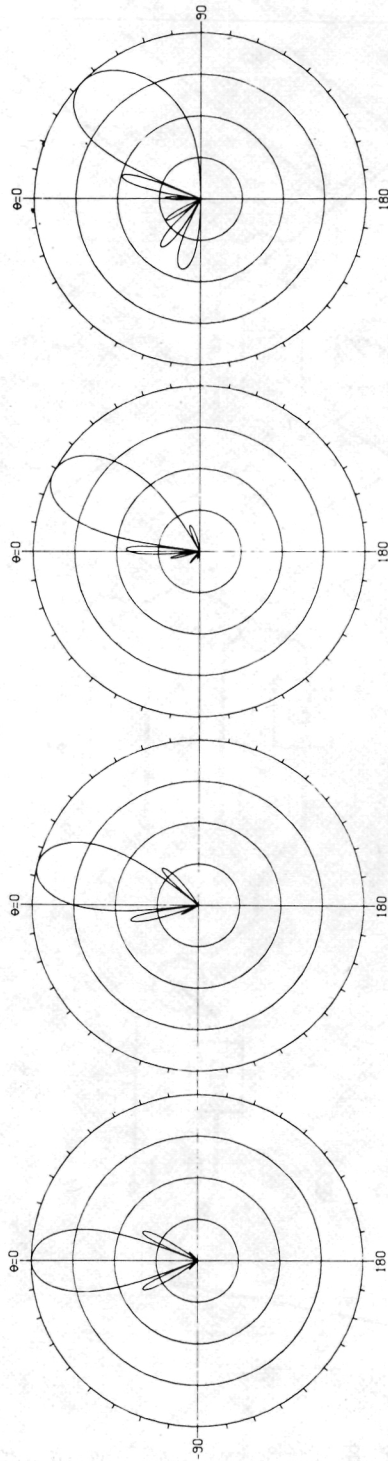
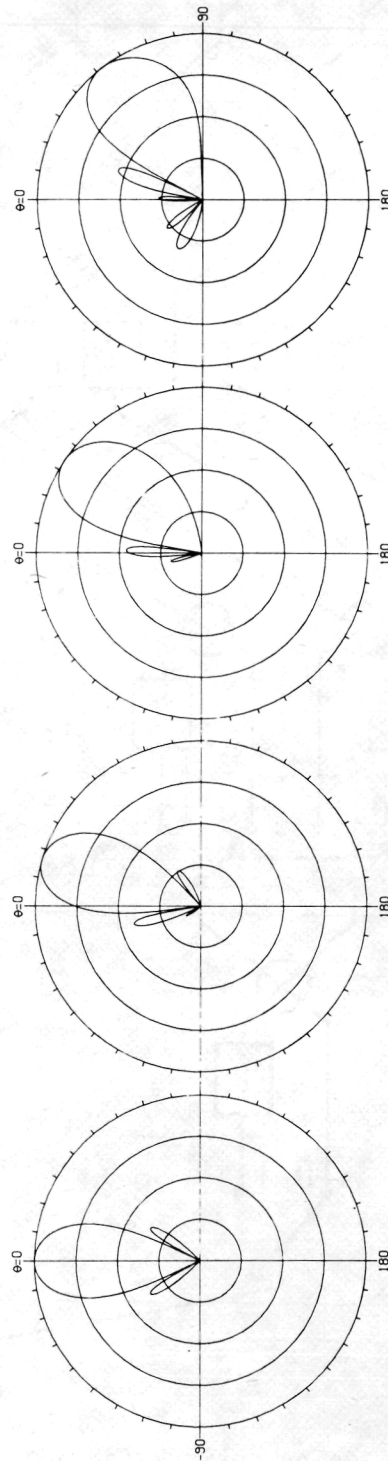


Figure 32.- Switching network for addition of 8 uniformly illuminated beams to form 7 cosine illuminated beams.



0.50 wavelength element spacing



0.42 wavelength element spacing

Figure 33.- Calculated H-plane scanning radiation patterns for a 64-element planar array with cosine illumination.

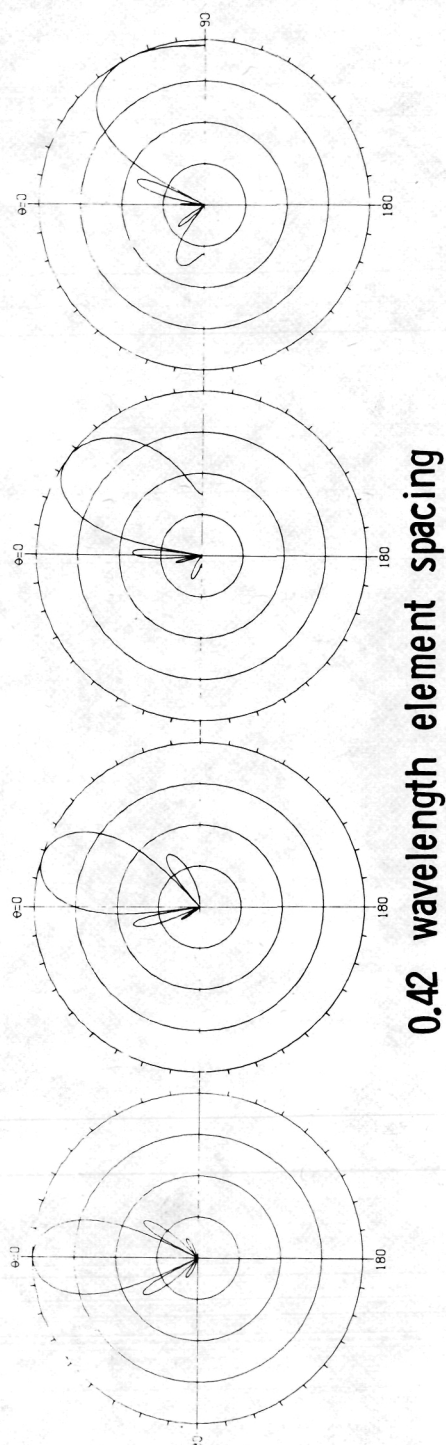
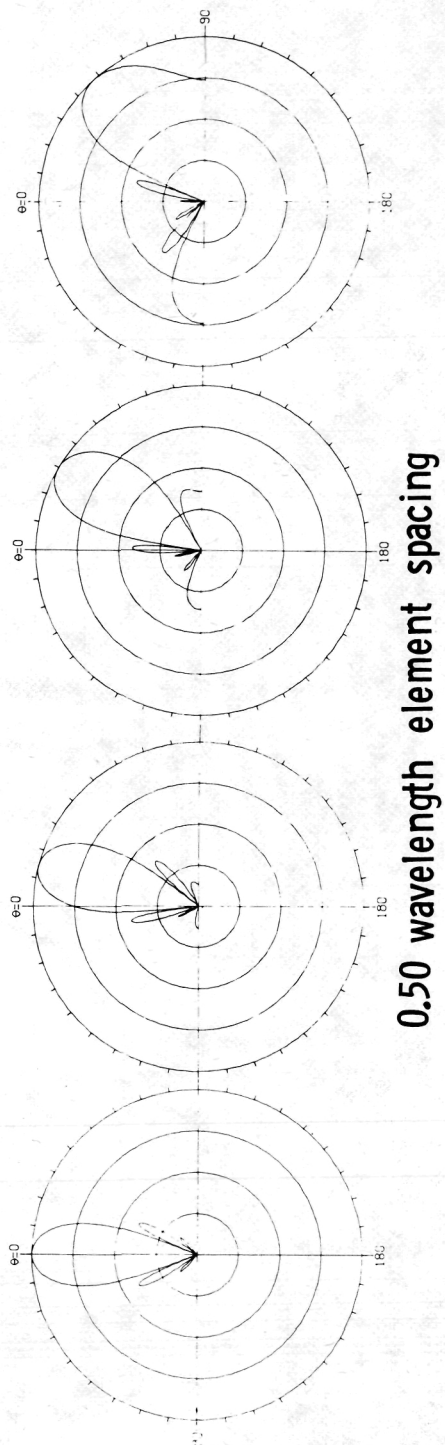
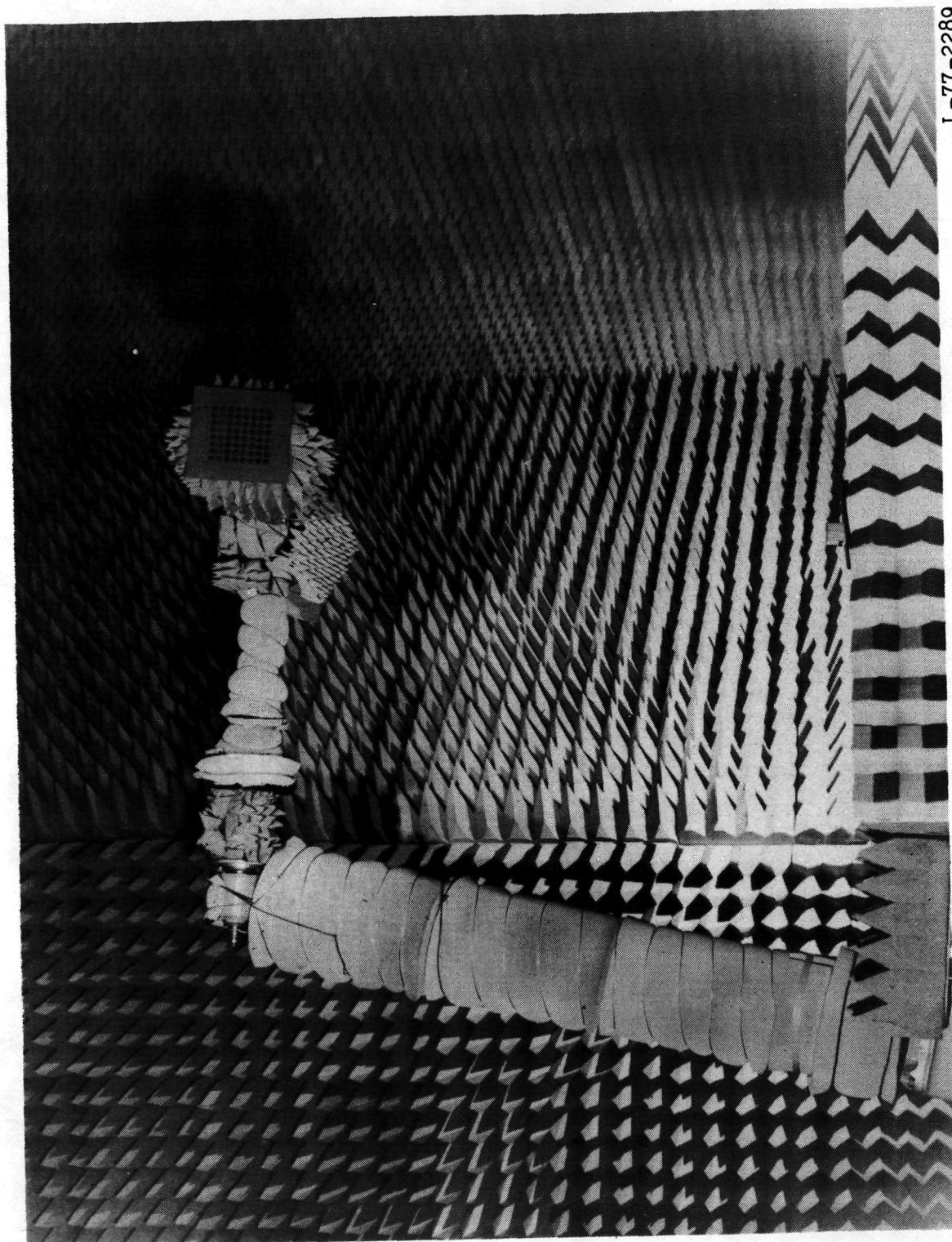


Figure 34.- Calculated E-plane scanning radiation patterns for a 64-element planar array with cosine illumination.



L-77-2289

Figure 35.- The 64-element array mounted in anechoic test chamber.



L-77-2291

Figure 36.- Anechoic chamber operating console.

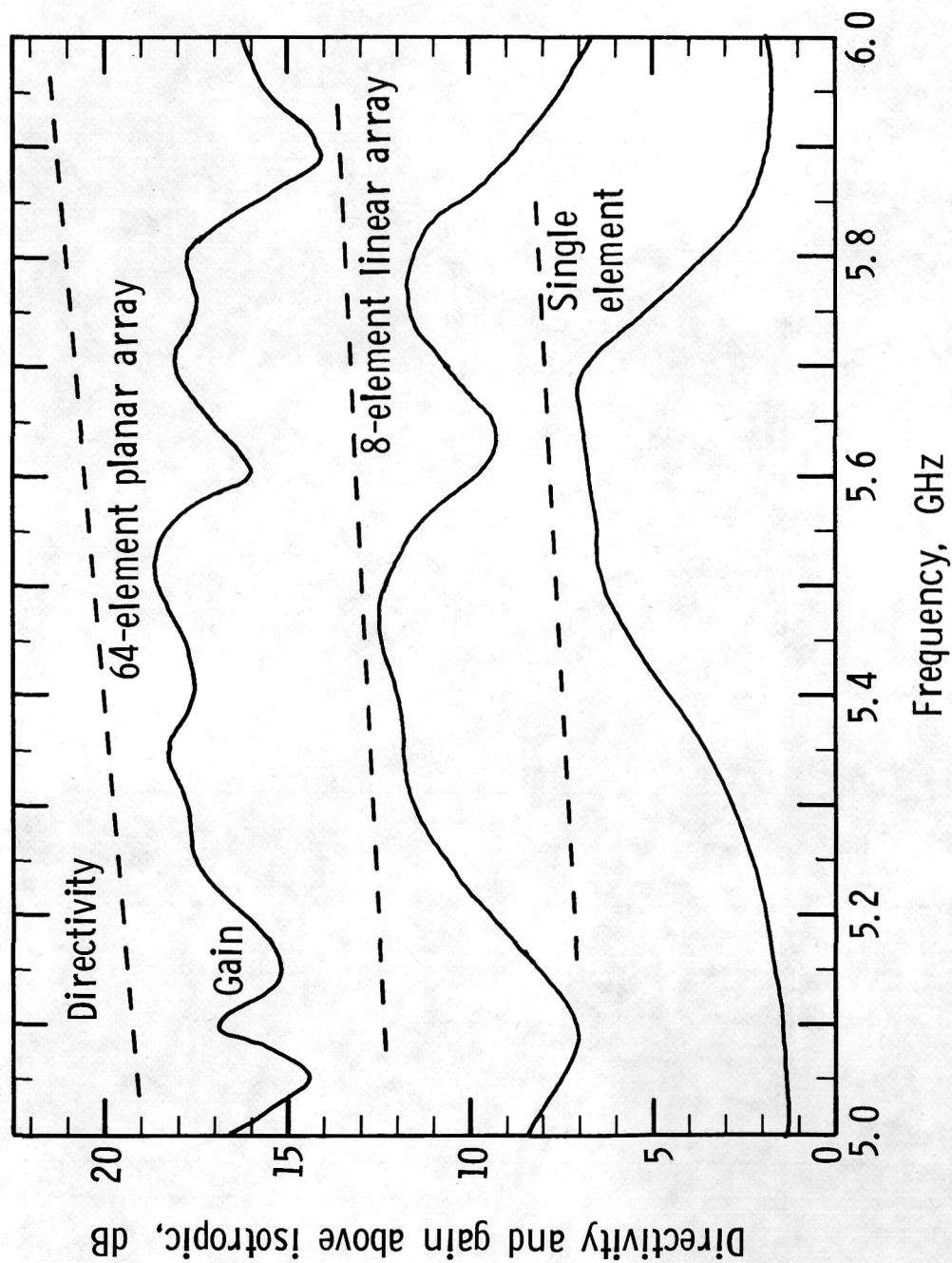
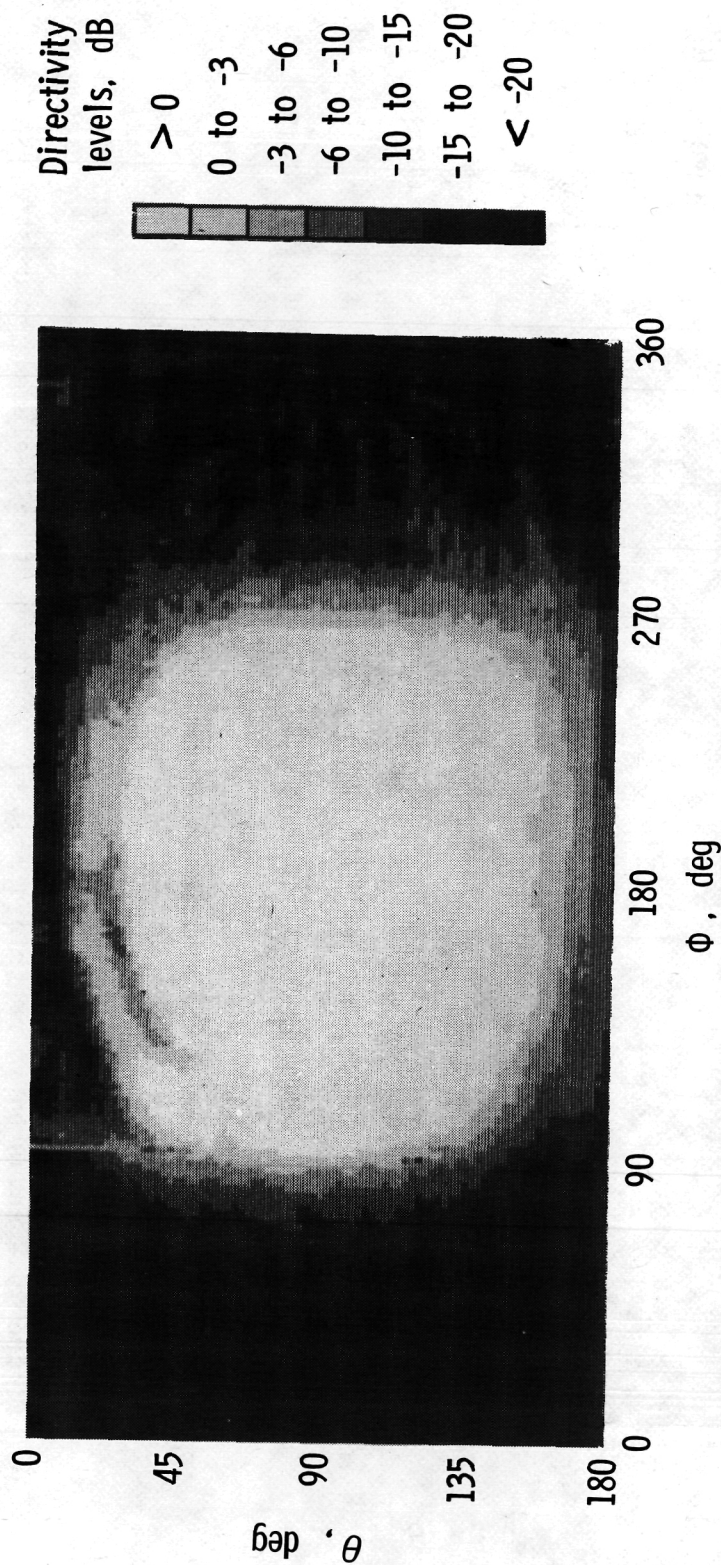
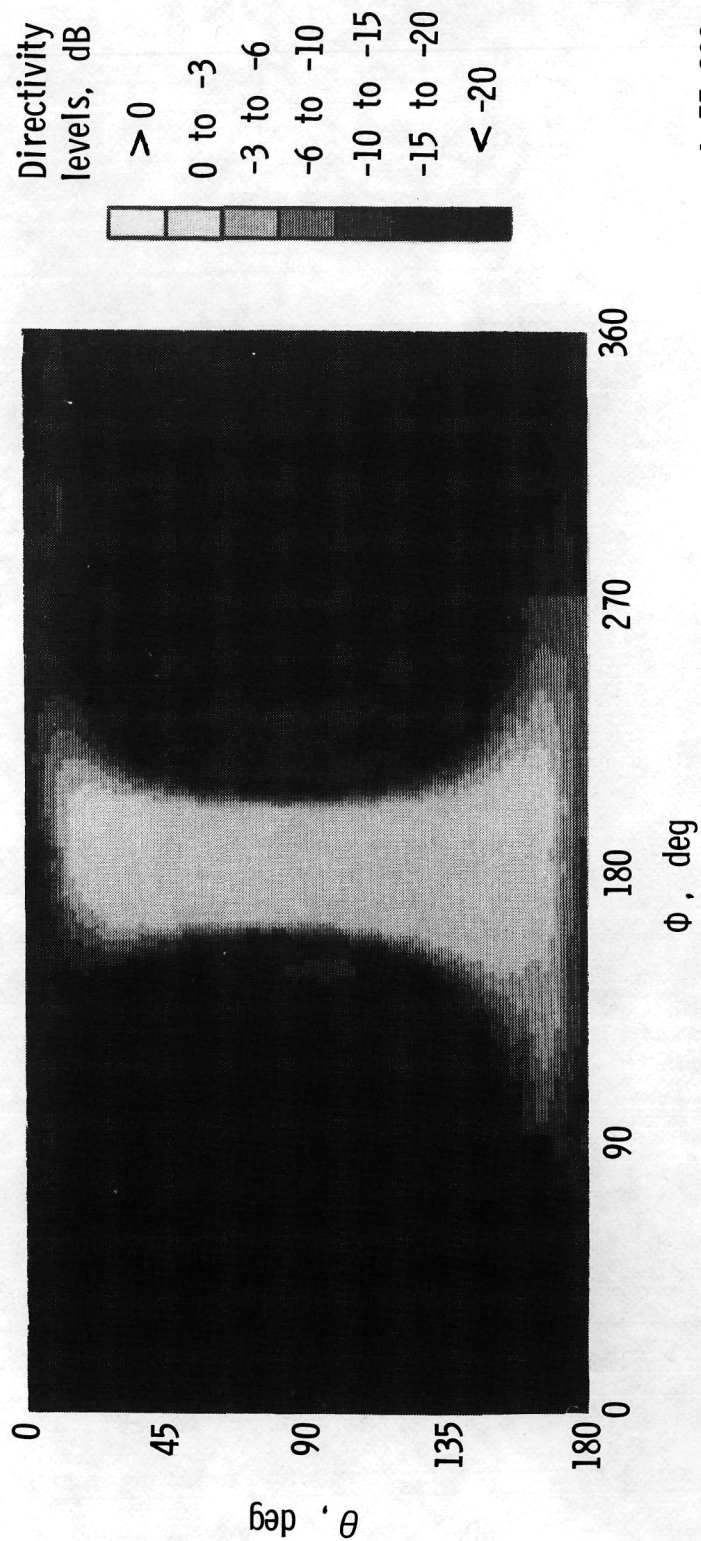


Figure 37.- Gain and directivity as a function of frequency for single element, 8-element linear array, and the 64-element planar array.



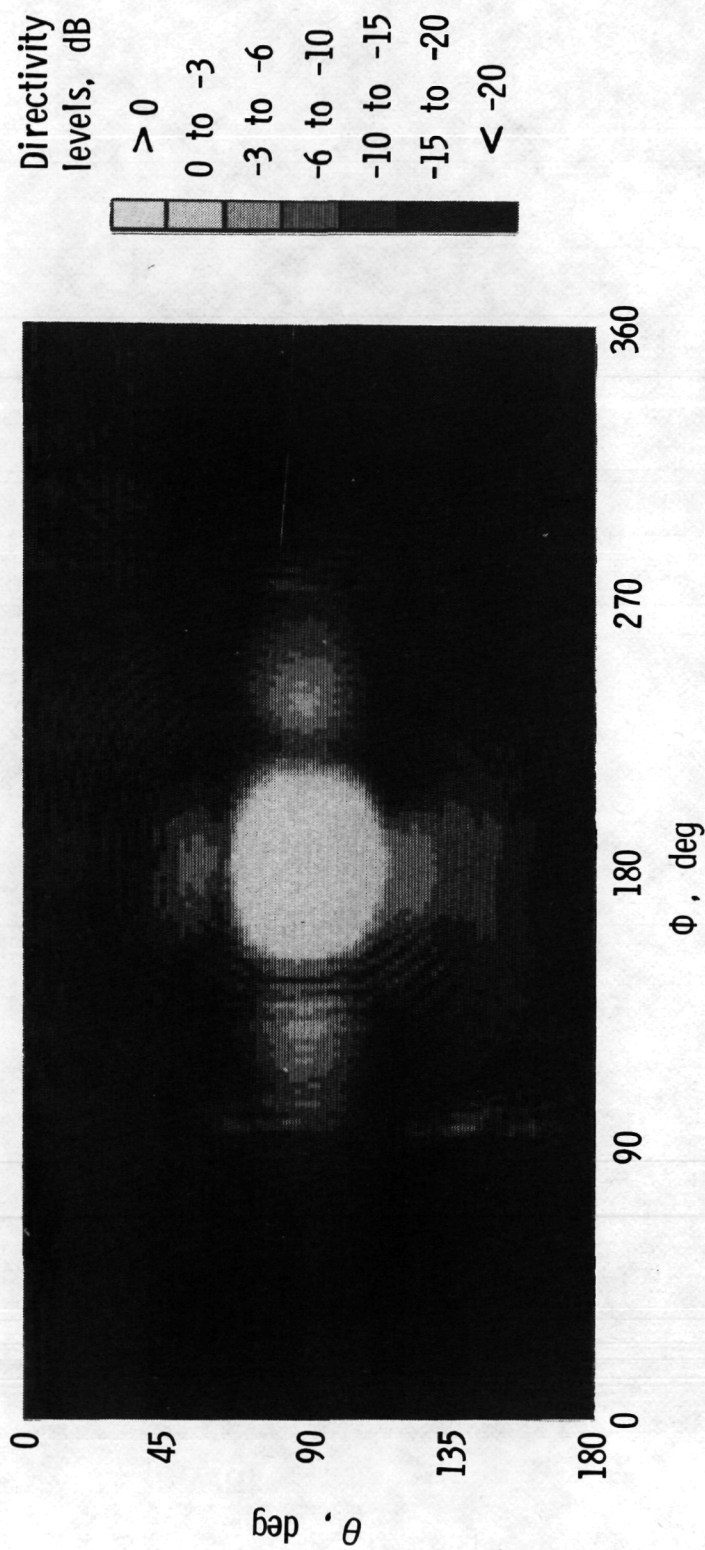
L-77-391

Figure 38.- Measured volumetric directivity pattern of a microstrip disk relative to an isotropic radiator.



L-77-392

Figure 39.- Measured volumetric directivity pattern of an 8-element microstrip disk linear array relative to an isotropic radiator.



L-77-393

Figure 40.- Measured volumetric directivity pattern of a 64-element microstrip disk planar array relative to an isotropic radiator.

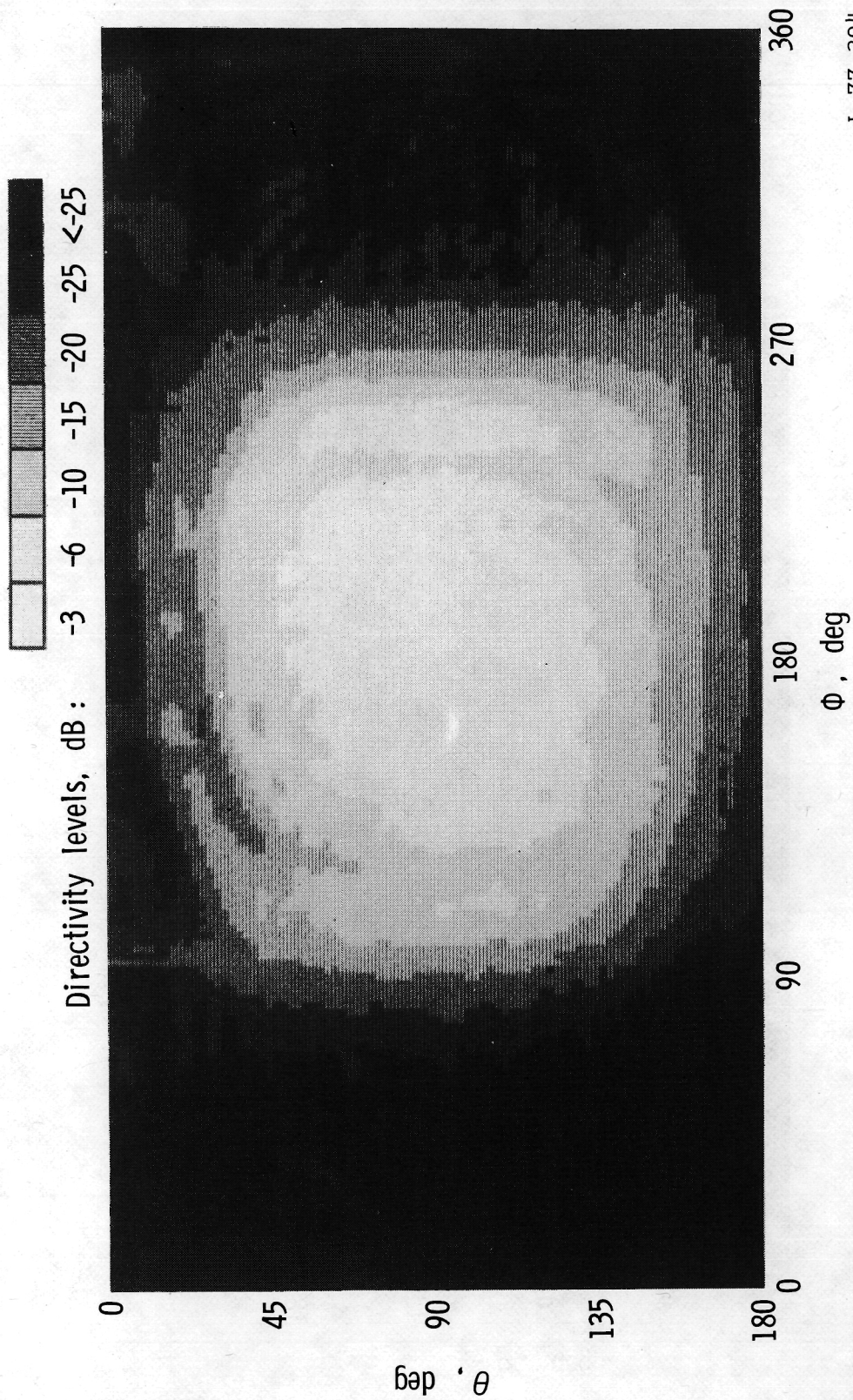


Figure 41.- Measured volumetric radiation pattern of a microstrip disk
normalized to beam peak.

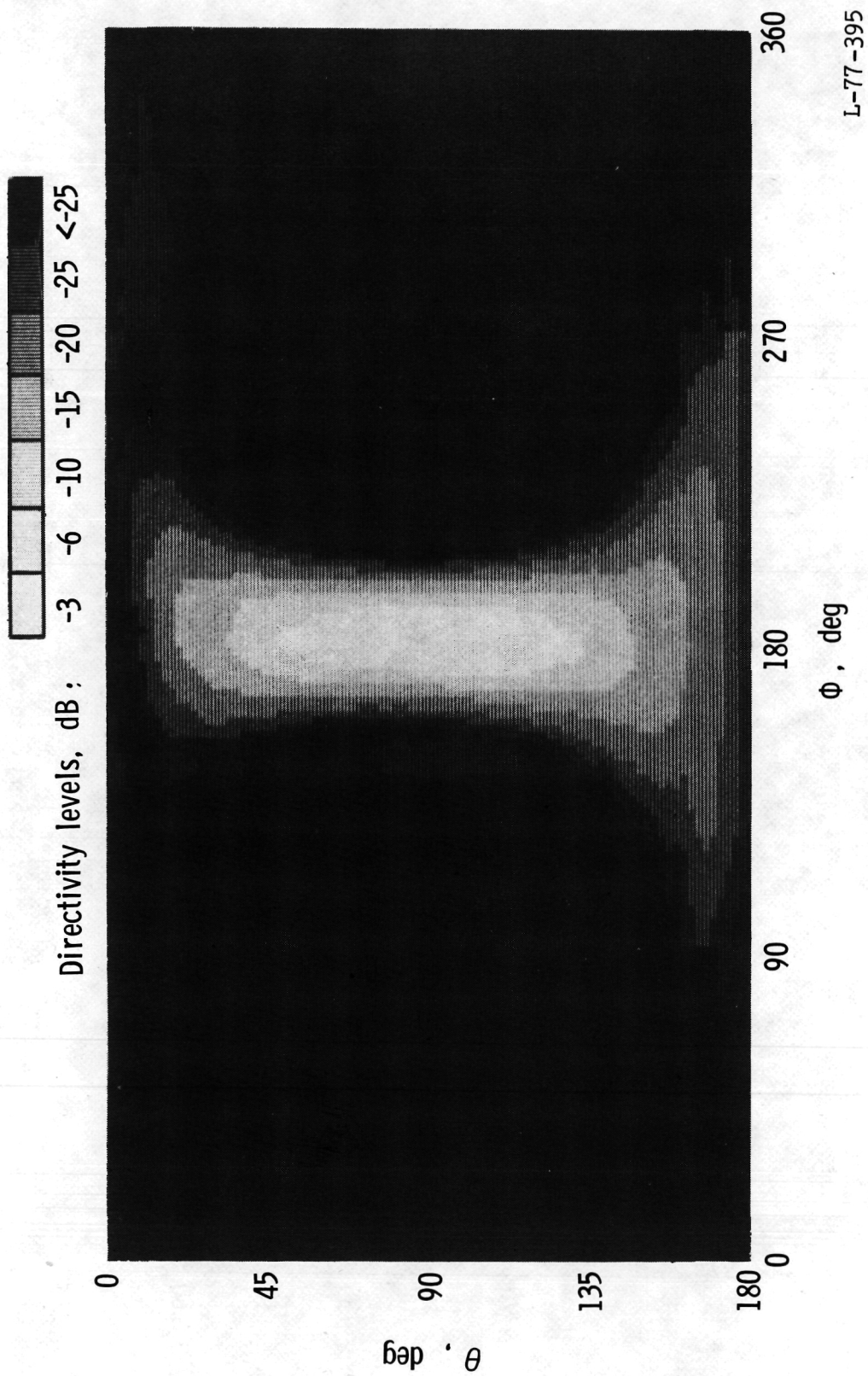


Figure 42.- Measured volumetric radiation pattern of an 8-element microstrip disk linear array normalized to beam peak.

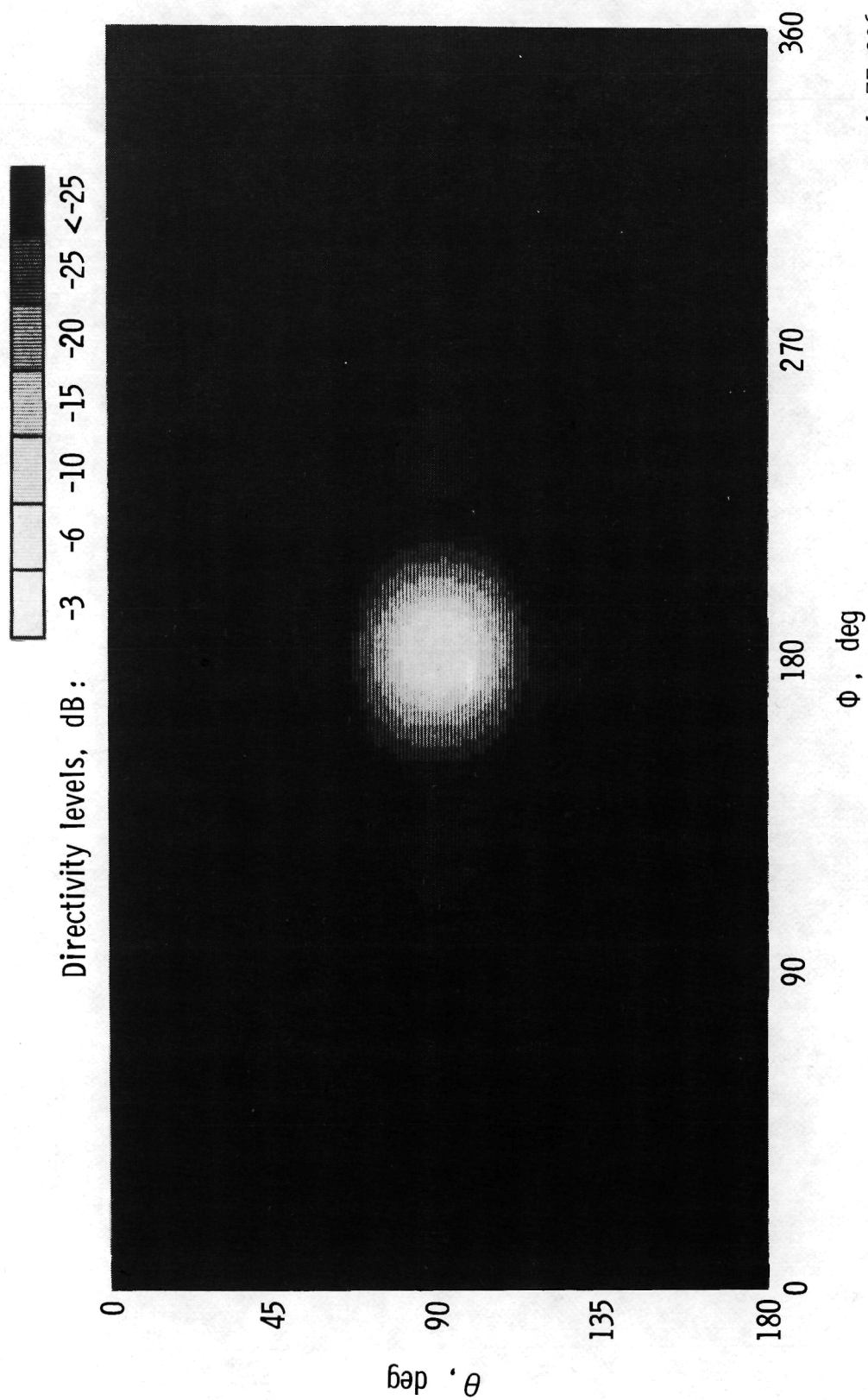


Figure 43.- Measured volumetric radiation pattern of a 64-element microstrip disk planar array normalized to beam peak.

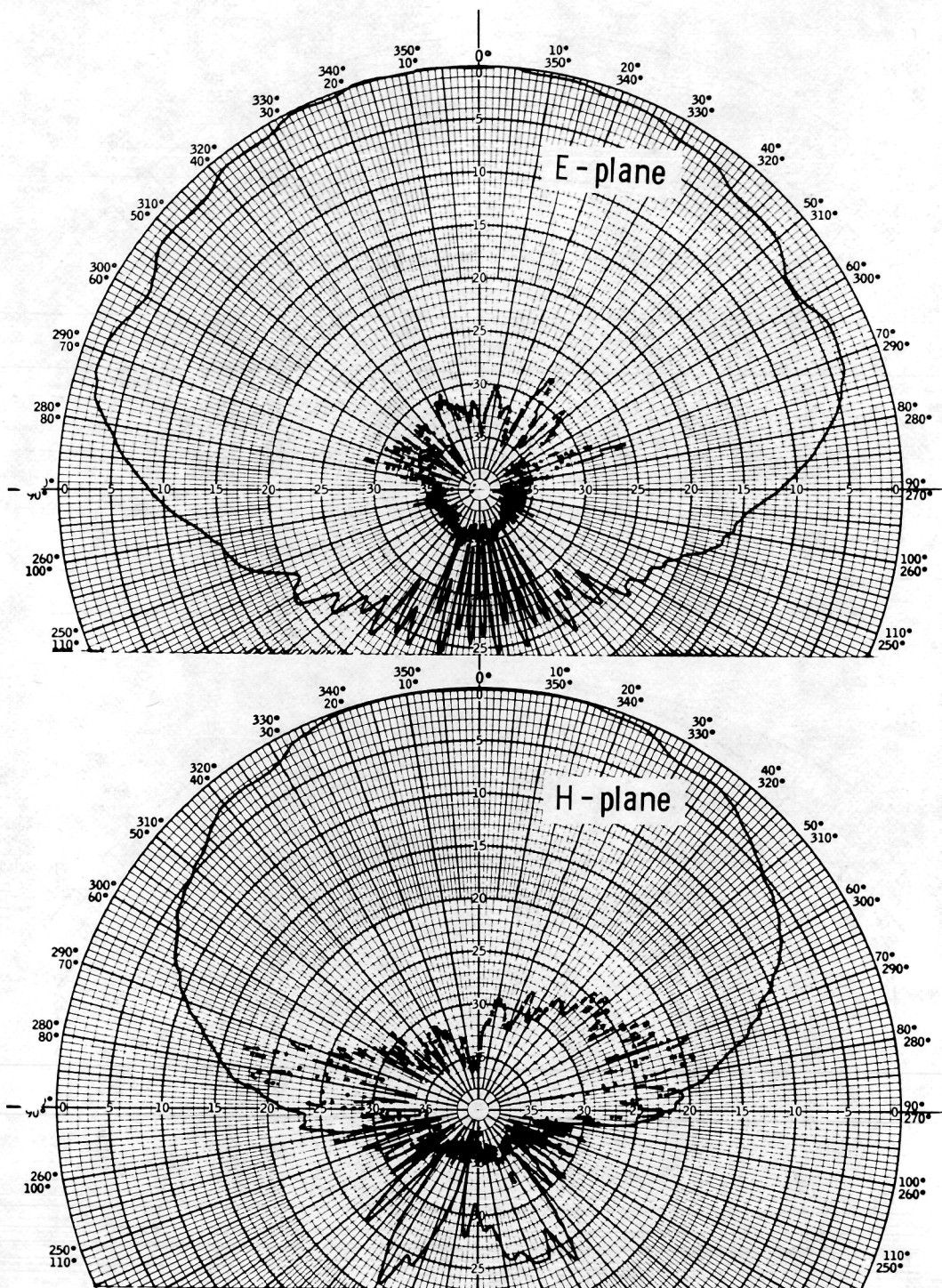


Figure 44.- Principal plane radiation patterns for a microstrip disk on a 0.6-m ground plane at 5.5 GHz.

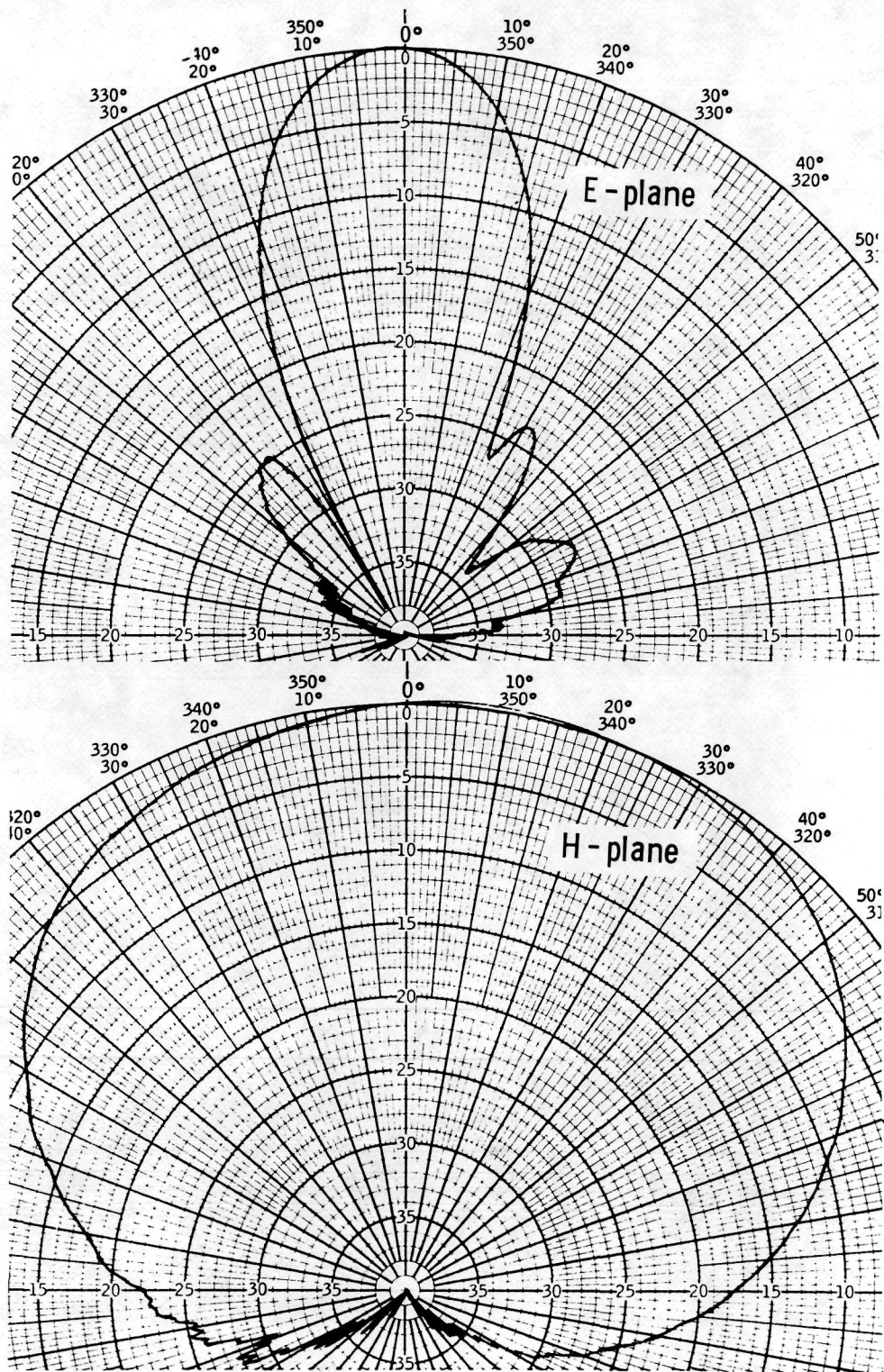


Figure 45.- Principal plane radiation patterns for an 8-element microstrip disk linear array on a 0.6-m ground plane at 5.45 GHz.

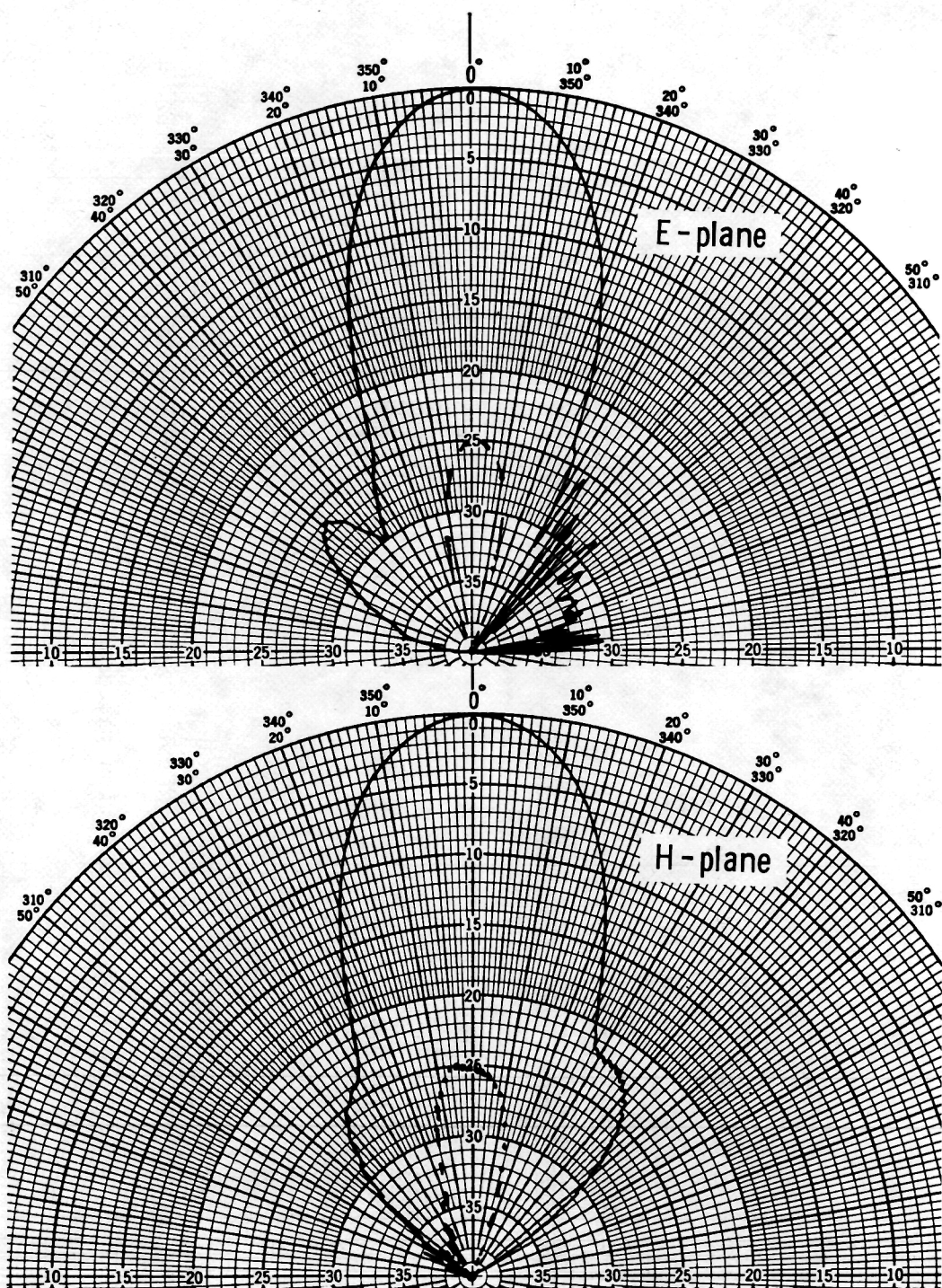


Figure 46.- Principal plane radiation patterns for a 64-element microstrip disk planar array on a 0.3-m ground plane at 5.35 GHz.

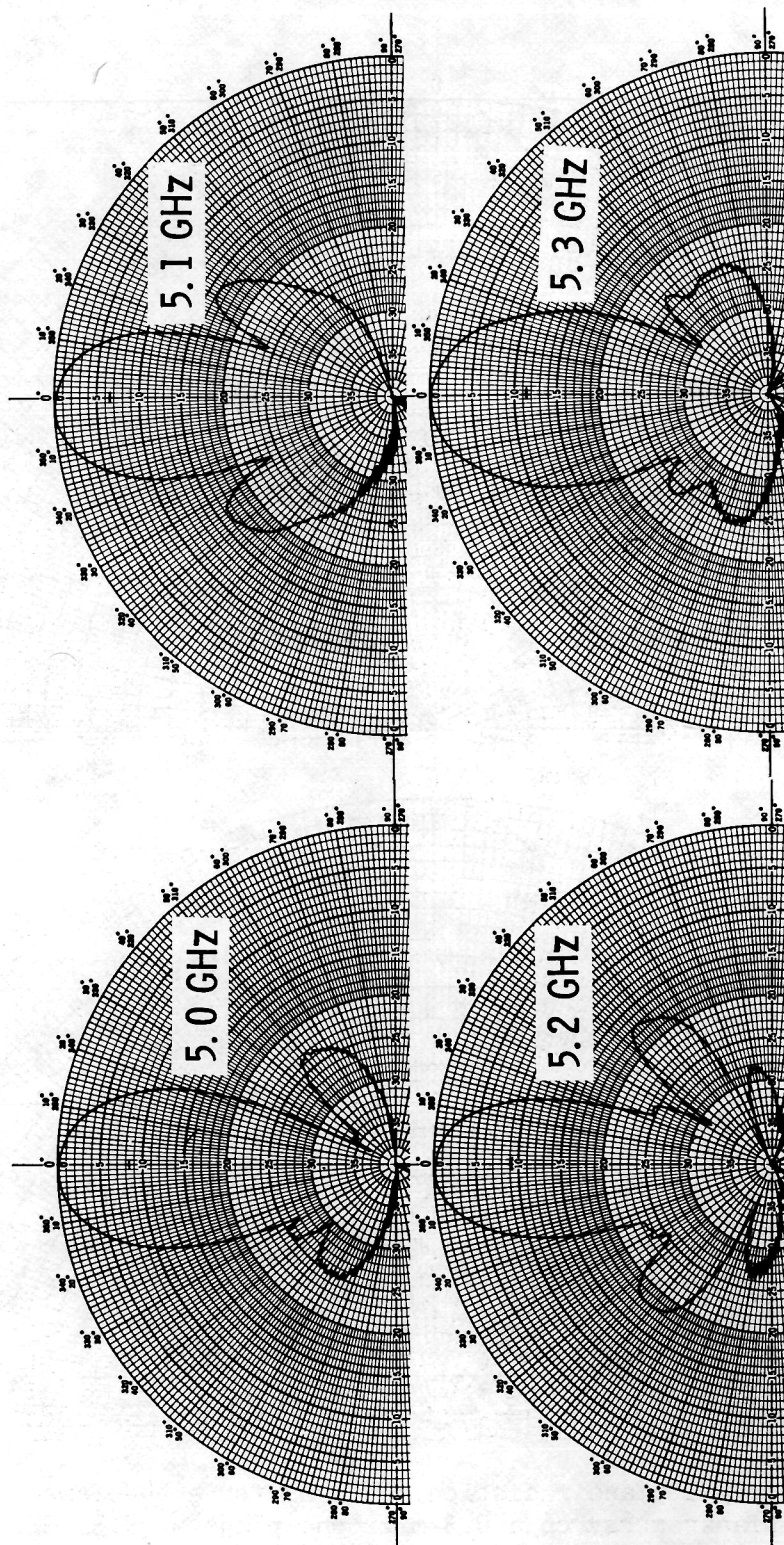


Figure 47.- E-plane radiation patterns for 8-element linear array.

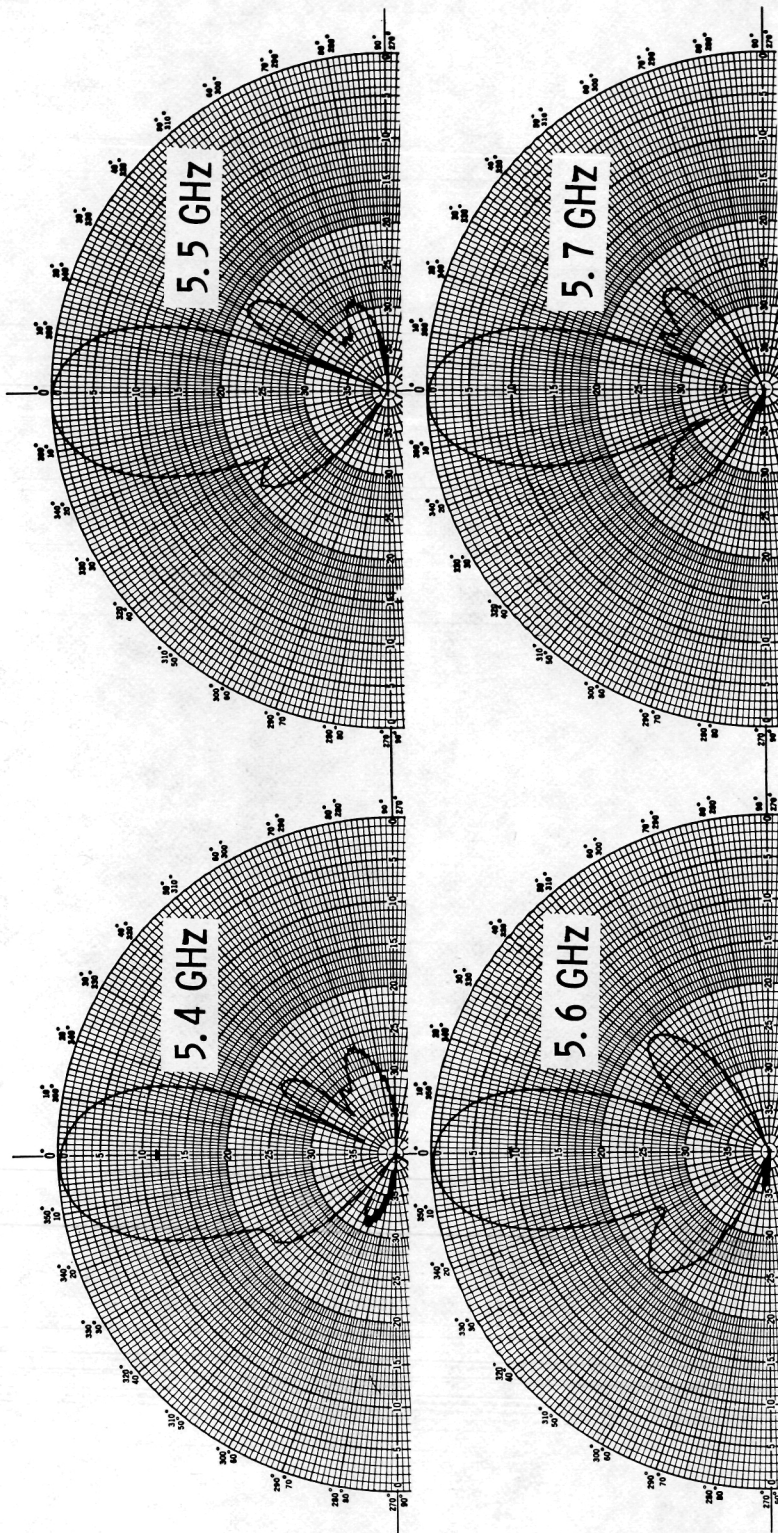


Figure 47.- Continued.

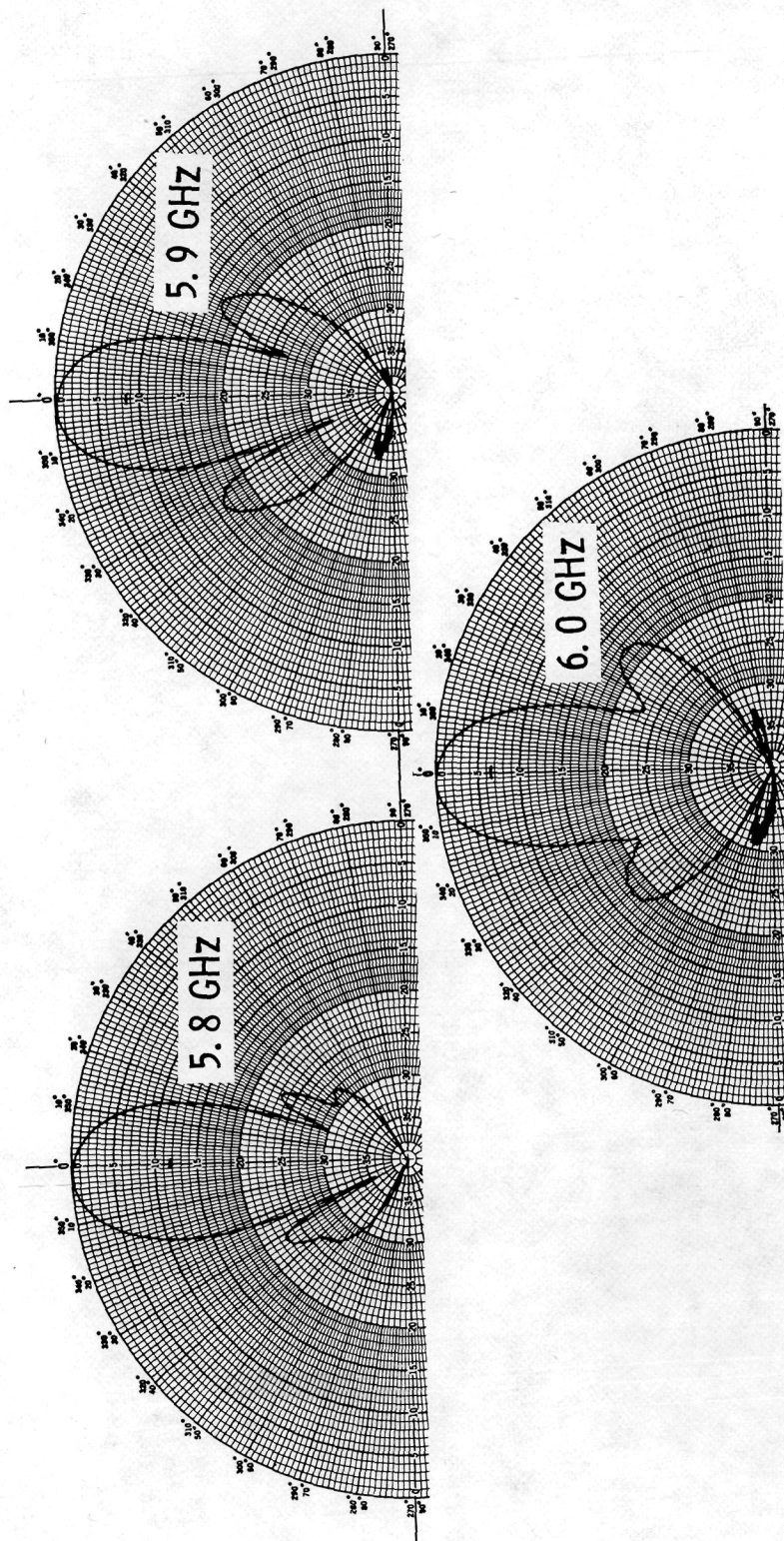
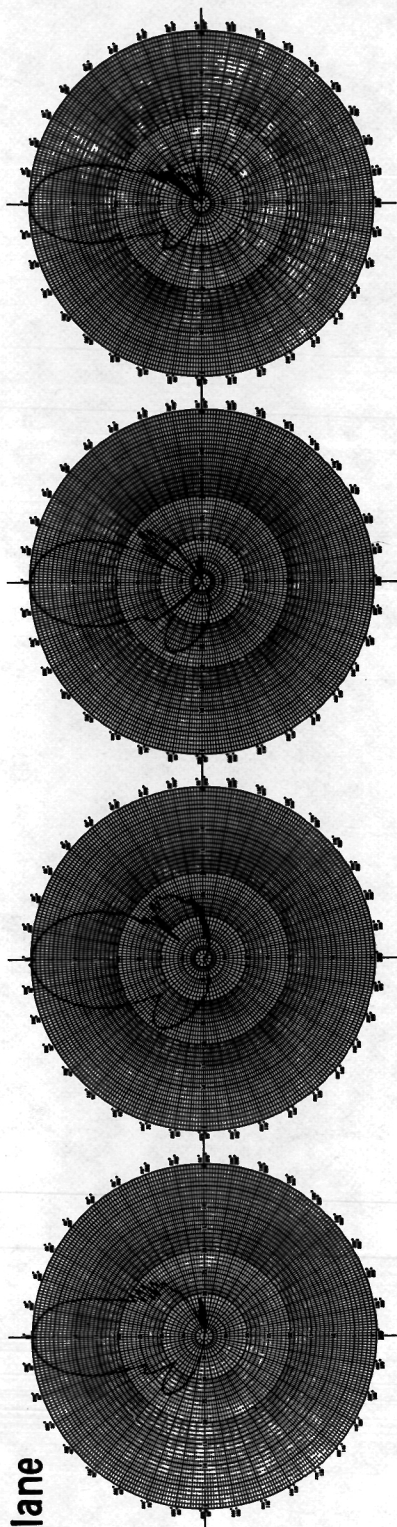
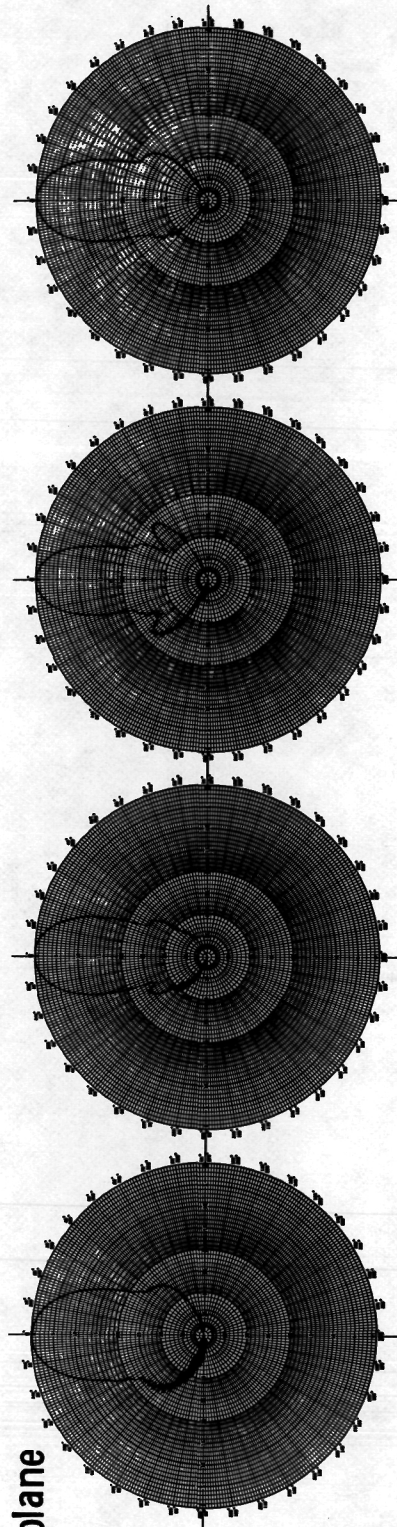


Figure 47.- Concluded.

E-plane



H-plane



5.0 GHz

5.1 GHz

5.2 GHz

5.3 GHz

Figure 48.- E-plane and H-plane radiation patterns for 64-element planar array.

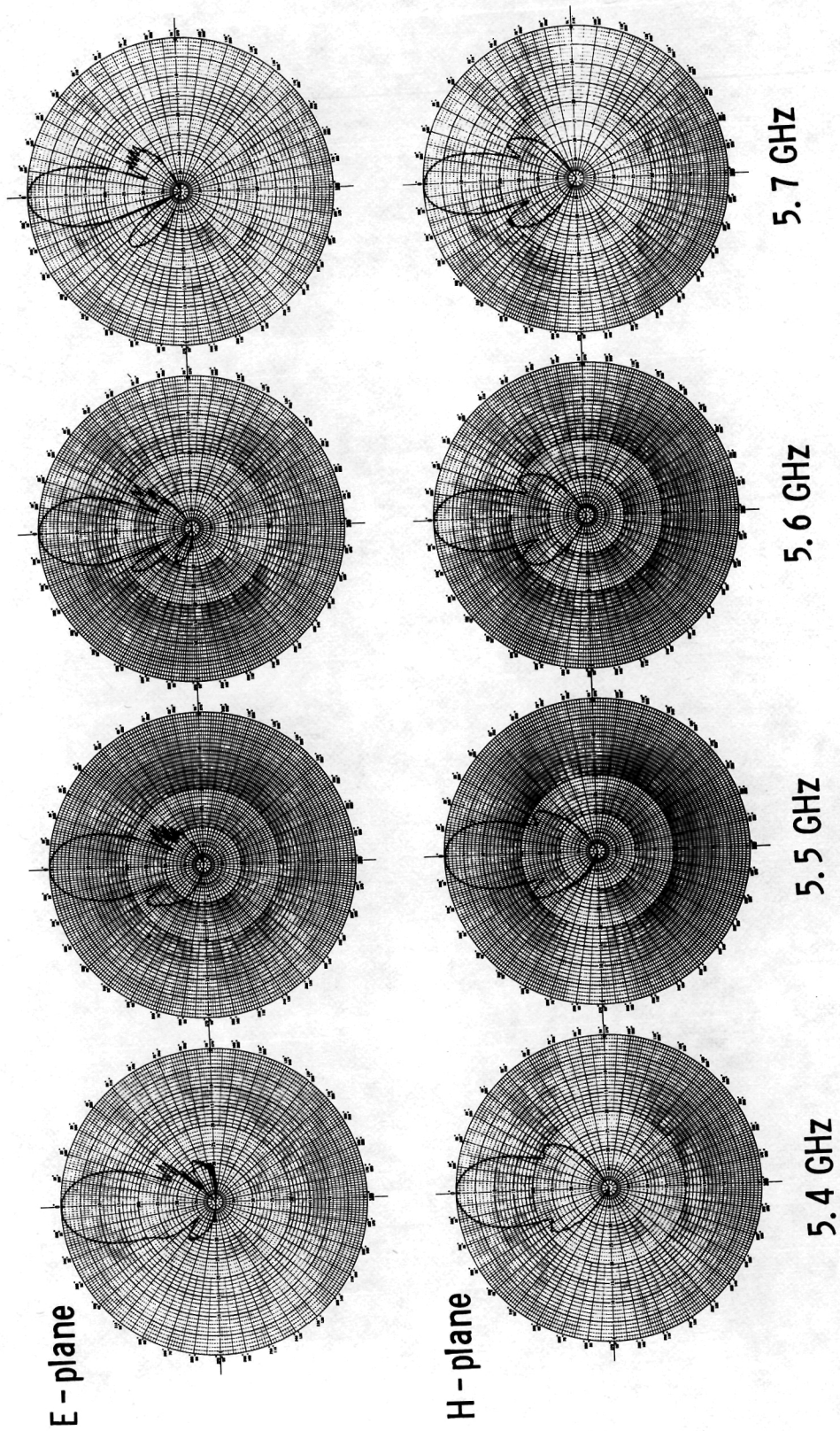
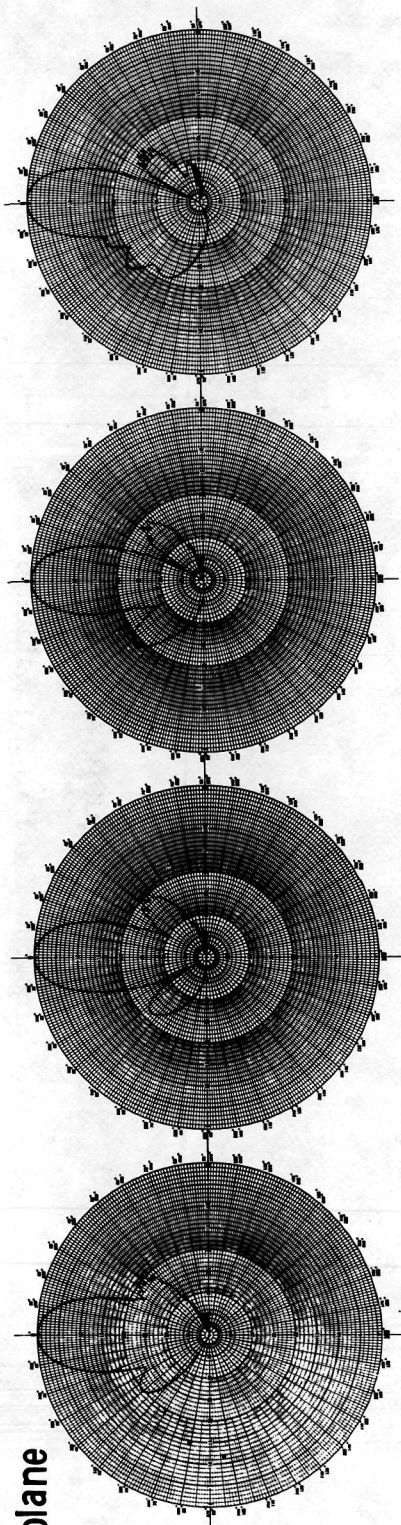
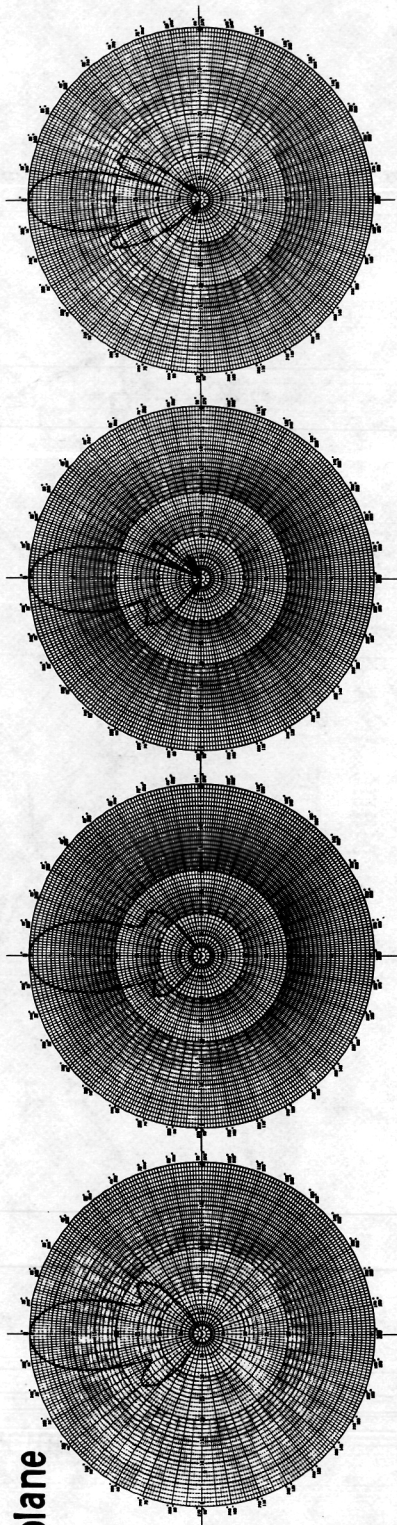


Figure 48.- Continued.

E - plane



H - plane



5.8 GHz

5.9 GHz

6.0 GHz

6.1 GHz

Figure 48.- Concluded.

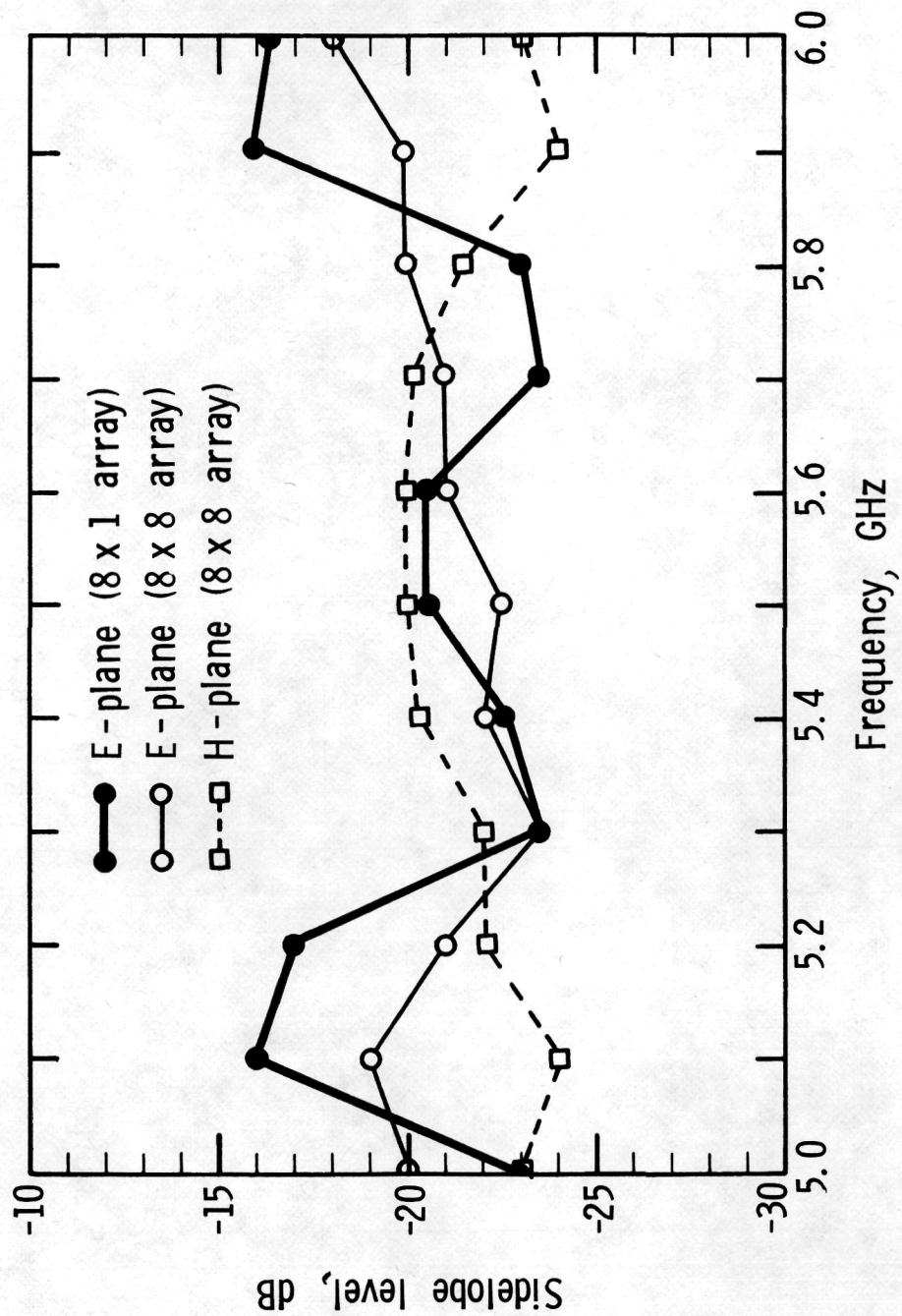
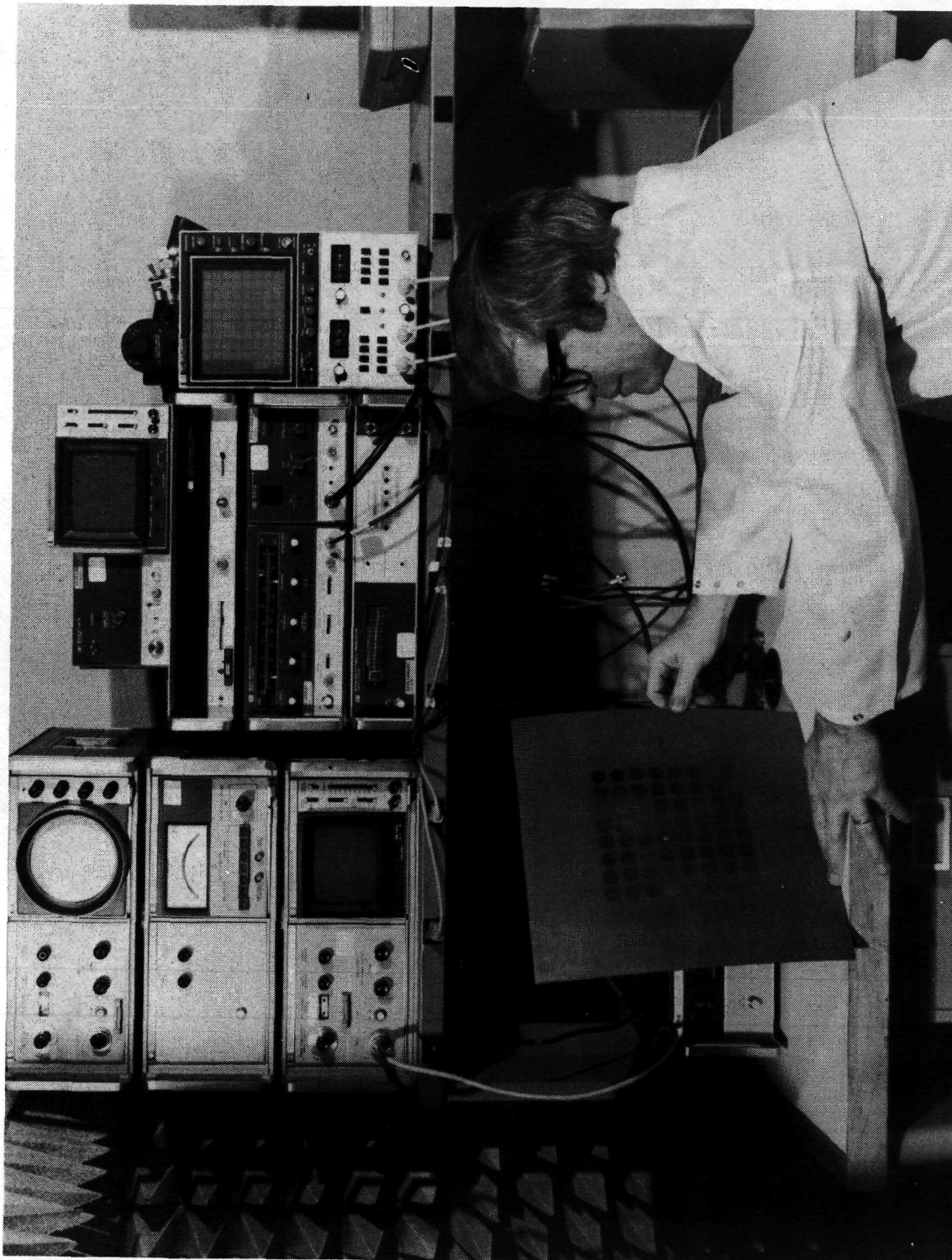


Figure 49.- Sidelobe level as a function of frequency.



L-77-2290

Figure 50.- Network analyzer measurement system.

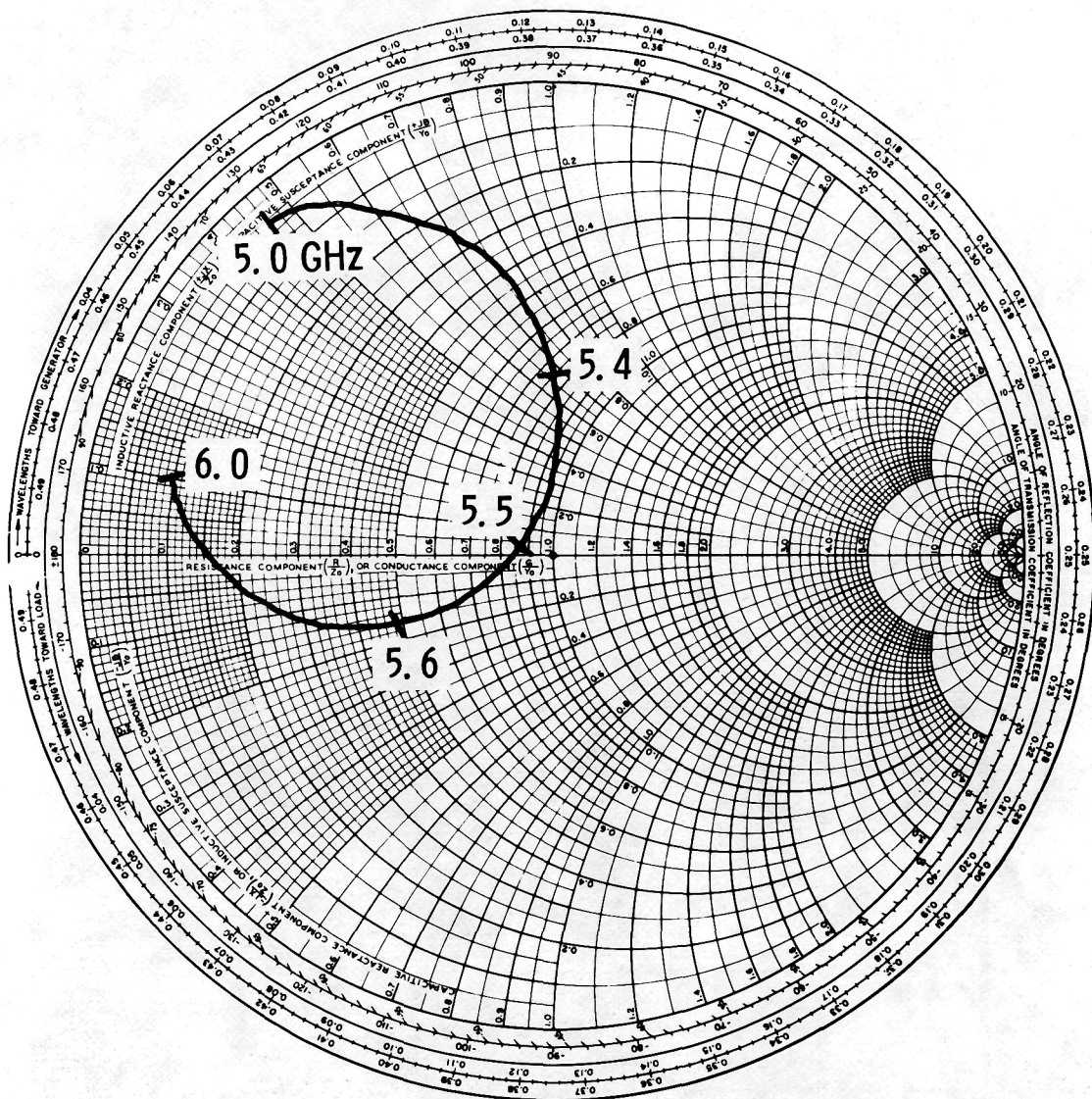


Figure 51.- Measured impedance of a microstrip disk.

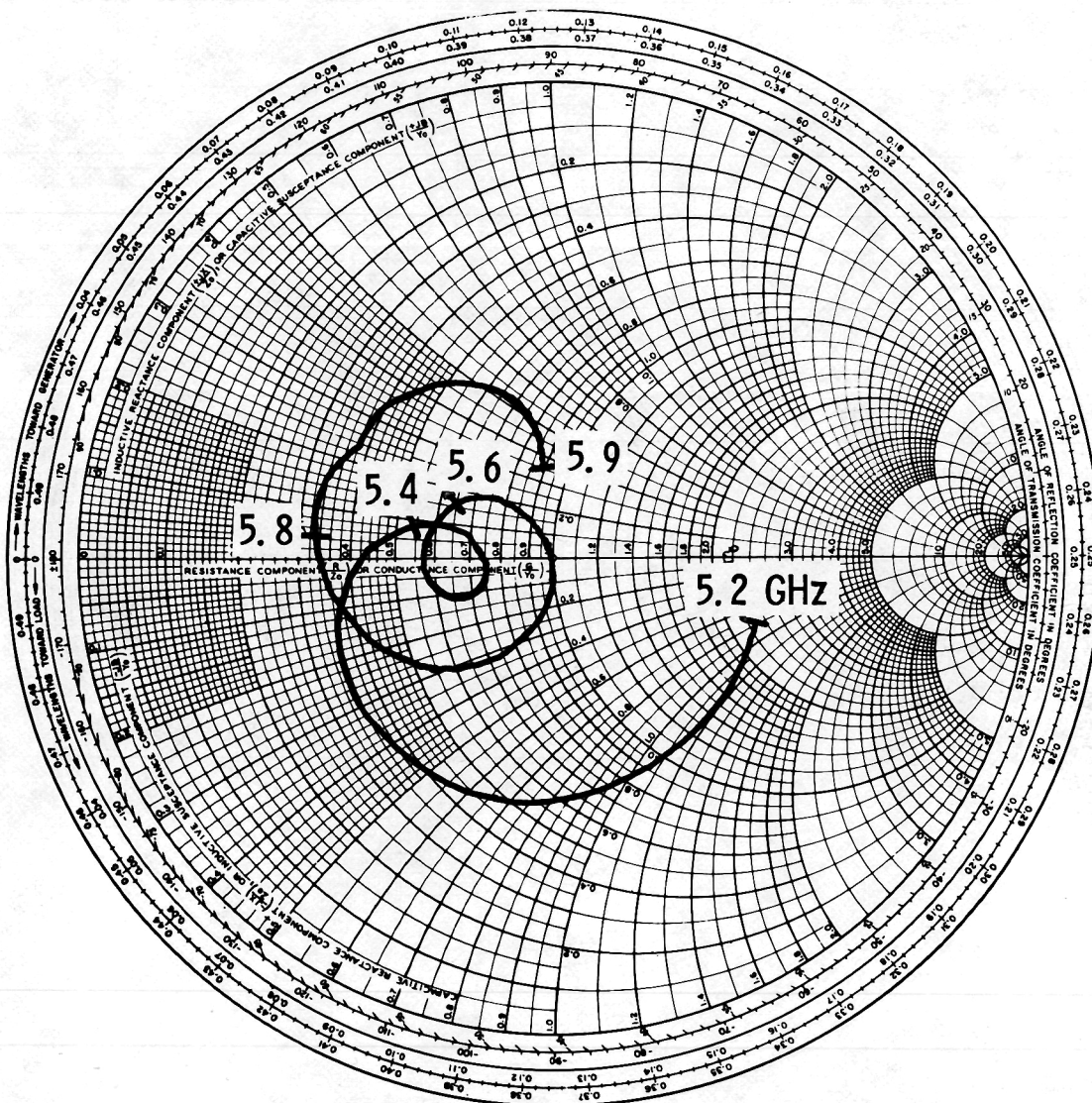


Figure 52.- Measured impedance of 8-element linear array.

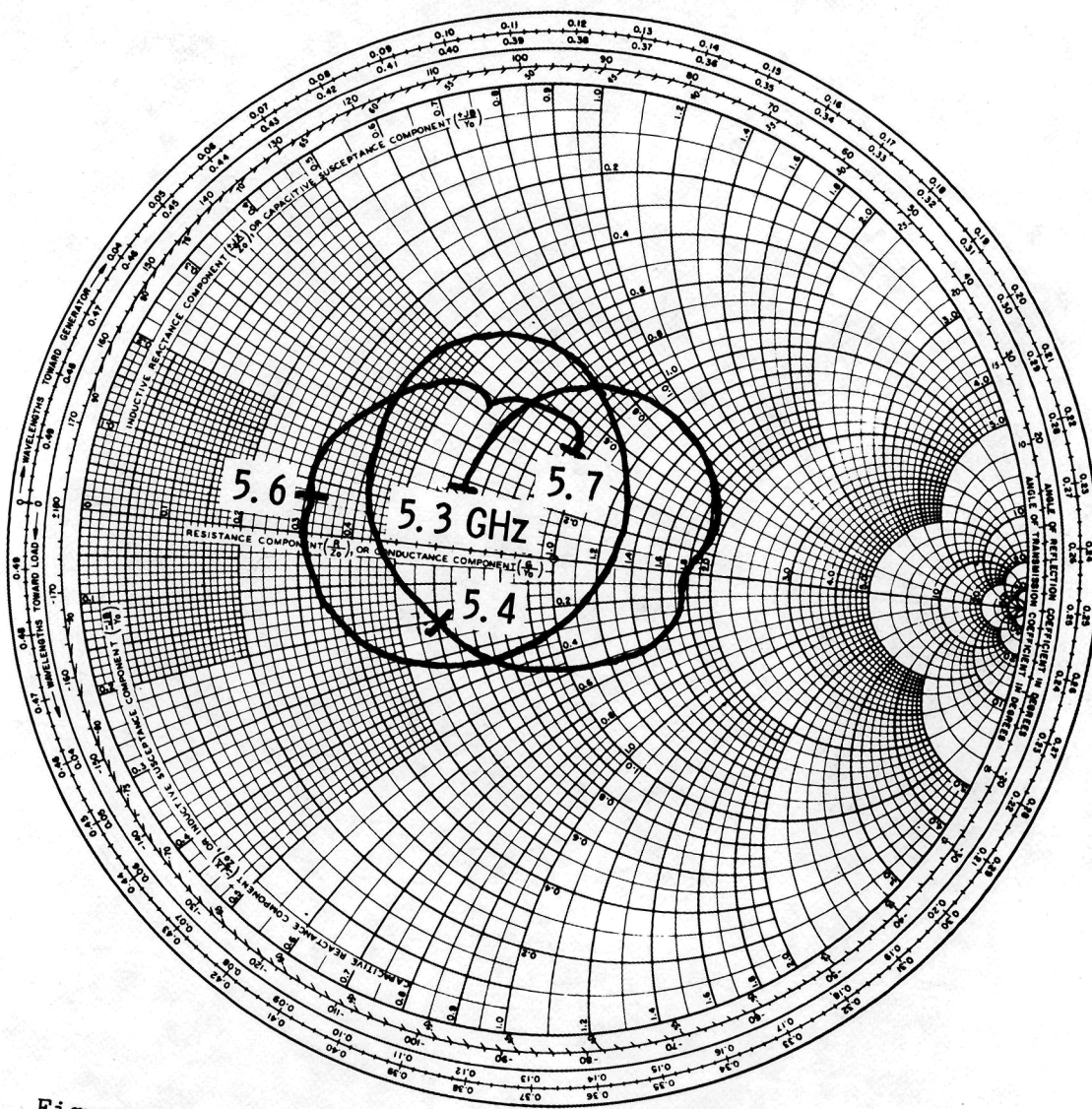


Figure 53.- Measured impedance of 64-element planar array.

1. Report No. NASA TM-78631		2. Government Accession No.		3. Recipient's Catalog No.	
4. Title and Subtitle DESIGN OF MICROSTRIP DISK ANTENNA ARRAYS				5. Report Date February 1978	
				6. Performing Organization Code	
7. Author(s) M.C. Bailey and F. G. Parks				8. Performing Organization Report No. L-11926	
9. Performing Organization Name and Address NASA Langley Research Center Hampton, VA 23665				10. Work Unit No. 505-07-22-01	
				11. Contract or Grant No.	
12. Sponsoring Agency Name and Address National Aeronautics and Space Administration Washington, DC 20546				13. Type of Report and Period Covered Technical Memorandum	
				14. Sponsoring Agency Code	
15. Supplementary Notes F. G. Parks: Graduate Research Associate, Univ. of Kansas, Lawrence, Kansas now at Sanders Associates, Inc., Nashua, New Hampshire.					
16. Abstract The radio frequency characteristics and design parameters for microstrip disk antenna elements and planar arrays are presented. Two C-band model arrays (an 8-element linear and an 8 by 8 planar) were designed, fabricated, and tested to demonstrate the technique of using microstrip elements for array applications. These arrays were designed with a cosine amplitude distribution. The effects of a thermal protective cover upon the electrical performance of microstrip antennas were not considered in this paper.					
17. Key Words (Suggested by Author(s)) Antennas Arrays Antenna design Microstrip Low-profile antenna			18. Distribution Statement Unclassified - Unlimited Subject Category 32		
19. Security Classif. (of this report) Unclassified	20. Security Classif. (of this page) Unclassified	21. No. of Pages 80	22. Price* \$6.00		

* For sale by the National Technical Information Service, Springfield, Virginia 22161

NASA-Langley, 1977

National Aeronautics and
Space Administration

THIRD-CLASS BULK RATE

Postage and Fees Paid
National Aeronautics and
Space Administration
NASA-451

Washington, D.C.
20546

Official Business

Penalty for Private Use, \$300



NASA

POSTMASTER:

If Undeliverable (Section 158
Postal Manual) Do Not Return

HQ SAMTEC, AFL 2827
TECHNICAL LIBRARY (PMET)
VANDENBERG AFB, CA 93437